General Disclaimer

One or more of the Following Statements may affect this Document

- This document has been reproduced from the best copy furnished by the organizational source. It is being released in the interest of making available as much information as possible.

- This document may contain data, which exceeds the sheet parameters. It was furnished in this condition by the organizational source and is the best copy available.

- This document may contain tone-on-tone or color graphs, charts and/or pictures, which have been reproduced in black and white.

- This document is paginated as submitted by the original source.

- Portions of this document are not fully legible due to the historical nature of some of the material. However, it is the best reproduction available from the original submission.

Produced by the NASA Center for Aerospace Information (CASI)

THE UNIVERSITY OF KANSAS SPACE TECHNOLOGY CENTER
Raymond Nichols Hall

2291 Irving Hill Drive—Campus West   Lawrence, Kansas 66045
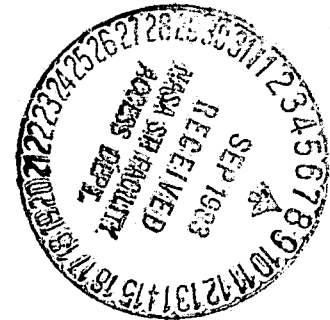
Telephone: 913-864-4832

E84-10009
CR-174524

MICROWAVE REMOTE SENSING OF SNOW

EXPERIMENT DESCRIPTION AND PRELIMINARY RESULTS

Remote Sensing Laboratory
RSL Technical Report   340-1

W. H. Stiles

B. C. Hanson

F. T. Ulaby

June, 1977

Fawwaz T. Ulaby, Principal Investigator

CRES

—————————————————————————REMOTE SENSING LABORATORY

ACKNOWLEDGEMENTS

<div align="right">

Fawwaz T. Ulaby
Principal Investigator

</div>

i

TABLE OF CONTENTS

TABLE OF CONTENTS (CONTINUED)

LIST OF TABLES

LIST OF FIGURES

LIST OF FIGURES (CONTINUED)

Page

LIST OF FIGURES (CONTINUED)

LIST OF FIGURES (CONTINUED)

LIST OF FIGURES (CONTINUED)

Page

ABSTRACT

The active and passive microwave responses to snow were investigated
at a site near Steamboat Springs, Colorado during the February and March
winter months of 1977. The microwave equipment was mounted atop truck-
mounted booms. Data were acquired at numerous frequencies, polarizations
and angles of incidence for a variety of snow conditions. This report
documents the experiment description, the characteristics of the microwave
and ground truth instruments and presents the results of a preliminary
analysis of a small portion of the total data volume acquired in Colorado.

1.0 INTRODUCTION

Snowpack water is a major component of the total water supply for the Western United States, Alaska and many other parts of the world. Since the runoff from snowmelt is usually limited to the spring and early summer, conservation of this water is very important. Accurate prediction of runoff is therefore needed on a seasonal, monthly, weekly and daily basis for flood control, hydroelectric power generation, irrigation, domestic and industrial water supplies, and recreation.

Present methods for monitoring snowpack characteristics use statistical models based on a few widespread sample points. Recently aerial photography and ERTS imagery have shown some promise for mapping snow extent [1,2]. Microwave remote sensing has several potential advantages over optical remote sensing. Snow covered areas tend to be cloud covered for large portions of the time. The ability of microwave sensors to make timely observations unhampered by cloud cover is very important to snowpack monitoring. Moreover, the greater penetration of microwaves into the snowpack can potentially provide information on the depth profile of the snowpack properties of interest.

Cosgriff et al. [3] made measurements on snow covered ground with a CW-doppler scatterometer and observed that snow had the effect of lowering the backscatter of the underlying terrain. The University of Kansas Remote Sensing Laboratory conducted an experiment in early 1975 to investigate the radar response to snow cover [4]. This experiment showed strong sensitivity of the radar measurements to snow wetness (free water in the snowpack). Both of the above experiments were hampered by inadequate snowfall and incomplete ground truth data

Edgerton et al. [5] made radiometric measurements of snow and determined that a direct relationship existed between brightness temperature and water equivalent for dry snow. For wet snow, a complex behavior was reported. More recently, Kunzi et al. [6] examined possibilities of large scale mapping of snow cover using Nimbus-5 data.

The conclusions derived from the above experiments are limited in scope because of the limited data base and the often narrow range over which the sensor or snow parameters varied. In an effort to better

understand the microwave scattering and emission properties of snow, the University of Kansas conducted an extensive experimental program during the period from 2 February to 25 March 1977 at a site near Steamboat Springs, Colorado. The microwave instruments used included the MAS 1-8 (1 to 8 GHz radar), the MAS 8-18/35 (8 to 18 and 35 GHz radar), and three radiometers (10.69, 37 and 94 GHz). Ground data were also acquired to facilitate interpretation of the remotely sensed data. Figure 1 gives the timetable of the experiment and operation periods for the various measurement systems and Table 1 is a summary of the data volume acquired. The measurement systems will be described in more detail in Section 2.

This report covers the experiments, equipment descriptions, a section on fading, and some preliminary results. Specifically, the preliminary results include two of the diurnal experiments, the single spot fading time history experiment, the snowpile experiments, and the 35 GHz attenuation experiment.
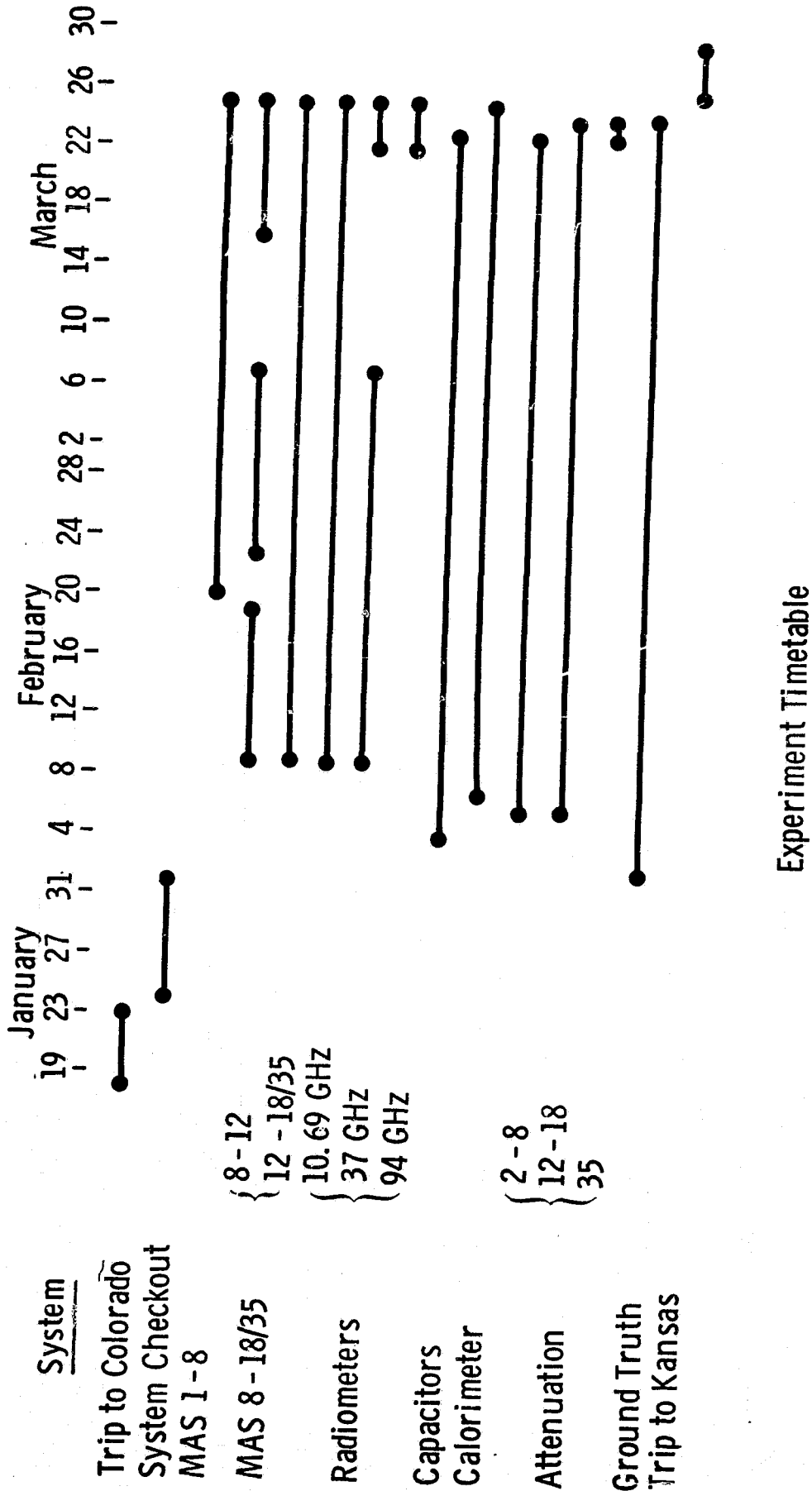
Figure 1. Experiment timetable showing data acquisition periods of the various systems.

3

TABLE 1. Data Base of 1977 Snow Experiment
at Steamboat Springs, Colorado.

SYSTEM	DATA SETS
MAS 1-8	
Diurnal subsets	34
Regular sets	46
TOTAL	80
MAS 8-18/35	
Diurnal subsets	90
Regular sets	40
TOTAL	130
Radiometers	
X-band	
Diurnal subsets	96
Regular sets	40
TOTAL	136
37 GHz	
Diurnal subsets	77
Regular sets	26
TOTAL	103
94 GHz	
Diurnal subsets	29
Attenuation Sets	
2-8 GHz	67
12-18 GHz	40
35 GHz	4
Capacitance Measurements	201
Calorimeter Measurements	217
Temperature Profiles	270
Ground Truth Sets	198
Photographs	576

4

2.0 EXPERIMENT DESCRIPTION

The following section covers the test site selection, equipment descriptions and data acquisition.

2.1 Test Site Description

After considering several potential test sites for conducting the snow experiment, the area around Steamboat Springs, Colorado was selected and a 40 acre hayfield was rented from Mr. Ben Hibbert of Steamboat Springs. Figure 2 shows the location of the test site. The surface of the field was very flat and was covered with closely cut hay approximately six centimeters tall. Figure 3 illustrates the experiment layout. Test plot #1 was the main test area for observation with the microwave sensors. Test plot #2 contained buried enclosures for the attenuation experiment. It was also to serve as the back-up area for the main test plot. The radar trucks were parked between plots #1 and #2 and remained stationary for the duration of the experiment. Connections were made to the electric company and the telephone company for the experiment duration. Figure 4 shows the trucks and ancillary equipment in place at the test site.

2.2 Microwave Sensors

Both active and passive systems were employed to measure the microwave properties of snow. The MAS 1-8, MAS 8-18/35 and three radiometers were used in the experiment. The following section describes these sensors.

2.2.1 MAS 1-8 and MAS 8-18/35

The MAS 1-8 and the MAS 8-18/35 are truck mounted wideband FM-CW radars. Figure 4 shows both the MAS 1-8 and MAS 8-18/35 in operation at the Steamboat Springs test site. Figure 5 shows a picture of the MAS 1-8 radar. Figure 6 is a closeup of the antenna section of the MAS 8-18/35. The system specifications for both MAS systems are given in Table 2. A block diagram of the MAS 1-8 system is shown in Figure 7. The MAS 8-18 system is identical to the MAS 1-8 system block diagram except for frequency coverage. The 35 GHz channel is shown in block

Colorado 131

to Steamboat
Springs

Figure 2. View of the test site south of
Steamboat Springs, Colorado.

MAS 1-8

Instrumentation Van

MAS 8-18/35

weather
station

Pyronameter
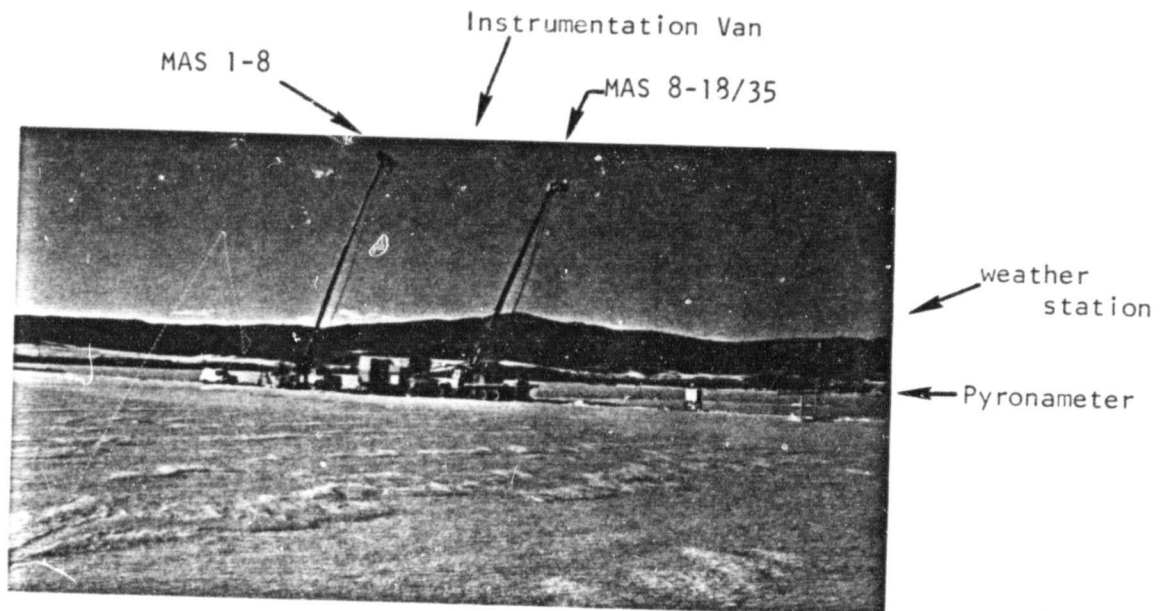
Figure 4. Test plot layout.

Scale: 1/2" = 100 ft.
—•— Fence Lines
• Temperature Thermister Profile Poles
+ Snow Depth Ganging Stations

|←— 300 ft. —→|

Test Plot #2

•Luneberg Lens Locations

300 ft.

Attenuation Pits

Hay Bales

15 ft. —→

Gate

+

300 ft.

75 ft.

Test Plot #1

50 ft. —→

Colo. 131

Road to U. S. 40
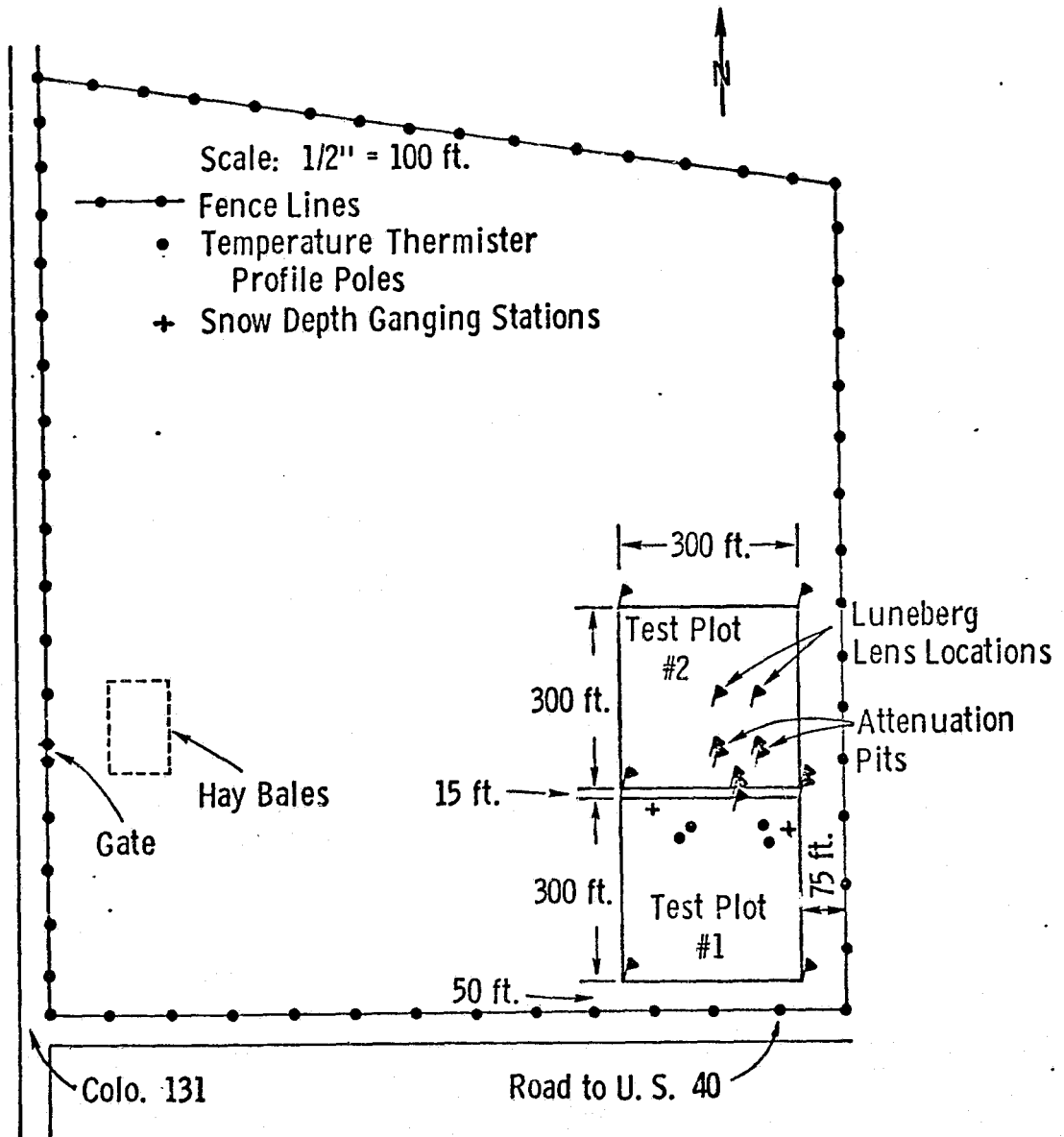
Figure 3. Steamboat Springs test site layout.
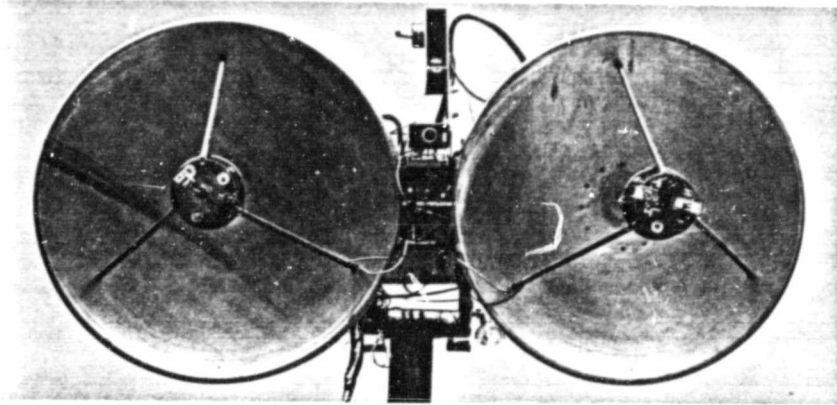
Figure 5.   Closeup of MAS 1-8 RF section.

94 GHz radiometer

35 GHz scatterometer antennas

electronics enclosure

10.69 GHz
radiometer

37 GHz
radiometer

MAS 8-18 antennas
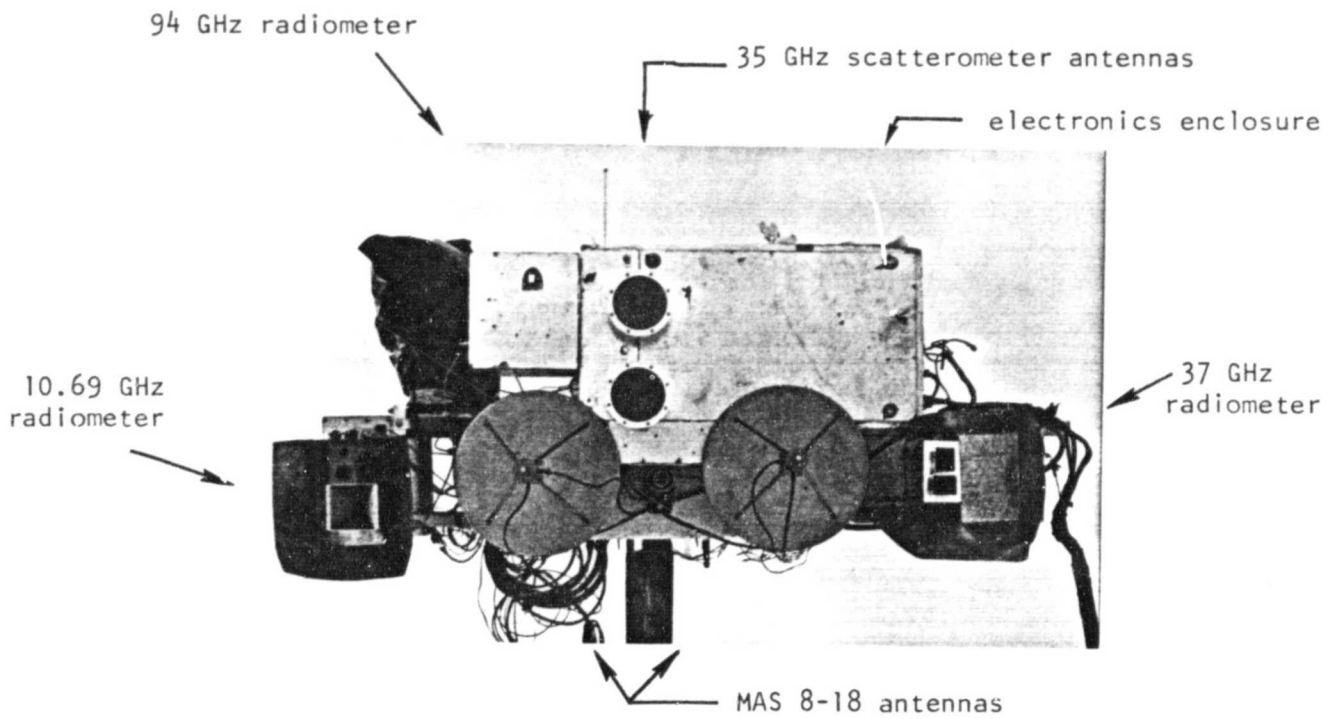
Figure 6.   Closeup of the MAS 8-18/35 RF section.

TABLE 2.

MAS 1-8 and MAS 8-18/35 Nominal System Specifications

	MAS 1-8	MAS 8-18	35 GHz Channel
Type	FM-CW	FM-CW	FM-CW
Modulating Waveform	Triangular	Triangular	Triangular
Frequency Range	1-8 GHz	8-18 GHz	35.6 GHz
FM Sweep: Δf	400 MHz	800 MHz	800 MHz
Transmitter Power	10 dBm	10 dBm	1 dBm
Intermediate Frequency	50 KHz	50 KHz	50 KHz
IF Bandwidth	10 KHz	10 KHz	10 KHz
Antennas			
Height of Ground	20 m	26 m	26 m
Type	122 cm Reflector	46 cm Reflector	Scalar Horn
Feeds	Crossed Log-Periodic	Quad-Ridged Horn	----
Polarization Capabilities	HH, HV, VV	HH, HV, VV	HH, HV, VV, RR, RL, LL
Beamwidth	12° at 1.25 GHz to 1.8° at 7.25 GHz	4° at 8.6 GHz to 2° at 17.0 GHz	3°
Incidence Angle Range	0° (nadir)-80°	0° (nadir)-80°	0° (nadir)-80°
Calibration:			
Internal	Signal Injection (delay line)	Signal Injection (delay line)	Signal Injection (delay line)
External	Luneberg Lens Reflector	Luneberg Lens Reflector	Luneberg Lens Reflector

9
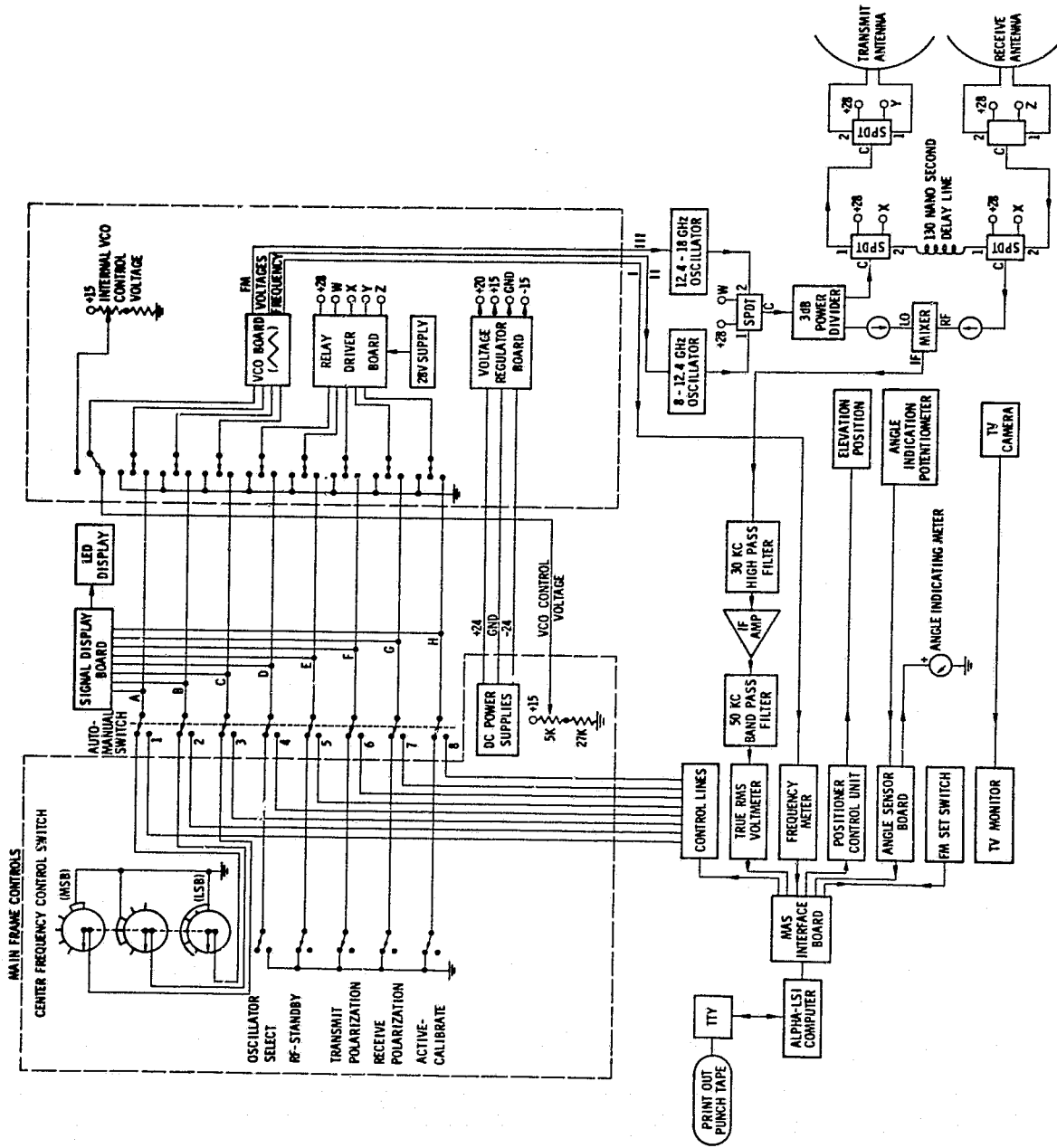
Figure 7. MAS 8-18 block diagram.

diagram form in Figure 8. Radar data were taken at eight frequencies between 1.125 GHz and 7.75 GHz for MAS 1-8. MAS 8-18/35 took data at 11 frequencies between 8.6 and 17.0 GHz and at 35.6 GHz. The systems operate in three polarization configurations, HH (horizontal transmit-horizontal receive), HV (horizontal transmit-vertical receive), and VV (vertical transmit-vertical receive). In addition, at 35.6 GHz, RR (right circular transmit-right circular receive), RL (right circular transmit-left circular receive), and LL (left circular transmit-left circular receive) polarizations are measured. Data can be obtained at any angle of incidence between 0° and 80° from nadir. Receive power levels are converted to scattering cross section by a two step calibration procedure. Short term power variations due to oscillator power, mixer temperature, etc., are normalized by referencing the power to the power through a coaxial delay line of known loss. Actual calibration to radar cross section is accomplished by referencing the return power to the power returned from an object of known radar cross section. A Luneberg lens is used for that purpose. The Luneberg lens has a radar cross section which has been calibrated against a metal plate. The advantage of using the lens for this purpose is its relative insensitivity to orientation.

The calculation of $\sigma°$ results from evaluating the radar equation for an area extensive target.

$$P_r = \iint\limits_A \frac{P_t \, G_t \, G_r \lambda^2 \sigma° \, dA}{(4\pi)^3 \, R_t^4} \tag{1}$$

where

P_r = received power

P_t = transmitted power

G_t = transmit antenna gain

G_r = receive antenna gain

λ = wavelength

$\sigma°$ = scattering coefficient

R_t = target range

dA = differential element of illuminated area
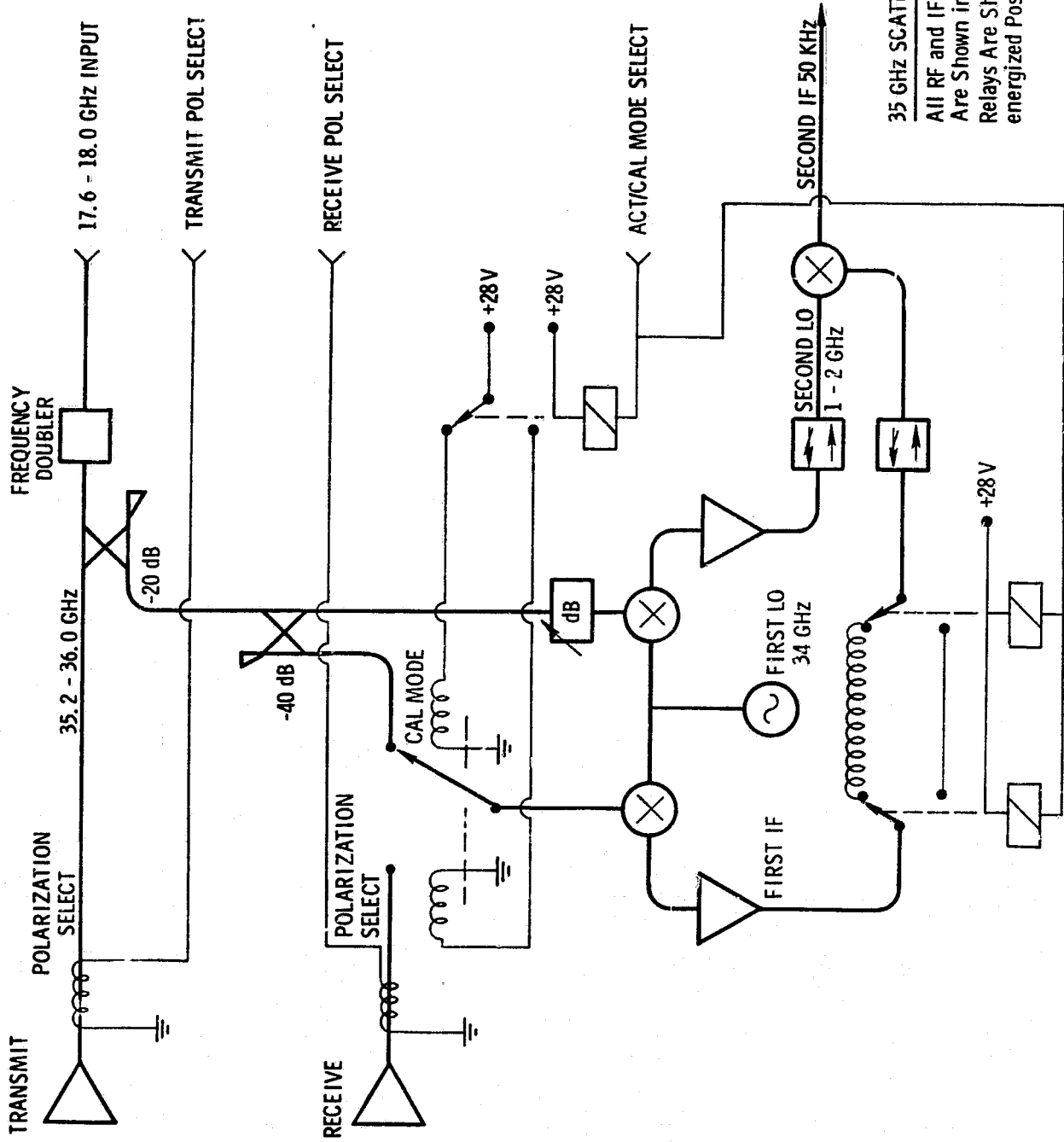
11

Figure 8. Overall Schematic of the 35 GHz Radar Module

12

If the assumption is made that the parameters inside the integral are constant over the illuminated area the radar equation becomes:

$$P_r = \frac{P_t\, G_t\, G_r \lambda^2 \sigma^\circ\, A_{ill}}{(4\pi)^3\, R_t^4} \tag{2}$$

Note that P_r represents the received power at the receive antenna terminal. If we introduce an unknown constant K_t to represent the effects of cable loss, mixer conversion loss etc., we can write

$$V_t = K_t \left[\frac{P_t\, G_t\, G_r \lambda^2 \sigma^\circ\, A_{ill}}{(4\pi)^3\, R_t^4}\right]^{1/2} \tag{3}$$

where V_t is the voltage at the mixer output.

Shortly before or after recording the return from the target of interest, switches at the transmit and receive RF lines are actuated to replace the transmit antenna-receive antenna path with a coaxial delay line of loss L. Thus, the voltage received is given by:

$$V_{td} = K_t\, [P_t\, L]^{1/2} \tag{4}$$

The ratio of the two voltages, M_t, is given by:

$$M_t = \frac{V_t}{V_{td}} = \left[\frac{G_t\, G_r \lambda^2 \sigma^\circ\, A_{ill}}{(4\pi)^3\, R_t^4}\right]^{1/2} \tag{5}$$

Thus any variations in P_t or K_t are removed by this internal calibration technique.

In addition to internal calibration, external calibration is also conducted by recording the voltage corresponding to the return from a standard target of known radar cross section, in this case a Luneberg lens. The measured voltage is given by:

$$V_c = K_c \left[\frac{P_t \, G_t \, G_r \lambda^2 \sigma_c}{(4\pi)^3 \, R^4_c} \right]^{1/2} \tag{6}$$

where K_c is the receiver transfer constant during calibration against the lens, R_c is the range to the lens and σ_c is the radar cross section of the lens. Again internal calibration is conducted shortly before recording the voltage due to the calibration target:

$$V_{cd} = K_c \left[P_t \, L \right]^{1/2} \tag{7}$$

and the ratio is given by:

$$M_c = \frac{V_c}{V_{cd}} = \left[\frac{G_t \, G_r \lambda^2 \sigma_c}{(4\pi)^3 \, R^4_c L} \right]^{1/2} \tag{8}$$

Combining Eqs. 5 and 8 yields the following expression for $\sigma°$ in dB:

$$\sigma°(dB) = 20 \log M_t - 20 \log M_c + 10 \log \sigma_c \tag{9}$$
$$- 10 \log A_{ill} + 40 \log R_t - 40 \log R_c$$

The first two quantities are measured and recorded by the system and σ_c is known (measured by the manufacturer) with respect to a flat plate. A_{ill} is calculated from the geometry on the basis of measured values of the beamwidths (for each frequency-polarization configuration) and the range R_t. Finally, R_t and R_c are determined through measurement of the modulation frequency f_m:

$$R = \frac{f_{iF} \, c}{4 \, \Delta f \, f_m} \tag{10}$$

14

where

c = the velocity of propagation

f_{IF} = intermediate frequency

Δf = FM sweep

f_m = modulation rate

2.2.2 Radiometers

Passive microwave data were acquired with radiometers operating at 10.69, 37 and 94 GHz. These devices were all either borrowed or rented for the experiment. The manufacturer's specifications are given in Table 3. Block diagrams of the radiometers are shown in Figures 9-11.

TABLE 3. Radiometer Specifications

Manufacturer	Aerojet	Aerojet	Sperry
Frequency	10.69 GHz	37 GHz	94 GHz
Type	Dicke	Dicke	Total-power
Polarization	H	H and V	H
Bandwidth	200 MHz	300 MHz	730 MHz
Sensitivity (Δt min)	.2K (1-sec.)	.5K (1-sec.)	3.5K
Accuracy	1K	$\pm 1K$	$\pm[.05(300-T_s)+6]$
Temperature Range	50-350K	0-500K	0-500K
Approx. Gain (Volt/K)	-.012	.010	.020
AGC	No	Yes	Yes
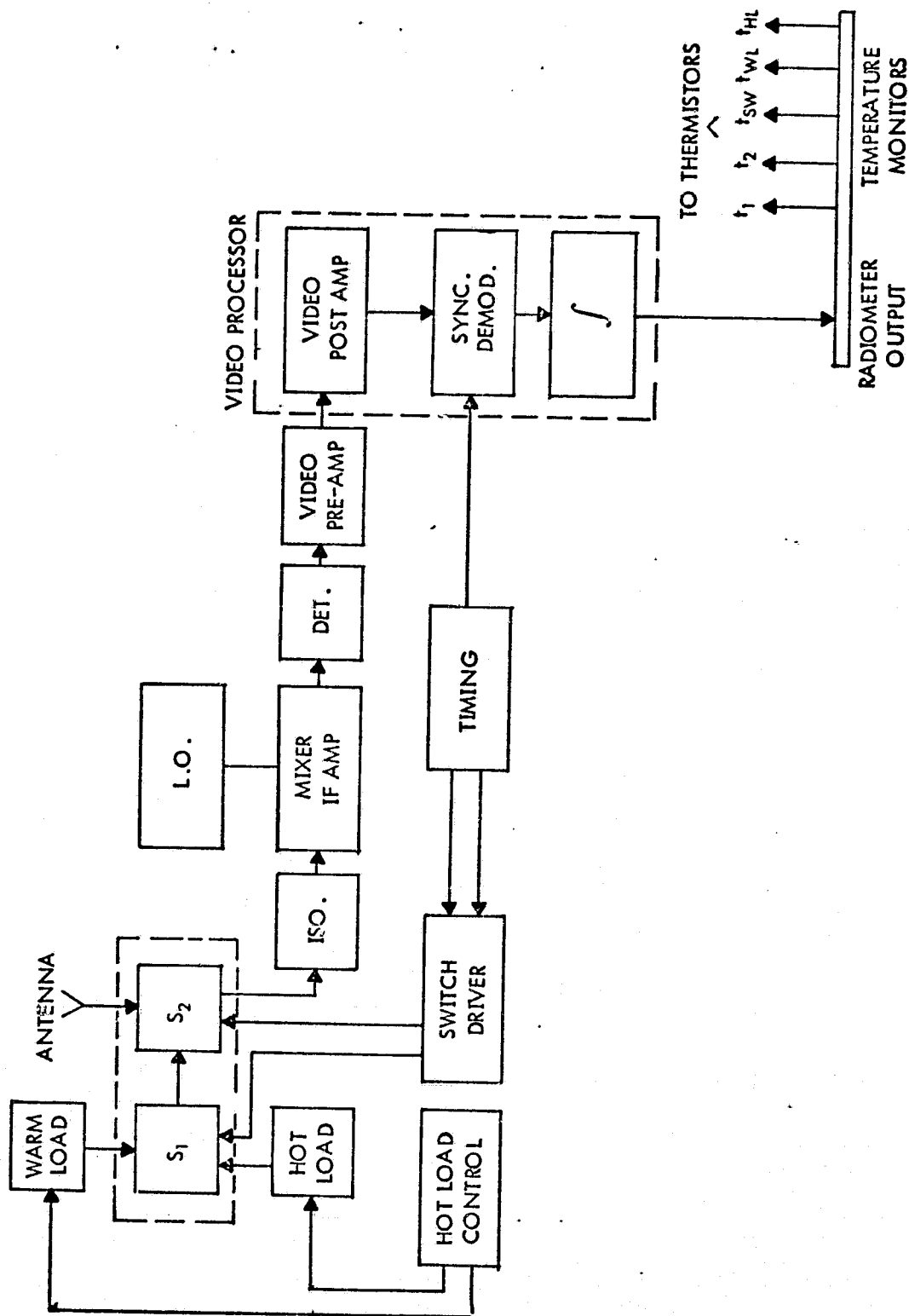
Figure 9. Functional block diagram of 10.69 GHz radiometer [7].
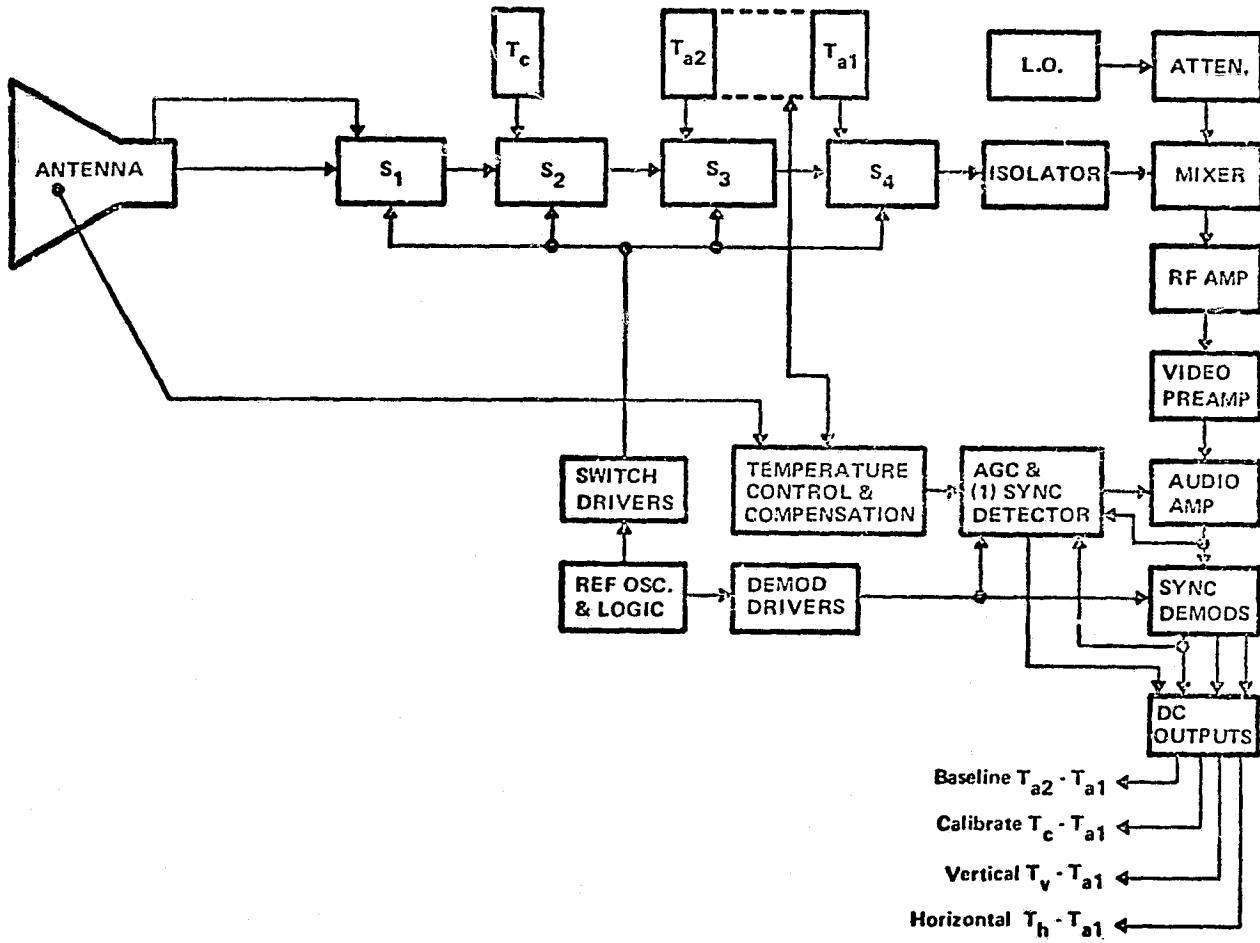
Figure 10.   Functional block diagram of
37 GHz radiometer.
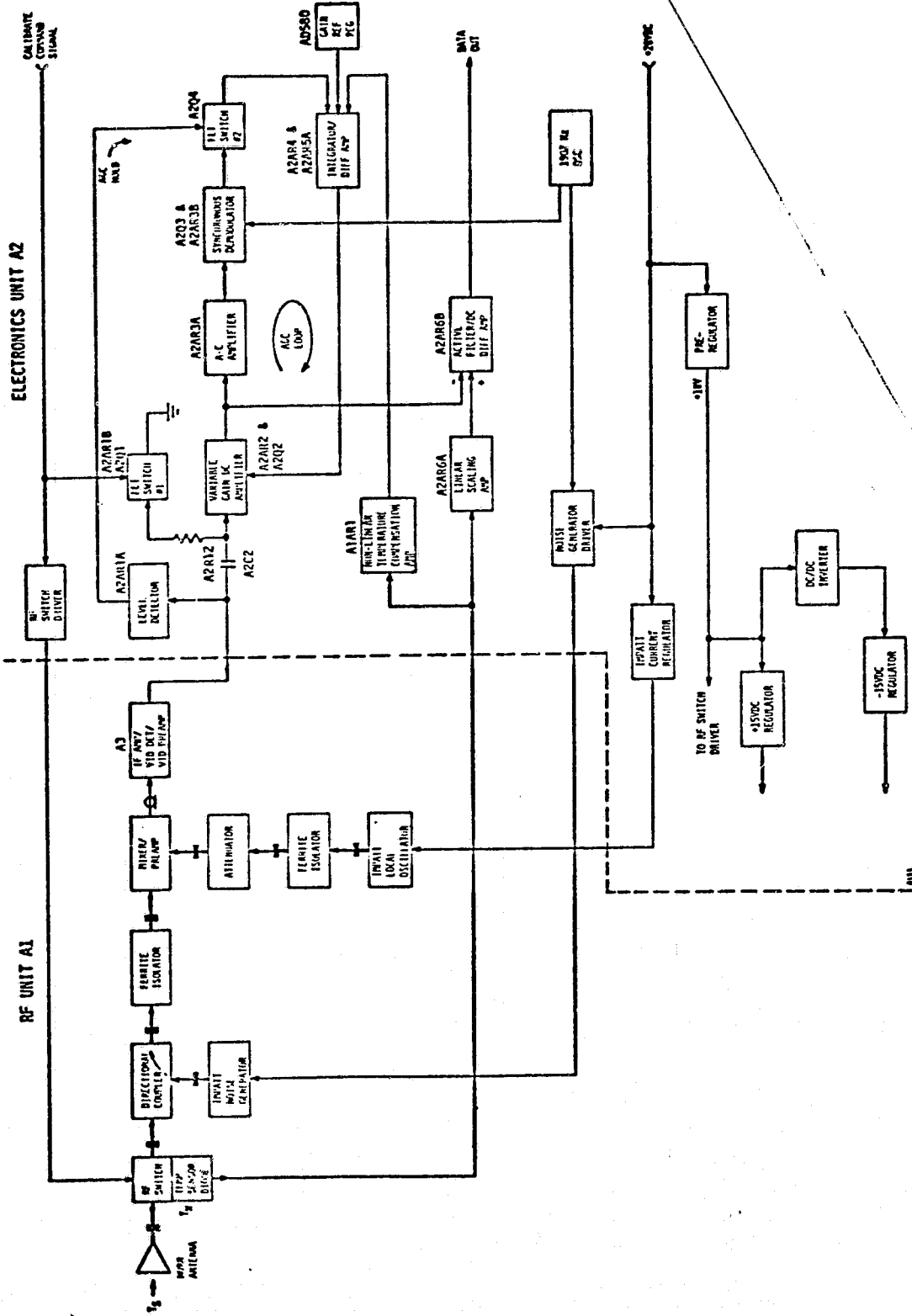
Figure 11.   Functional block diagram 94 GHz radiometer [8].

18

The 10.69 and 37 GHz radiometers were operated with 1-second integration time. Data were taken at the same angles as the scatterometers since the radiometers were located (Figure 6) on the boom with the scatterometers. Calibration of the radiometers was checked when possible by looking at the sky or microwave absorber.

X-band (10.69 GHz) radiometer

The following equations were used to convert the measured voltages and physical temperatures of components to T_{ap}, the radiometric temperature of the scene viewed by the antenna.

$$T_{HL} = \frac{t_{hl}}{1.108} + \frac{t_{hl} + t_{sw}}{136.8} + \frac{t_{sw}}{12.06} \tag{11}$$

$$T_{WL} = \frac{t_{wl}}{1.106} + \frac{t_{wl} + t_{sw}}{136.5} + \frac{t_{sw}}{12.38} \tag{12}$$

$$G = \frac{V_{CAL} - V_{BL}}{T_{HL} - T_{WL}} \tag{13}$$

$$T_R = T_{HL} - \frac{V_{ANT} - V_{BL}}{G} \tag{14}$$

$$T_{in} = 1.042 \left[T_R - \frac{t_1 + t_2}{239.7} - \frac{t_2 + t_{sw}}{738.6} - \frac{t_{sw}}{34.25} \right] \tag{15}$$

$$T_{ap} = 1.009 \, L_{ANT} \left[T_{in} - t_{ANT} \left(1 - \frac{1}{L_{ANT}} \right) (.9951) - \frac{T_{RAD}}{440.5} \right] \tag{16}$$

where

t_{hl}	=	physical temperature of hot load
t_{sw}	=	physical temperature of Dicke switch
t_{wl}	=	physical temperature of warm load
t_1	=	physical temperature of waveguide 1
t_2	=	physical temperature of waveguide 2
t_{ANT}	=	physical temperature of antenna
L_{ANT}	=	loss of the antenna
G	=	gain factor
T_{HL}	=	radiometric temperature of hot load
T_{WL}	=	radiometric temperature of warm load
T_{in}	=	radiometric temperature at receiver input
T_{ap}	=	radiometric temperature at the input to the antenna
V_{ANT}	=	voltage measured with receiver connected to the antenna
V_{CAL}	=	voltage measured with receiver connected to the warm load
V_{BL}	=	voltage measured with receiver connected to the hot load
T_{RAD}	=	radiometric temperature of energy emitted by the radiometer RF section

Equations 11-15, provided by the radiometer manufacturer's manual [7], represent the system transfer function between the input to the receiver (T_{in}) and the final output voltages. Equation 16 relates T_{ap} to T_{in} by taking into account absorption and mismatch losses of the antenna and waveguide section. The mismatch losses were measured and supplied by Dr. Lawrence Klein of NASA Langley Research Center. Matching Equation 16 against calculated values of T_{in} from measurements of the emission by an anechoic absorber of known physical temperature yields a value for L_{ANT} approximately equal to 1.0.

37 GHz Radiometer

The following two equations were used to calculate T_{ap} for the two channels from the measured voltages. These equations are best fits to the calibration points shown in Figures 12 and 13.

$$T_{ap} \text{ (horizontal)} = 95.06 \, V_H - 1.02 \tag{17}$$

$$T_{ap} \text{ (vertical)} = 102.8 \, V_V - 23.52 \tag{18}$$

where V_H and V_V are measured voltages.

94 GHz Radiometer

Figure 14 shows the best fit curve for the 94 GHz radiometer calibration:

$$T_{ap} = 53.4 \, V_{ANT} - 20.86 \tag{19}$$

where V_{ANT} is the measured voltage.

Fluctuation in the absolute calibration of the 94 GHz radiometer occurred when the instrument's ambient temperature fell outside the 25°C to 35°C range. Note will be made in the data analysis if the operating range was exceeded.

2.3 Ground Truth Instrumentation

This section covers description of the snow sampling, soil sampling, and atmospheric measuring equipment.

2.3.1 Snowpack Conditions

The following parameters were measured for the snowpack:

1. Depth
2. Density
3. Wetness
4. Temperature
5. Stratification
6. Grain size, shape and texture
7. Surface roughness

Figure 13. Calibration curve of 37 GHz V-polarization radiometer.

Figure 12. Calibration curve of 37 GHz H-polarization radiometer.

22
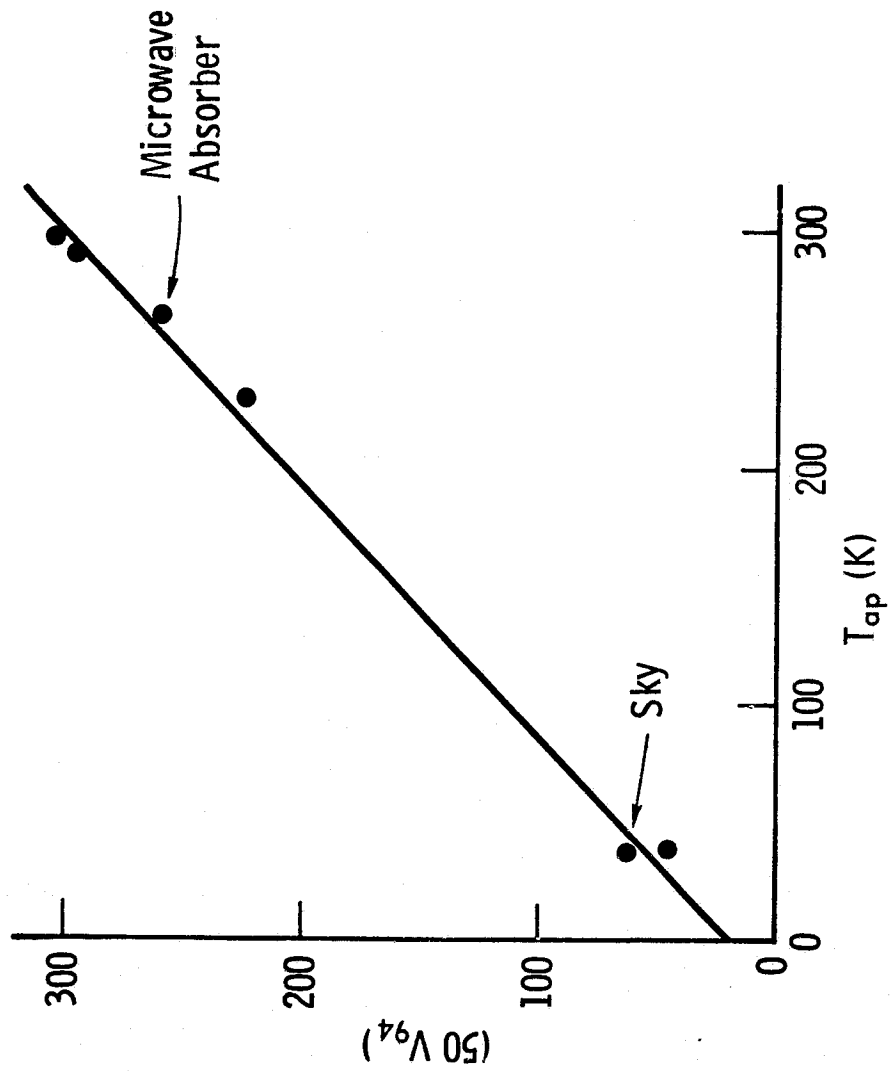
Figure 14. Calibration curve of the 94 GHz radiometer.

23

2.3.1.1 Snow Depth

Two permanent gauging stations, shown in Figure 3 , were located on opposite ends of the test plot. These stations were monitored twice daily. Figure 15 is a photograph of one of the stations.

2.3.1.2 Snow Density

Snow density profiles were obtained using a horizontal sampling technique. Figure 16 illustrates the sampling and weighing procedures. Also, the standard vertical (Mount Rose snow tube) sampling technique was used periodically. It was determined that for detailed snowpack analysis the horizontal sampling technique was easier to use and had better accuracy.

2.3.1.3 Snow Wetness Measurement

Since one of the major parameters affecting the microwave properties of the snow is free water, two methods were employed to measure wetness.

2.3.1.3.1 Capacitance Measurement of Snow Wetness

The use of a capacitor to measure the free water content of snow was proposed by Linlor [9] who loaned us his equipment for this experiment. The amount of free water in the snow affects the dielectric constant of the snow capacitor and thus its Q and capacitance. Figures 17 and 18 show the experimental relationships between dielectric constant or Q and the amount of free water. The response of dielectric constant and therefore capacitance is a linear function of wetness. Determination of wetness from capacitance is simpler than using the Q because of linearity. Also, low frequencies give the most sensitivity to wetness. Figure 19 illustrates the variation of capacitance and Q with frequency. A trade off is involved between sensitivity (low frequency desirable) and Q (high frequency desirable). The problem with using Q measurements alone is that the structure of the snow and of the capacitor will affect the Q. Therefore an alternative is to measure the change in capacitance between a snow sample with free water, and the same sample after freezing with dry ice. For this case, the change in capacitance will be independent of structure and only a function of the free water. The measurements of capacitance and Q were made with an HP-4342A Q-meter at the following frequencies: 100 KHz, 230 KHz, 500 KHz, 1.0 MHz and 3.2 MHz. Figure 20

24
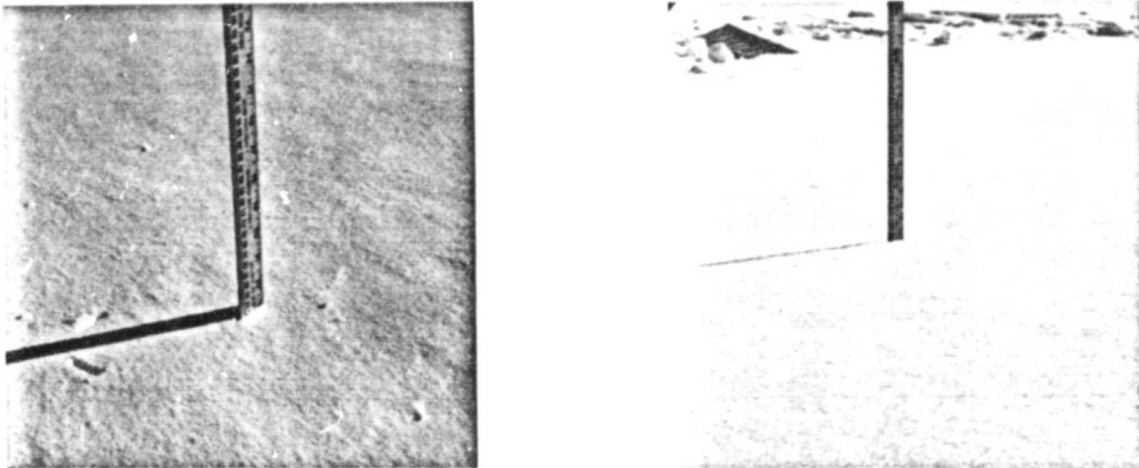
Figure 15. Snow depth measurement.
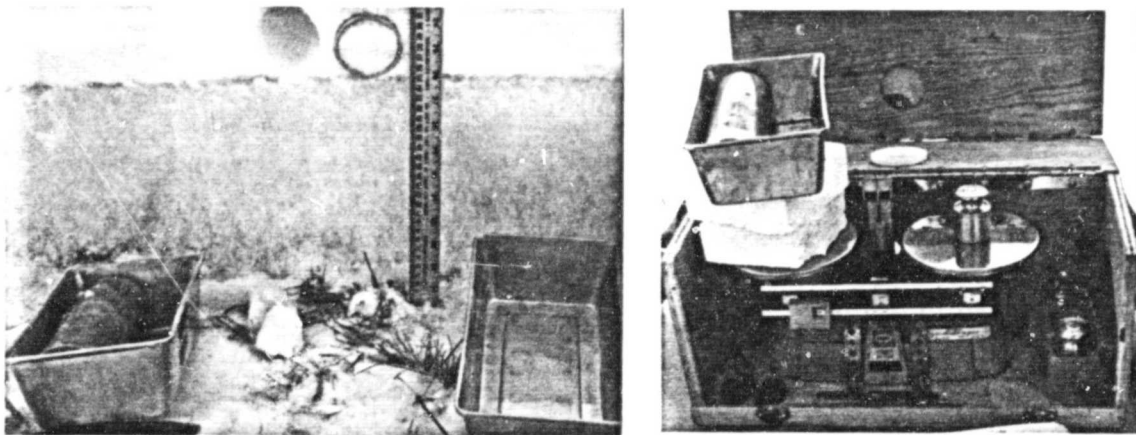
Figure 16. A given volume of snow was removed from each snow interval
with an aluminum cylinder of known volume (500 cc) and
placed in a pan. The pan, snow and cylinder were trans-
ported to the balance and weighed. The data were then
recorded for the appropriate date and time.
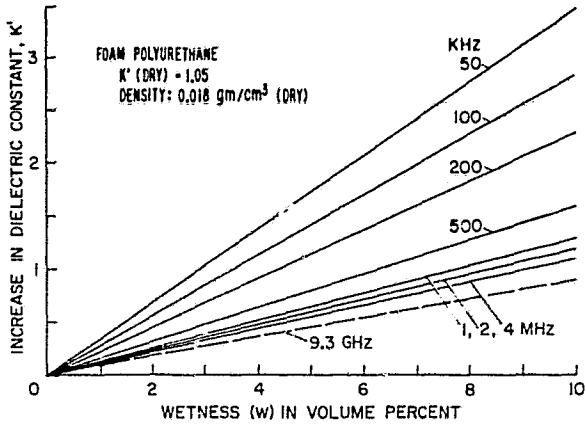
FIG. 17. DEPENDENCE OF DIELECTRIC CONSTANT ON WETNESS [9]
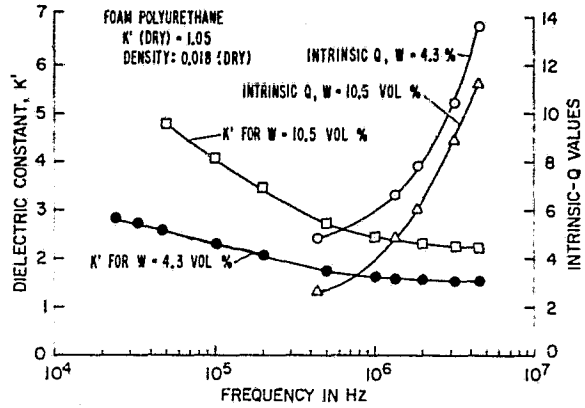
FIG. 19. DEPENDENCE OF DIELECTRIC CONSTANT ON FREQUENCY [9]
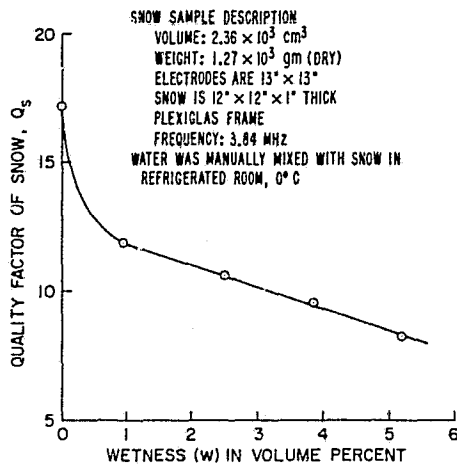
FIG. 18. QUALITY FACTOR OF SNOW CAPACITOR VERSUS WETNESS [9]

26

(a) Obtaining sample.

(b) Preparing snow capacitor.

(c) The filled snow capacitor.
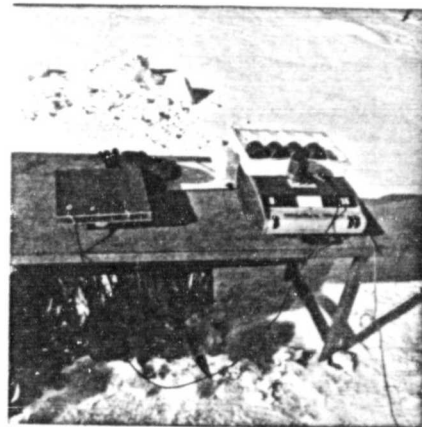
(d) Measurement of capacitance
and Q showing Q-meter,
inductors and snow
capacitor.

Figure 20.   Capacitor Sampling Procedure.

shows the procedure used in obtaining samples and making the
measurements with the Q-meter. At a given frequency, the change in
capacitance is given by:

$$\Delta C = C_s - C_f$$

$$= A C_o W \tag{20}$$

where

C_s = capacitance with snow sample

C_f = capacitance after freezing snow sample

C_o = capacitance of empty capacitor

A = calibration constant

W = volume percent wetness

The quantities C_s, C_f and C_o are measured for each sample but the
calibration constant A has not yet been determined. Thus, at this time
the capacitance method provides a measure of free water content on a
relative scale only.

2.3.1.3.2 Calorimeter Measurement of Snow Wetness

The calorimetric method of measuring snowpack wetness was investi-
gated by Leaf [10]. Either a freezing or melting calorimeter could have
been used. However, for snowpack wetness the freezing calorimeter is
more accurate. The calorimeter is an insulating container with provisions
for measuring the temperature. A known amount of toluene (cooling
agent) is allowed to reach equilibrium inside the calorimeter, then the
wet snow is added and the solution is again allowed to reach equilibrium.
Figure 21 shows the cold calorimeter and Figure 22 shows the procedure
used in obtaining the samples and performing the calorimeter measurements.
If the calorimeter is assumed lossless, heat will be conserved between
initial and final states:

$$H_i = H_f \tag{21}$$

where

H_i = initial heat content of all constituents

H_f = final heat content of solution

28

Figure 21. The cold calorimeter, used for measuring the amount of free water present in a sample of snow, consists of a thermos bottle with a thermocouple probe inserted through the lid and extending down into the central cavity of the thermos.
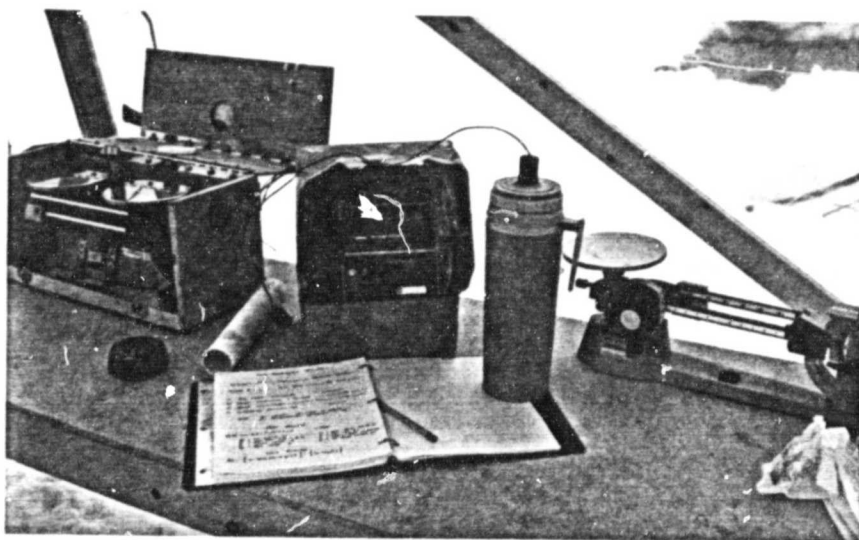
Figure 22. The temperatures of the solution were recorded using a digital thermometer, and the weights of snow and toluene were measured.

The heat content of the final solution of toluene and ice is

$$H_f = t_f(W_i+E) C_{tf} + t_f S C_{sf} \qquad (22)$$

where

t_f = final equilibrium temperature

W_i = weight of toluene

E = calorimeter constant

S = total weight of snow

C_{tf} = specific heat of toluene at t_f

C_{sf} = specific heat of ice at t_f

The two terms are the heat content of the toluene and calorimeter, and the heat content of the ice. The heat content of the initial constituents (toluene, snow, free water) is

$$H_i = t_i(W_i+E) C_{ti} + LF + t_sDC_s + t_sFC_w \qquad (23)$$

where

t_i = initial temperature of toluene

t_s = snow temperature

F = weight of free water in snow

D = weight of dry snow, $S = D + F$

C_{ti} = specific heat of toluene at t_i

C_s = specific heat of snow at t_s

C_w = specific heat of water at t_s

L = heat of fusion of water = 79.7 cal/g

The first term of Equation (23) is the initial heat content of the toluene and calorimeter and the second term is the heat required to change the state of the free water. The third term is the heat content of the ice component of the snow and the last term is the heat content of the free water in the snow. If the temperature of the snow (t_s) is less than 0°C, then the last term of Equation (23) should be changed to t_sFC_s.

30

Solving for the fraction of free water

$$T = \frac{F}{S} = \frac{\left(W_i + E\right)\left(t_f \, C_{tf} - t_i \, C_{ti}\right)}{S\left(t_s \, C_w - t_f \, C_{sf} + L\right)} + \frac{\left(t_f \, C_{sf} - t_s \, C_s\right)}{\left(t_s \, C_w - t_f \, C_{sf} + L\right)} \tag{24}$$

2.3.1.4 Snow Temperature

Temperature profiles of the snowpack were measured at 10 cm height intervals using thermisters incased in PVC tubing. The thermisters were measured with a bridge circuit that read out in degrees Celcius. Profiles were also obtained with a Doric digital thermometer and thermocouples at 2 cm intervals. Figures 23a and 23b show these two instruments.

2.3.1.5 Stratification

Snow stratification or layering is illustrated in Figure 24. Location, thickness and boundaries were measured for each layer. A vertical face is cut in the snow-pit sampling area to expose the layers. The layer thicknesses were then measured and photographs taken.

2.3.1.6 Grain Size, Shape and Texture

Photomicrographs were used to record the grain sizes, shapes and structural relationships for each layer. Figure 25 shows the microscope and light source.

2.3.1.7 Surface Roughness

Surface roughness was recorded by photographing a metal grid inserted into the snow. Figure 26 shows the panel in use. This particular snow condition occurred after high winds.

2.3.2 Soil Conditions

The soil temperature was measured at the soil surface and at 5 cm below the surface with the Doric thermometer. Temperature was also monitored at the surface, 2 cm and 5 cm below the soil surface with the thermister bridge meter. Late in the measurement period when the soil was thawed, soil moisture samples were taken. These samples were dried in a microwave oven to determine the soil moisture content.

a)   (b
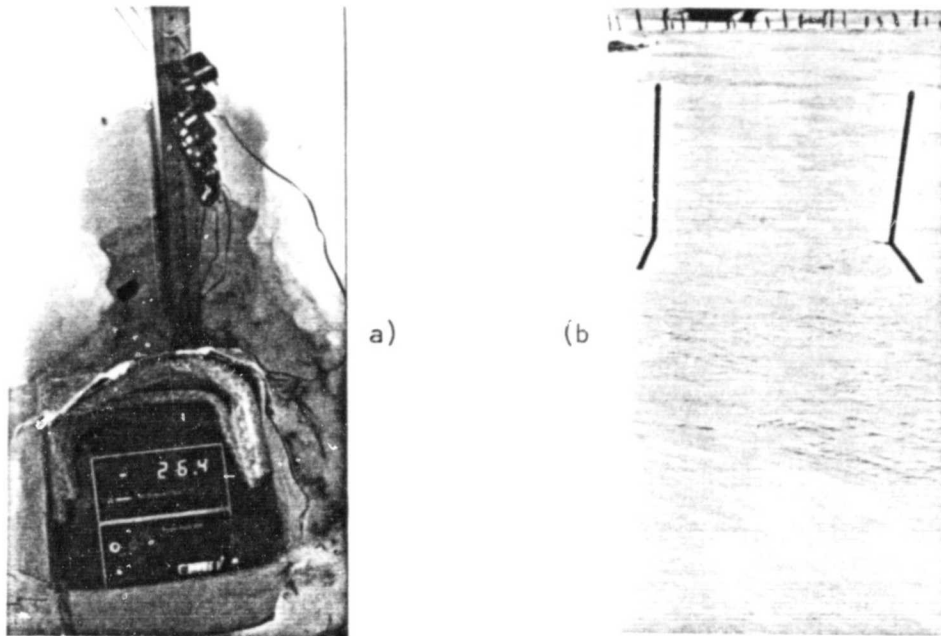
Figure 23a) Temperature was measured at 2 cm intervals with
             thermocouple probes and a Doric digital thermometer.
             b) Temperature was also measured at 10 cm intervals using
             thermisters encased in PVC tubing.
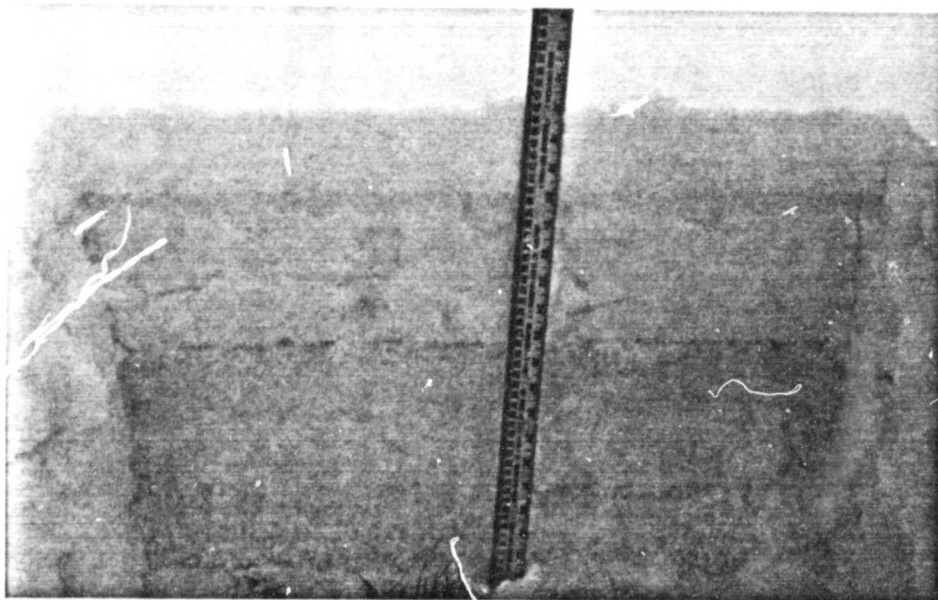
Figure 24.   Snow stratification profiles were measured.
             This photograph shows three distinct layers.
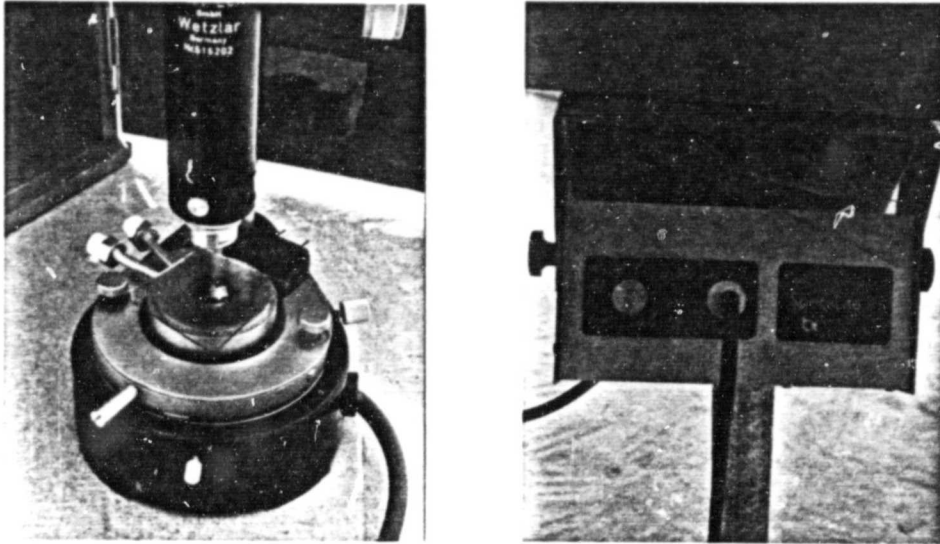
Figure 25. Photomicrographs of the snow were made using
a fiberoptic light source. This technique
was successful because of the cold light
source characteristics of the fiberoptic
system.
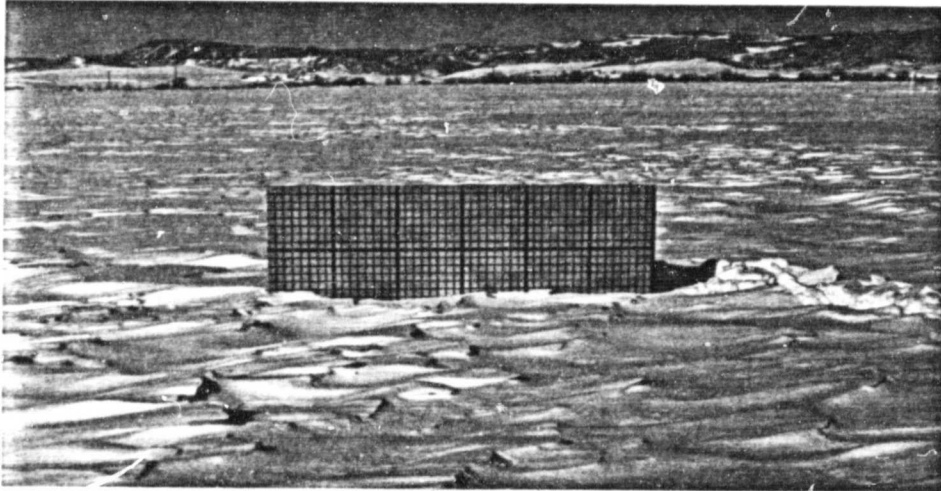
Figure 26. Surface roughness was measured by inserting
a ruled panel vertically into the snow and
photographing the surface irregularities
superimposed against it.

2.3.3 Atmospheric Conditions

A weather station was installed at the test site to continuously record temperature, relative humidity, and barometric pressure. Figure 27 shows the weather station. Two pyronameters were used to measure both incident and reflected solar radiation. Figure 28 shows the pyronameters.

2.4 Data Acquisition

This section describes the specific experiments performed to better understand the microwave characteristics of snowpacks.

2.4.1 Daily Backscatter and Emission Measurements

The daily data sets covered a more complete set of sensor parameters than the special experiments. The MAS 1-8 and MAS 8-18/35 operated at all frequencies and polarizations. The incidence angles observed were: 0°, 10°, 20°, 30°, 50° and 70°. Spatial averaging was employed to reduce the effects of fading. The radar returns from 20 resolution cells were averaged at 0°. The number of spatial samples was decreased with increasing angle to a minimum of five at 70°. The microwave radiometers measured five cells at each angle of incidence. In addition to the remotely sensed data, ground truth was taken with each set.

Between one and three daily sets were obtained depending on snow conditions and equipment status. Approximately three hours were required per data set. The desired time period for the daily sets were predawn, noon and late afternoon. These time periods cover the widest range of snow conditions within one day.

2.4.2 Diurnal Backscatter and Emission Measurements

Four diurnal data sequences were conducted. This measurement program was implemented to observe short term variation in snow conditions such as appearance of free water in the snowpack and structural changes within the layers. Each diurnal experiment consisted of continuous data acquisition over a 28 hour period commencing at 6:00 am.

To improve the temporal resolution of the variations under observation, the time span of an individual data set was reduced by reducing the number of system parameters at which measurements were made.
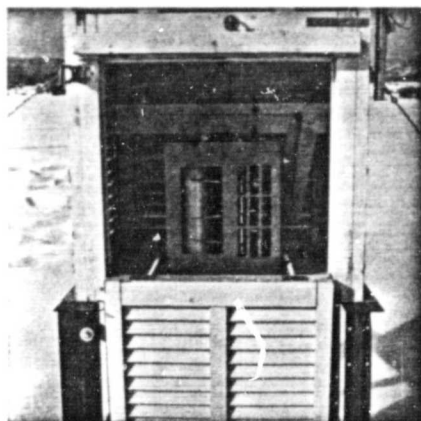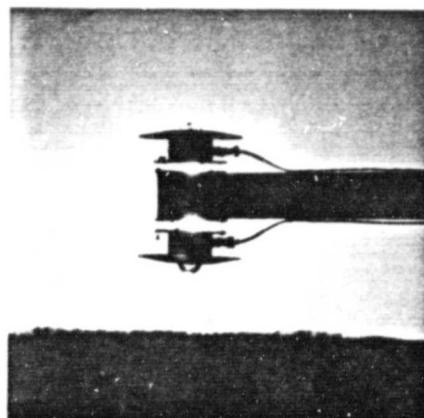
Figure 27.   Figure 28.

Figure 27.   The weather station was equipped with a Meteorgraph
(model 701, Weather Measure Corp., Sacramento, Ca.)
which recorded temperature, relative humidity and pressure.

Figure 28.   Two pyronameters (model SR71, Spectrolab, Inc.) mounted
back to back enabled measurements of incident and reflected
solar radiation.
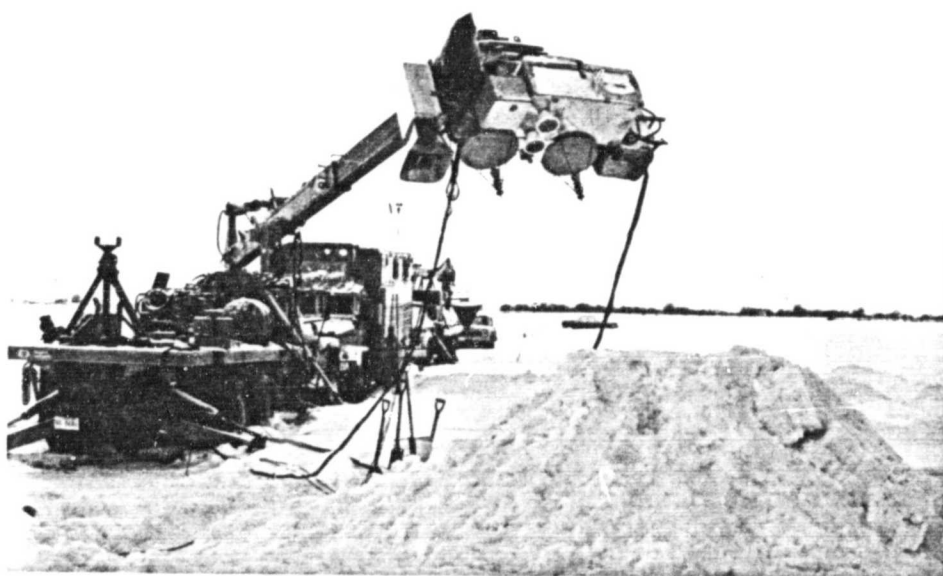
Figure 32.   MAS 8-18/35 and radiometers during one of
the snowpile experiments.

Generally, only HH polarization was observed with the exception of the 35.6 GHz scatterometer for which all polarizations were measured. Also, only 0°, 20° and 50° angles of incidence were sampled. The time span for a data set was reduced to approximately 1.5 hours. For the last two diurnals, only 50° data were acquired and the time span was approximately 0.75 hours. The ground truth data sets were obtained at hourly intervals except for the calorimeter and capacitance measurements which required a slightly longer duration.

2.4.3 Attenuation

One basic question to any study of snow is that of penetration. Is the microwave response related only to the snow (and to what depth beneath the snow surface) or is there a contribution by the underlying ground? To measure this attenuation, two boxes for each radar system were placed in the field before the first snowfall. Figure 29 illustrates the placement. The MAS 1-8 and MAS 8-18/35 were used as transmit sources. The one-way path loss was measured with a small 2-8 GHz spiral and a 12.4-18.0 GHz waveguide horn and a Boonton power meter. Figure 30 shows the measurement system. The power loss was measured at six frequencies in the 2-8 GHz band and at five frequencies in the 12.4-18.0 GHz band for two snow thicknesses. The one-way loss is not totally due to attenuation, in fact for low loss cases, the dominant loss factor may be mismatch at the snow-air interfaces. Using multiple frequency measurements for each of two layers may allow separation of attenuation and mismatch.

Also, an experiment was carried out independently to measure attenuation at 35 GHz. The path loss in this case was measured horizontally. Readings were taken for varying snow thicknesses and for three snow conditions. Figure 31 illustrates the layout. A signal generator and doubler were used for a transmit source. The receiver consisted of a crystal detector and a VSWR meter. Due to some equipment problems, sensitivity was limited. Alignment of the antennas was by manual peaking of the VSWR meter.

2.4.4 Single Cell Diurnal Fluctuation Measurement

This experiment is a variation on the diurnal experiments already described. In this case it was desirable to observe the microwave
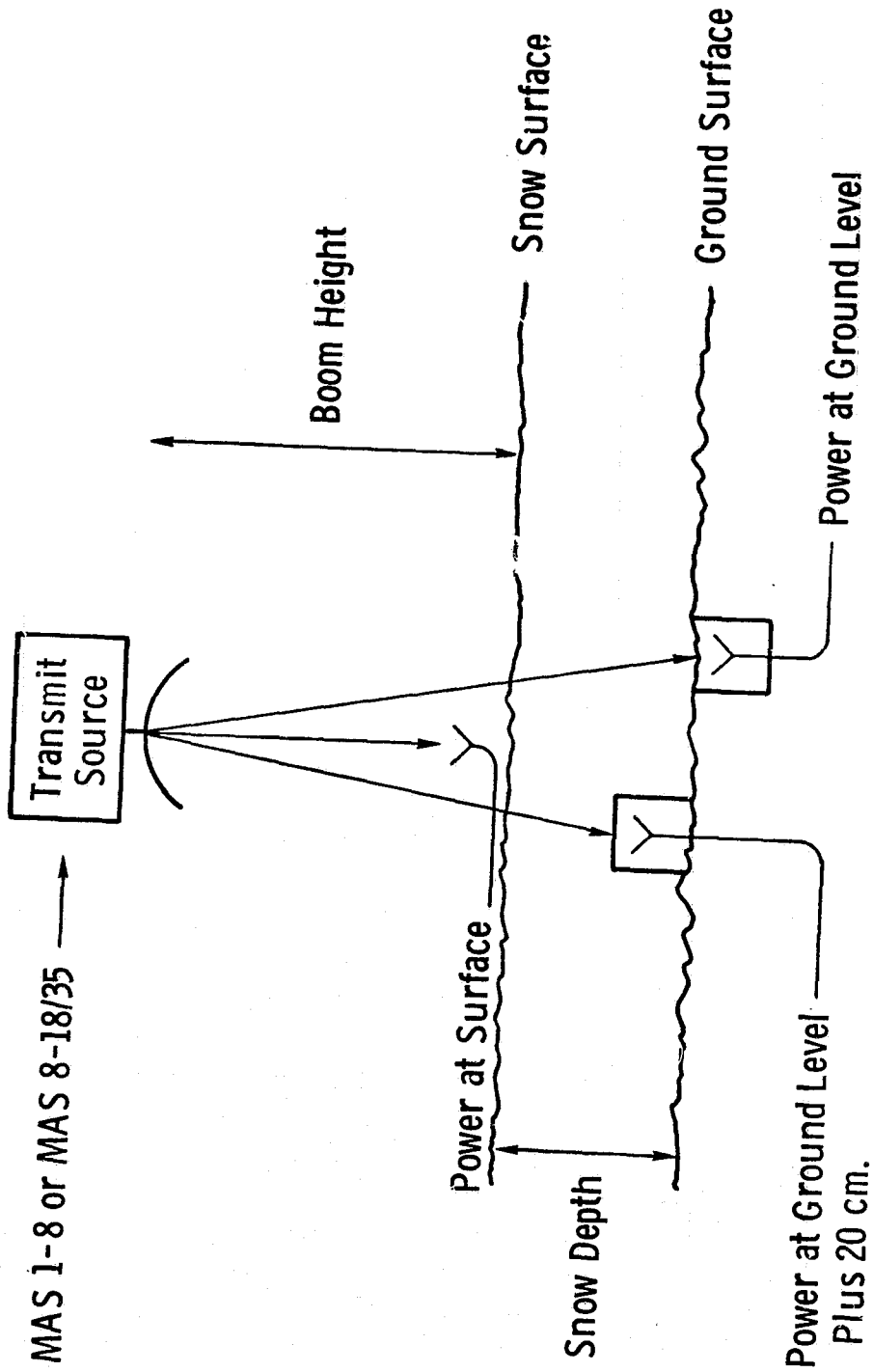
Figure 29. Diagram illustrating the attenuation measurement procedure.
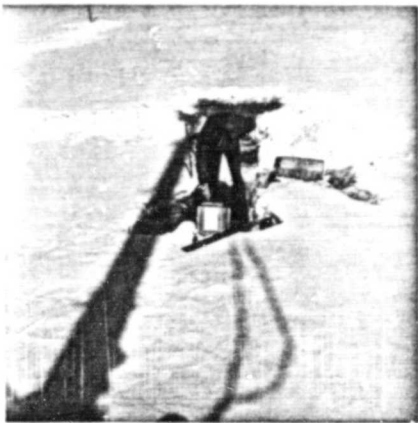
a) Attenuation pit showing
   the power meter, antenna
   and shadow of the
   MAS 8-18/35 transmit source.

b) Surface level power
   measurement.
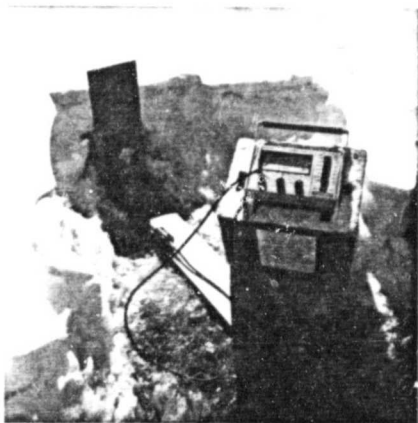
c) Closeup of the antenna
   and power meter and
   antenna box at +20 cm
   above ground level.

d) Closeup of the receive
   horn.

Figure 30.   Attenuation measurement.
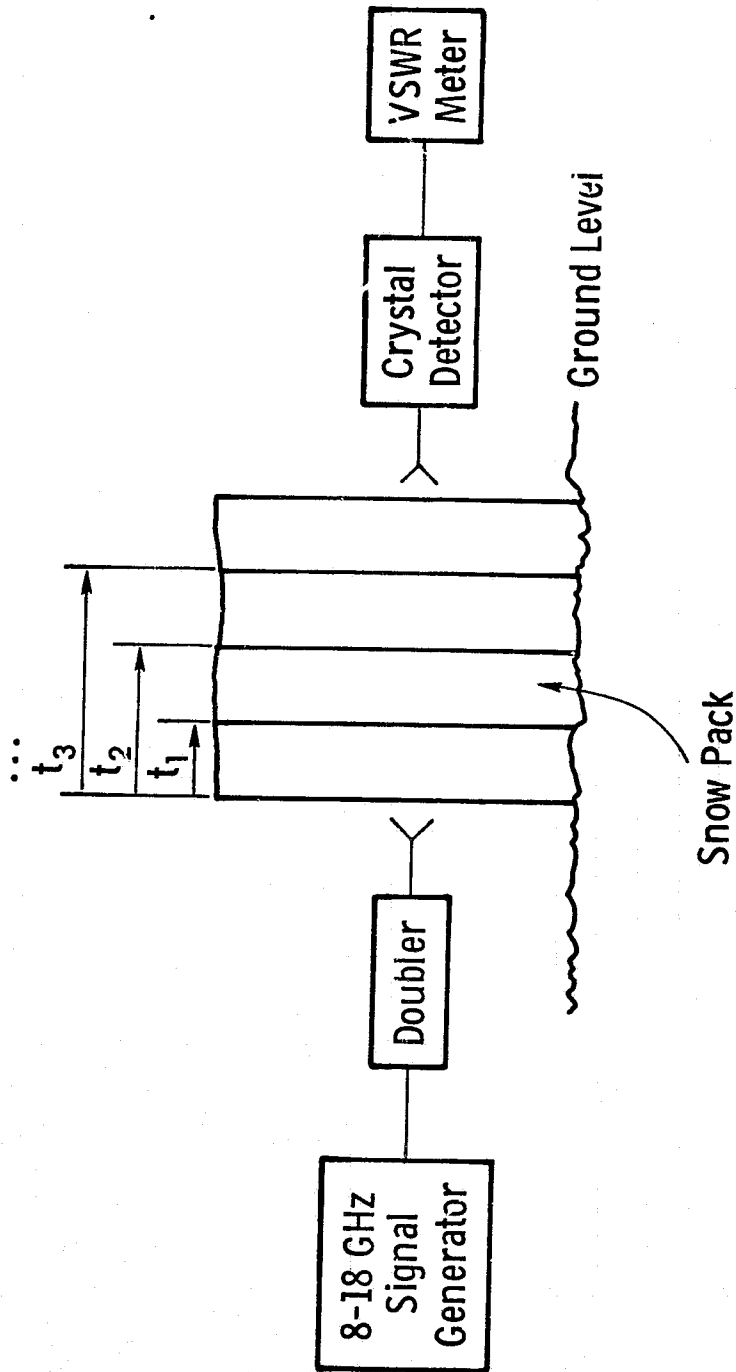
Figure 31. Diagram illustrating the procedure used to measure the attenuation of the snow at 35.6 GHz as a function of layer thickness (t).

response for a single observation cell. The look direction and position were therefore set and the scattering and emission properties measured for 12 hours during the daytime. Measurements at all polarizations and frequencies were taken at 50° and 70° angles of incidence.

2.4.5 Snowpile Experiment

The winter of 1976-1977 was the most severe drought in the last 10 years in Colorado and as a result the snowpack in the test area reached a maximum of only 57 cm. To test the microwave response to snow-depth, an artifical snowpack was created by piling snow up to depths of 144 and 170 cm (two experiments were conducted). Figure 32 shows a photograph of the MAS 8-18/35 and radiometers in operation during this experiment. Since the size of the target allowed only one independent look (spatially), emphasis was placed on acquiring radiometric measurements. MAS 8-18/35 data were acquired, however the error bars are quite large due to signal fading. Ground truth was obtained in conjunction with the microwave measurements.

3.0 FADING

Fading is a result of constructive and destructive interference of the signal components of the scattering elements within the resolution volume. This fluctuation complicates the study of the scattering properties of a target. A single measurement of the return power therefore can only give an estimate of the target properties. In general, unless the target can be described exactly, the fading contribution is unknown. In most radar measurements, fading has the effect of introducing an uncertainty in the estimated value. For example, fading can cause degradation in the probability of detection of a search radar. The speckle in a radar image is the result of fading. Similarly, the precision of radar cross section measurements with a scatterometer is limited by fading. Averaging of independent measurements provides fading reduction and hence a better estimate of the target radar cross section. If the target is area extensive and homogeneous, spatial averaging can be employed. Also, excess system bandwidth can be used to give more than one independent sample per measurement. A combination of both spatial and frequency averaging can also be used.

One of the original investigations into fading was performed by Marshall and Hitshfeld [11]. Later, Swerling [12] developed models to investigate the effect of radar cross section fluctuation on the probability of detection. Several different types of statistical distributions have been proposed and used to account for the effects of signal fading. If the power returned from a single scatterer is large compared to the power from all of the remaining scatterers of the target, the Rice distribution [13] is used to describe the statistics. If, on the other hand, the target is assumed to consist of a large number of scatterers of approximately equal backscatter amplitude, the Rayleigh distribution is applicable. The Rayleigh distribution has been widely used for terrain surfaces and has been shown to provide good agreement with experimental results [14,15].

3.1 Rayleigh Fading Statistics

If a target is area extensive and can be represented as a large collection of approximately equal amplitude scatterers, then the resultant signal voltage can be represented as a phasor summation over all the scatterers in the resolution volume (Figure 33):

$$E_t = V e^{j\theta} = \sum_n E_k e^{j\phi k} \qquad (25)$$

where

E_t = resultant signal voltage

V = resultant magnitude

θ = resultant phase

E_k = single element amplitude

ϕ_k = single element phase

n = number of scatterers

The signal can then be separated into its components:

$$X = V \sin \theta = \sum_n E_k \cos \phi_k \qquad (26)$$

$$Y = V \cos \theta = \sum_n E_k \sin \phi_k$$

If E_k and ϕ_k are uncorrelated, it has been shown that the probability density function of the signal voltage V is given by [15]:

$$P(V) = \frac{2V}{\alpha} e^{-V^2/\alpha} \qquad (27)$$

which is recognized as the Rayleigh density function with α being the variance of V. Since power W varies as the square of the voltage,

$$W = K V^2 \qquad (28)$$
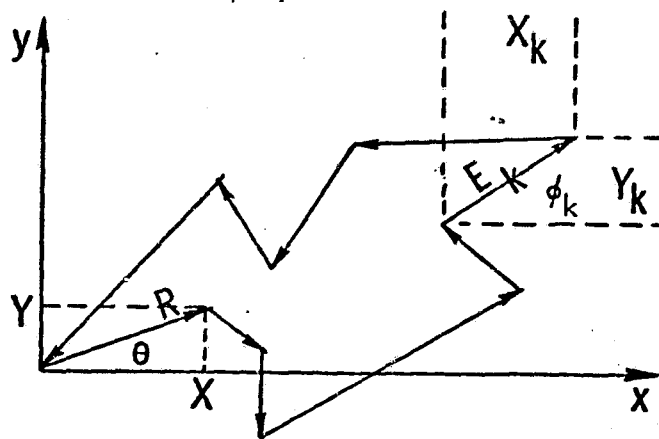
Figure 33.   Diagram showing scattered $\bar{E}$ field components.

the density function of W can be obtained from the condition:

$$P(W) \, dW = P(V) \, dV \tag{29}$$

which yields:

$$P(W) = \frac{1}{2\sigma^2} \, e^{-W/2\sigma^2} \tag{30}$$

where α has been set equal to $2\sigma^2$. Equation 30 is the power Rayleigh density function or chi-square distribution with two degrees of freedom. The general chi-square density function with i degrees of freedom is given by:

$$P_i(W) = \frac{1}{2^{i/2} \, \sigma^i \, \Gamma\left(\frac{i}{2}\right)} \, \exp\left(\frac{-W}{2\sigma^2}\right) \, W^{\frac{i}{2}-1} \tag{31}$$

The distribution for one independent sample is therefore chi-square with two degrees of freedom.

If N samples from the distribution are averaged,

$$\overline{W} = \frac{1}{N} \sum_{k=1}^{N} W_k \tag{32}$$

The probability density function of $\overline{W}$ is a gamma density function and is given by [15]:

$$P_N(\overline{W}) = \frac{N^N \, \overline{W}^{N-1}}{2^N \sigma^{2N} \, \Gamma(N)} \, \exp\left(\frac{-N \, \overline{W}}{2\sigma^2}\right) \tag{33}$$

The above distribution has the following important properties:

$$\mu_{\overline{W}} = E[\overline{W}] = 2\sigma^2 \tag{34}$$

$$\sigma_{\overline{W}}^2 = E[\overline{W}^2] = \frac{4\sigma^4}{N} \tag{35}$$

44

Hence the variance to the square of the mean ratio is given by:

$$\frac{\sigma_{\overline{W}}^2}{\mu_{\overline{W}}^2} = N \qquad (36)$$

Figure 34 presents plots of $P_N(\overline{W})$ for several different values of N.

3.2 Fading Reduction

Marshall and Hitschfeld [11] evaluated the statistical independence of fading with respect to time, range, aspect and frequency. Moore, Waite and Rouse [16] proposed that bandwidth, in excess of that required for resolution, could be used to reduce variations due to fading. If the bandwidth of the measurement system is large such that the signal return decorrelates in frequency, more than one independent sample may be obtained from one measurement [17]. Waite [17] showed that the required frequency spacing to decorrelate and thus given independence was

$$\Delta f_d = \frac{150}{D} \qquad MHz \qquad (37)$$

where D is in meters. D is the maximum range variation across the resolution volume. Waite performed an experiment to show the effects of averaging in frequency. Figures   and   show the variation in scattering coefficient for two targets and two effective bandwidths. Notice the decrease in fading with increasing bandwidth.

Improvement in measurement precision through the use of frequency averaging is determined by the number of independent samples provided by the frequency bandwidth ΔF employed in the averaging process:

$$N_f = \frac{\Delta F}{\Delta f_d} \qquad (38)$$

where N_f is the number of independent samples per measurement due to

45
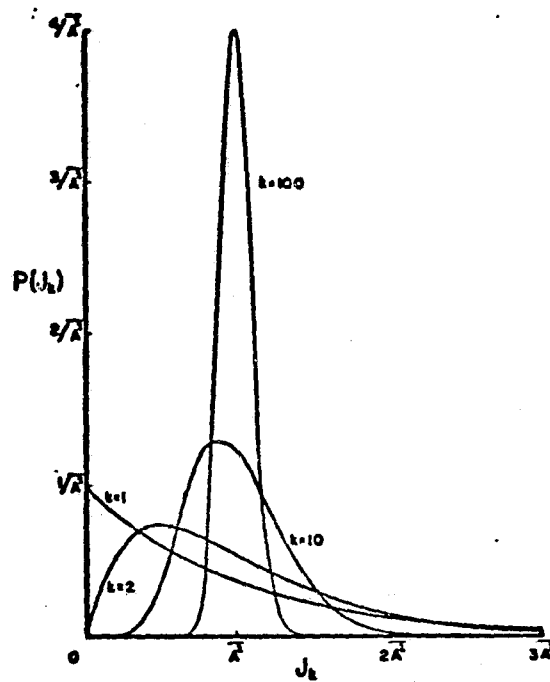
Figure 34. Chi-square probability distribution for three
different values of k, the number of degrees
of freedom [11].

46
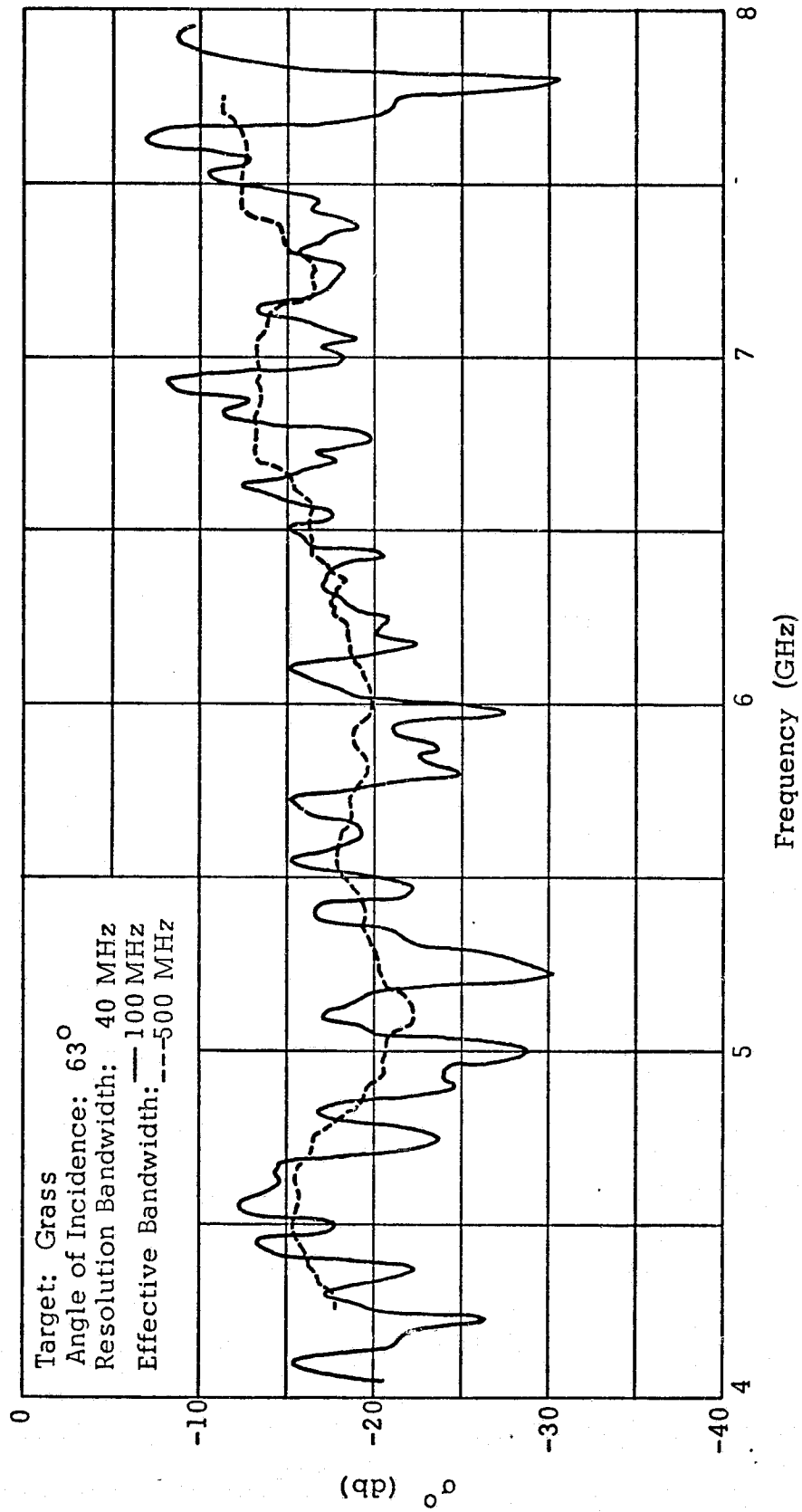
Figure 35. Spectral response curves for two different effective bandwidths. [17]
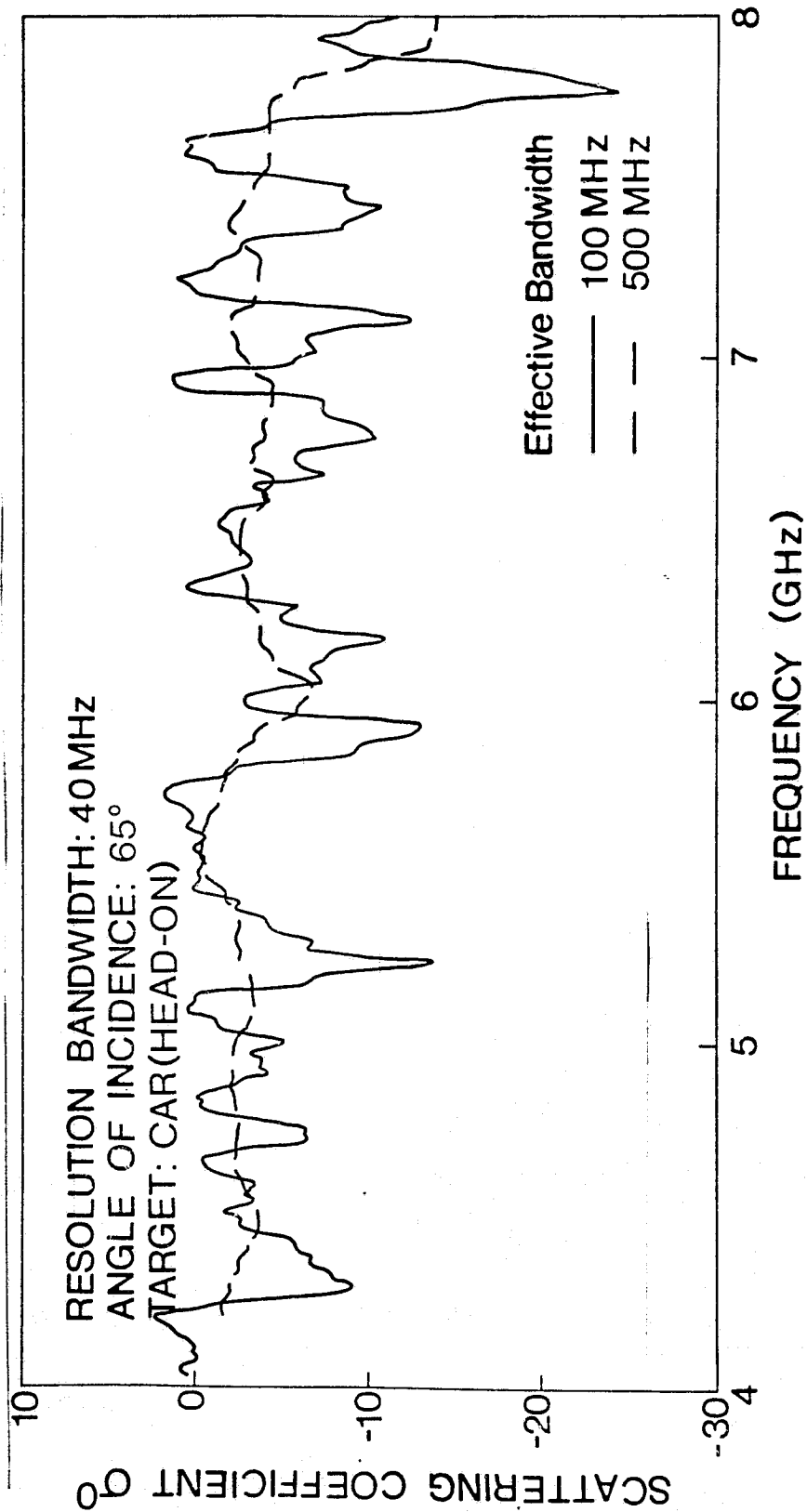
Figure 36. Spectral response curves for two different effective bandwidths. [17]

48

frequency averaging. Figure 37 shows the frequency distributions of the measured radar scattering coefficient of three different cases. In each case the value of N calculated on the basis of the measured values and the value calculated on the basis of Equations 37 and 38 are indicated.

If in addition to frequency averaging, spatial averaging is also used, the total number of independent samples is given by

$$N = N_s N_f \tag{39}$$

where N_s is the number of independent spatial measurements. Once N is determined, the variance of $\overline{W}_N$ can be calculated from Eq. 36 and the desired confidence interval can be calculated from gamma density function tables. As an example, the 5% and 95% probability levels are shown in Figure 38 as a function of N.

Under certain conditions, averaging returns over time will give independence. In the case of a stationary radar observing the ocean, wave motion provides a continuously varying observation area therefore for a single look direction averaging in time is effective. However, for the case of a stationary radar and stationary target, the relative phases of the scatterers (ϕ_k in Eq. 25) will remain constant and the returns will be completely correlated.

Variation in aspect angle can also provide independent samples if the angular change is sufficient. Spatial averaging may be employed to give independence and reduce fading. The assumption is made that returns from non-overlapping cells are independent and that the target is homogeneous over the areas of observation. Averaging may be applied either in azimuth or range. Averaging in range, however, is valid only for high incidence angles where the magnitude of the scattering coefficient is known to be slowly varying with angle.

3.3 Measurement Precision

The MAS 8-18/35 operates at 11 frequencies over the 8-18 GHz band and at 35.6 GHz. Table 2 and Table 4 give the system specifications and antenna beamwidths at selected frequencies. Figure 39 shows the geometry of the illuminated cell in the elevation direction.
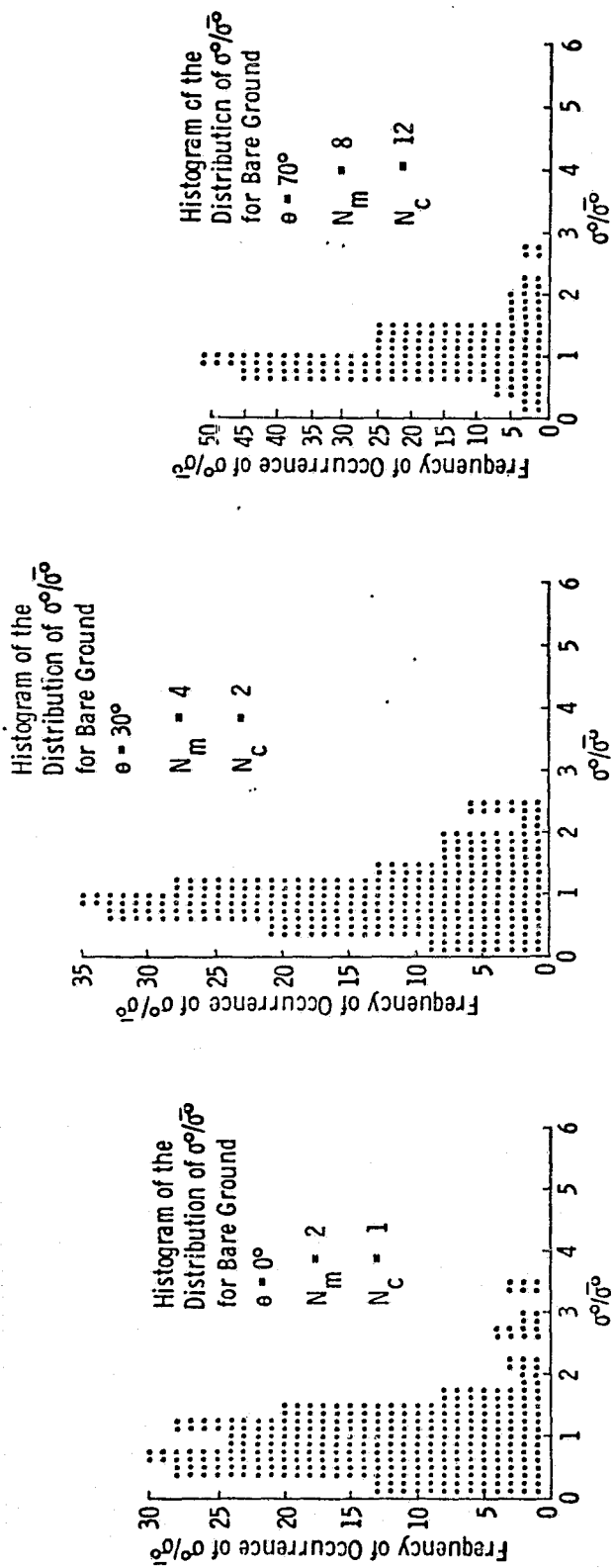
Figure 37. Histograms of σ^o for bare ground normalized by $\bar{\sigma^o}$, the mean value of σ^o. N_m is the number of independent samples based on the measured data and N_c is the number calculated on the basis of Rayleigh fading.
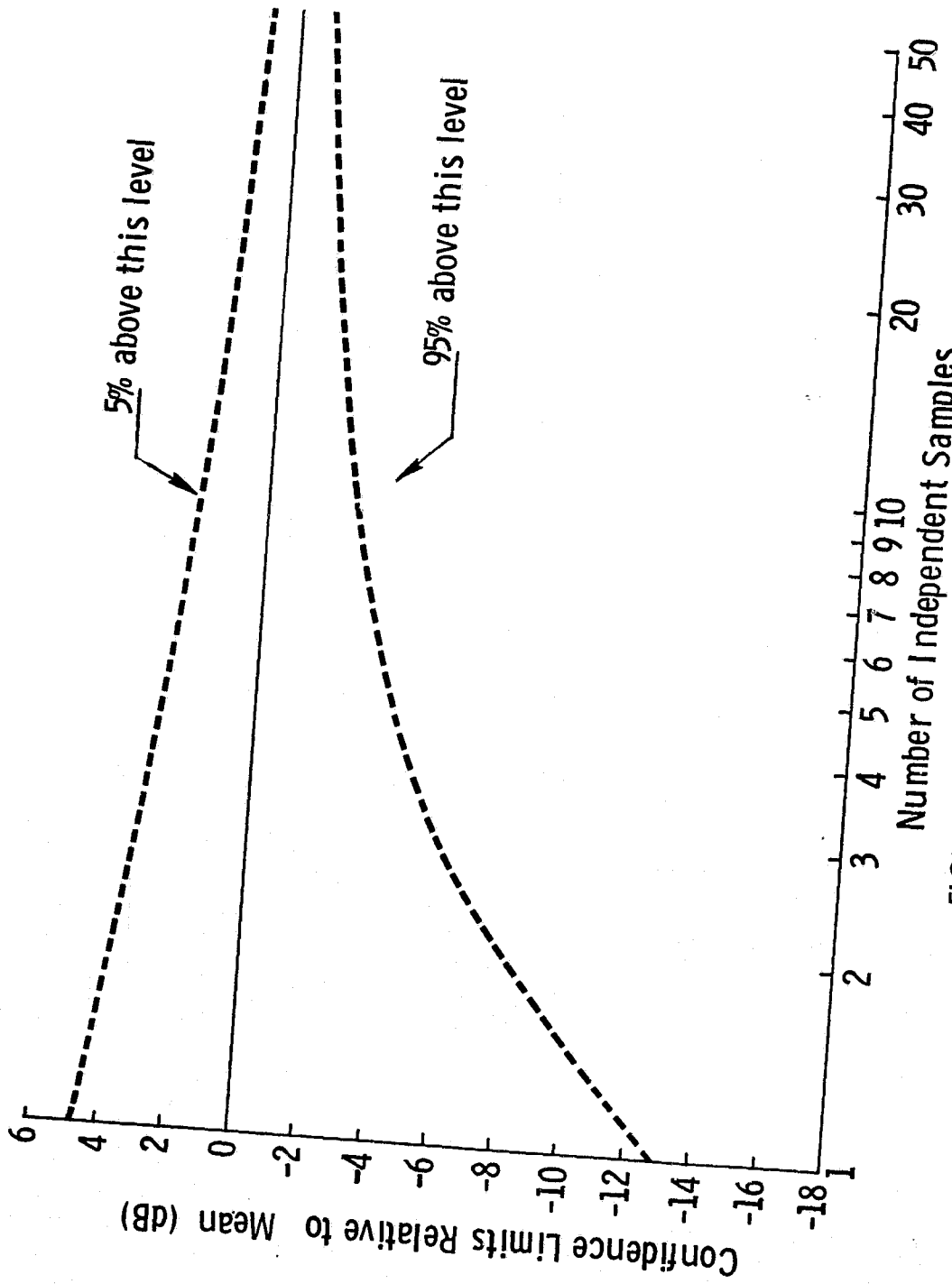
FIGURE 38. 90 PER CENT CONFIDENCE INTERVAL
FOR RAYLEIGH DISTRIBUTION.
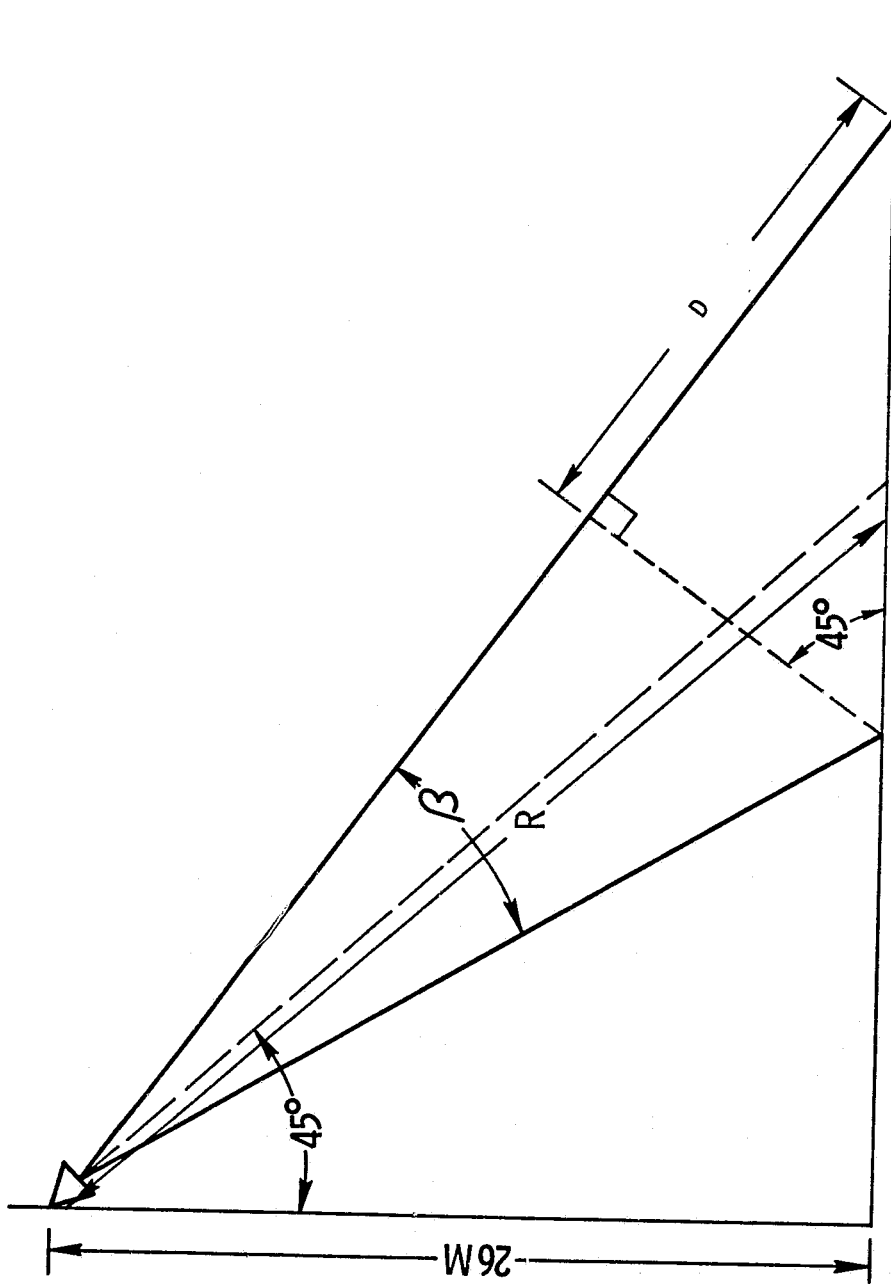
Figure 39. Illustration defining D: the range resolution afforded by the antenna beam.

TABLE 4.   MAS 8-18/35 Antenna Beamwidths

Antenna Product Beamwidths

8.6 GHz, HH polarization	3.6°
17.0 GHz, HH polarization	1.7°
35.6 GHz, HH polarization	3.0°
Antenna Height	26 m

Table 5 is a summary of the calculated values of the various param-
eters leading to the 90% confidence intervals with and without spatial
averaging. The 90% confidence interval is defined by two values, both in
dB with respect to the mean. The lower value represents the level at
which the probability that it will be exceeded is 95% and the higher
value represents the level at which the probability that it will be
exceeded is only 5%. The need for spatial averaging is most apparent at
nadir where frequency averaging does not appear to provide any increase
in the number of independent samples. In practice, however, the assumption
that no penetration into the medium takes place and that the surface is
perfectly smooth are too conservative and hence the effective number of
independent samples is usually between 2 and 4 [15]. On the other extreme,
the confidence interval with spatial averaging at 70° is smaller than the
system stability factor estimated to be about $\pm$ 0.5 dB.

3.4   Measurement Variability with a Pulsed Radar

Like the FM-CW system, a pulse system can have the capability to
provide more than one independent sample per look. If the return from
a chirp pulse is not processed for the best range resolution, multi-
samples may be obtained from one pulse. However, most systems are
monochromatic and will have the bandwidth matched to the pulse width.
Under the above circumstance , only one independent sample is obtained
per look.

Consider a pulse radar with a pulse width τ (Figure 40) and a
matched IF bandwidth $\Delta F_{IF} = 1/\tau$. The maximum range resolution across
a resolution cell is:
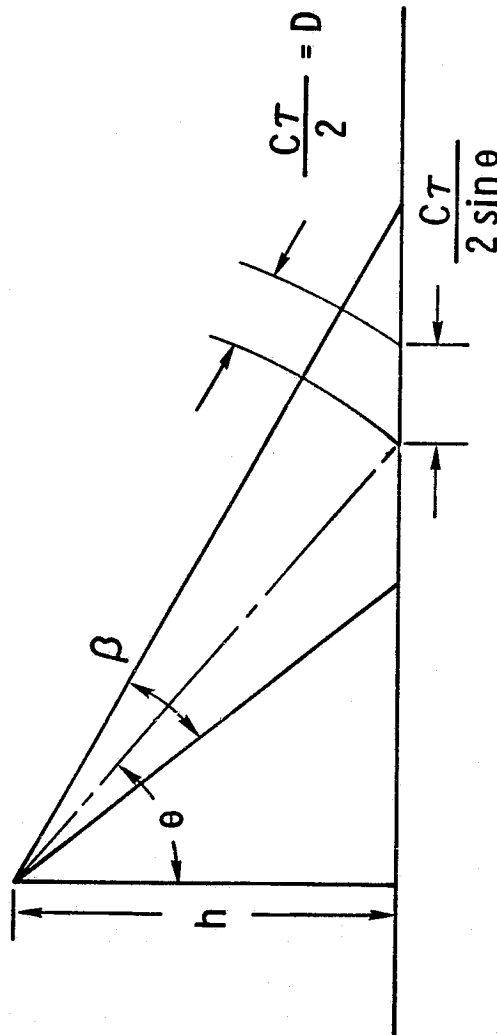
τ – Pulse Width

Figure 40. Diagram illustrating elevation plane geometry for a pulsed radar.

TABLE 5. Calculated values of 1) Range variation d (Figure 39), 2) Decorrelation Δf_d (Eq. 37), 3) Number of independent samples provided by frequency averaging N_f (Eq. 38), 4) 95%/5% confidence interval for N_f samples (Figure 38 for $N=N_F$), 5) Number of spatially independent samples acquired N_s, 6) Total number of independent samples $N=N_f \times N_s$, 7) 95%/5% confidence interval for N samples (Figure 38).

Angle of Incidence	D(m)	Δf_d (MHz)	N_f	95%/5% for N_F samples	N_s	N	95%/5% for N samples
				8.6 GHz			
0°	0.013	1.2×10^4	1	-12.9 dB/+4.8 dB	20	20	-1.8 dB/+1.4 dB
50°	3.04	49.3	16	-2.1 dB/+1.6 dB	5	80	-0.76 dB/+0.73 dB
70°	13.2	11.4	70	-1.0 dB/+0.9 dB	5	350	-0.35 dB/+0.35 dB
				17.0 GHz			
0°	.003	5.2×10^4	1	-12.9 dB/+4.8 dB	20	20	-1.8 dB/+1.4 dB
50°	1.43	104.9	7	-3.3 dB/+2.3 dB	5	35	-1.3 dB/+1.1 dB
70°	6.2	24.2	33	-1.4 dB/+1.2 dB	5	165	-0.5 dB/+0.47 dB
				35.6 GHz			
0°	.009	1.7×10^4	1	-12.9 dB/+4.8 dB	20	20	-1.8 dB/+1.4 dB
50°	2.53	59.3	13	-2.3 dB/+1.8 dB	5	65	-0.82 dB/+0.79 dB
70°	11.0	13.6	58	-1.0 dB/+0.9 dB	5	290	-0.38 dB/+0.38 dB

$$D = \frac{C\tau}{2} \qquad (40)$$

where c is the velocity of light (3×10^8 m/s). Hence the decorrelation frequency bandwidth is:

$$\Delta f_d = \frac{150}{D} \text{ MHz} = \frac{2 \times 150}{c\;\tau} \times 10^6 \text{ Hz} \qquad (41)$$

and the number of independent samples provided by the IF bandwidth ΔF_{IF} is:

$$N_f = \frac{\Delta F_{IF}}{\Delta f_d} = \frac{1}{\tau} \cdot \frac{c\,\tau}{2 \times 150 \times 10^6} = 1 \qquad (42)$$

If Rayleigh fading is assumed, the 90% confidence limits on a single measurement are between -12.9 dB and +4.8 dB relative to the mean.

If a chirp pulse radar is used with a frequency variation of $10/\tau$ and an IF bandwidth of $10/\tau$, the number of independent samples per look will be 10. Therefore, for a given observation the 90% confidence limits with Rayleigh fading are -2.7 dB to +2.0 dB. A large reduction in fading is obtained without changing pulse width (or range resolution).

4.0 PRELIMINARY RESULTS

The following section presents some of the preliminary analyses of a small portion of the data. It should be noted that the radar backscatter measurements reported herein have not been converted to absolute scattering coefficient values. The conversion involves the incorporation of the range to target, the area of the illuminated cell and the Luneberg lens cross section. This conversion will be completed over the next two months and all future reports will report values of σ°, the scattering coefficient instead of relative backscatter power values.

4.1 Measurement Variability

This section examines the horizontal spatial variability of the test site and the measurement precision of the radar systems.

4.1.1 Test Site Spatial Variability

Ground truth data collection was conducted in a snowpit along the eastern edge of the test plot. A single pit was chosen to minimize the time span required for each complete ground truth set. To test the applicability of the ground truth data obtained in the snowpit to the rest of the field, four tests were made to examine the uniformity of the snow parameters across the field. Table 6 provides a summary of the snow depth variations of the snowpack. The samples were acquired along the perimeter of the field (at the locations indicated in Figure 41) for the first three tests. The last test, which was performed after the last microwave data set was acquired, sampled the field itself at the numbered locations shown in Figure 41.

It is clear from Table 6 that the snowpack was spatially uniform in depth as indicated by the height standard deviation. Before the March 14, 1977 test, high winds had caused the back edge of the test plot to drift and reduce the snow depth in that area. These points were not really in the radar field of view, since at 70° angle of incidence, the maximum ground range of the radar was 90 meters and the outer perimeter of the field was at a range of 110 meters. If the measurements along the back edge of the plot are deleted, then the standard deviation is 1.4 cm.

In addition to measuring the snowpack height, depth profiles were obtained of the snowpack density. The combination of height and density profile was used to calculate the snow water equivalent m (cm). Figure 41 includes plots of m as a function of position around the field for the February 15, 1977 and March 12, 1977 tests and for the interior

57

Figure 41. Spatial variability of snow depth and density at test site.
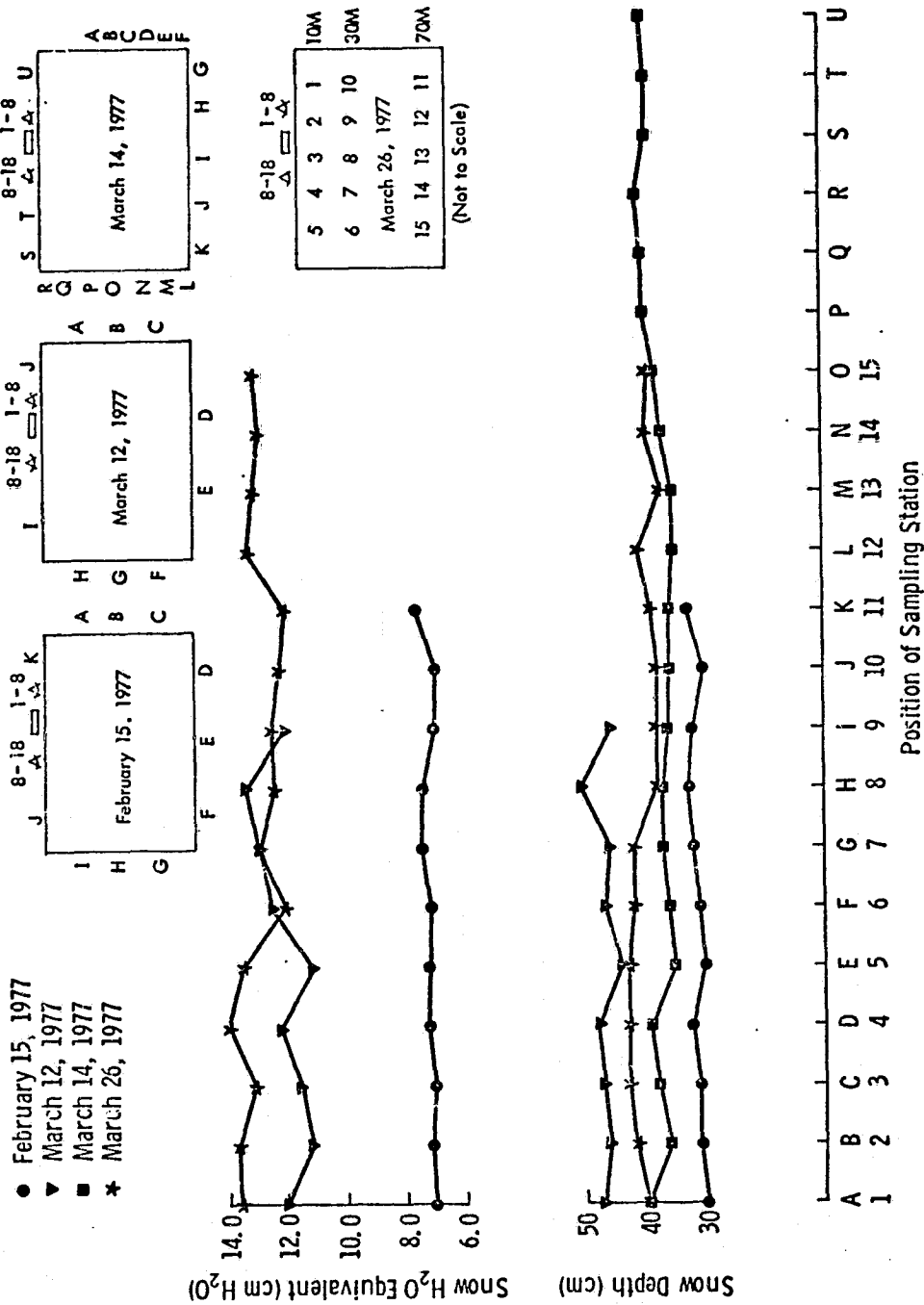
of the field for the March 26, 1977 test. Table 7 is a summary of
the measurements statistics.

TABLE 6. Mean snowpack height and standard deviation
based on N samples acquired along the perimeter
of the test plot as indicated in Figure 41.

Date	N	$\bar{h}$ (cm)	σ_h (cm)
February 15, 1977	11	31.3	1.1
March 12, 1977	9	46.7	1.9
March 14, 1977	21	37.9	1.9
March 14, 1977	12 (excluding far range, points E through N in Fig. 41)	39.2	1.4
March 26, 1977	15	40.3	1.8

TABLE 7 . Mean snowpack water equivalent and standard
deviation.

Date	N	$\bar{m}$ (cm)	σ_m (cm)
February 15, 1977	11	7.3	0.22
March 12, 1977	9	12.1	0.71
March 26, 1977	15	12.9	0.61

4.1.2 Precision of Microwave Measurements

Having established in the previous section that the snowpack was
fairly uniform, both in terms of height and water equivalent, we now
proceed to examine the measurement precision of the microwave sensors.
More specifically, the spatial homogeneity of the snowpack makes it
possible to average data from different spots across the field, thereby
improving the measurement precision of the microwave sensors, partic-
ularly the radar.

Figure 42 shows the 10.69 GHz and 37 GHz radiometric temperatures
for 13 measurements at 13 different spots across the field. The

Date: 3/3 – 3/4/77
Time: 2050 to 2300
Angle of Incidence (Degrees): 50
★ 37 GHz, H-polarization
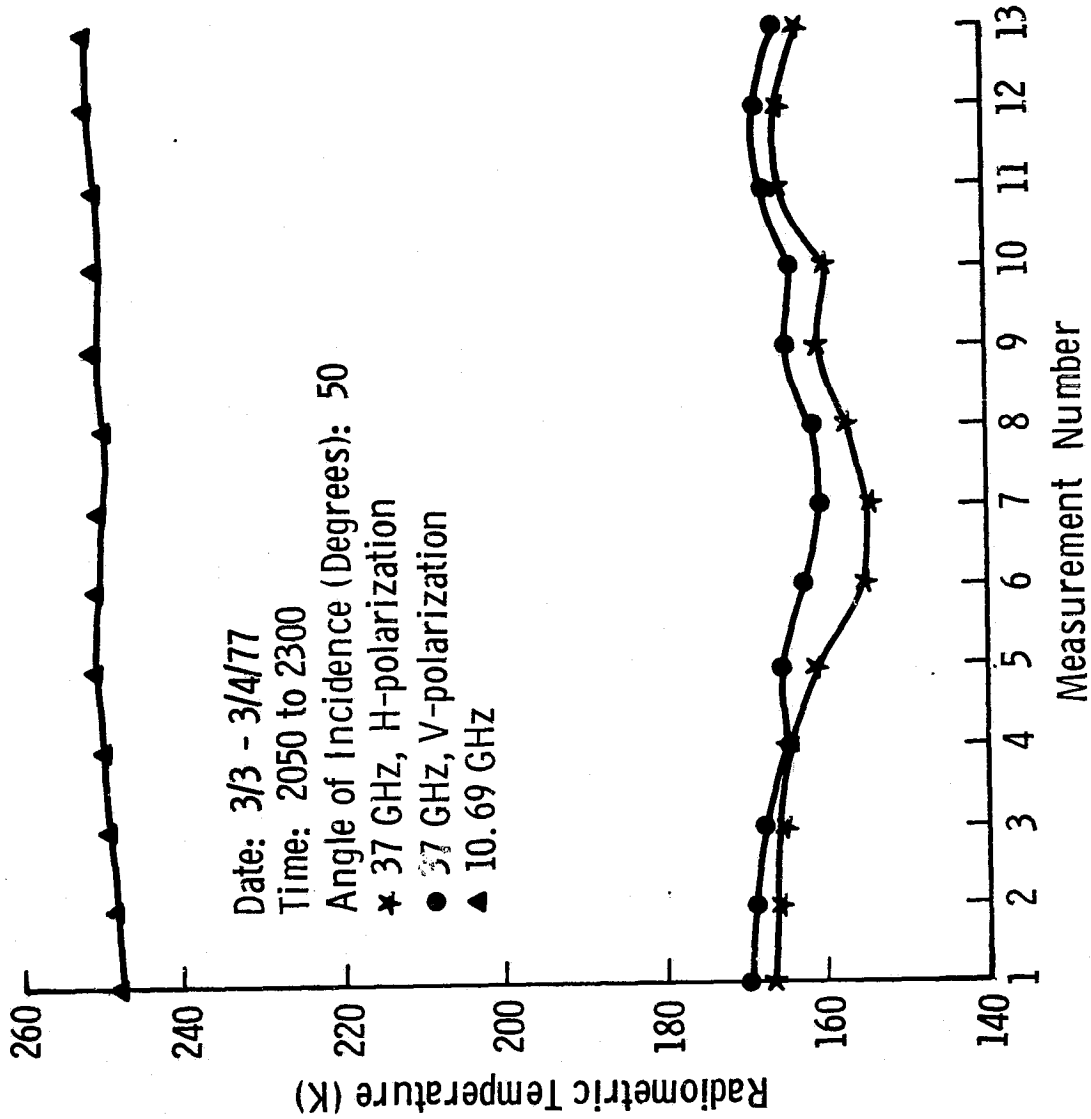● 37 GHz, V-polarization
▲ 10.69 GHz

Figure 42. Spatial variability of microwave radiometric temperatures.

positions of the spots were chosen randomly. The measurements were acquired over a span of approximately two hours during the late hours of the night during which the snowpack conditions remained essentially constant. According to Figure 42, the 10.69 GHz radiometric temperature variation was only 3 K. At 37 GHz, the total variation is 9 K for the vertically polarized channel and 12 K for the horizontally polarized channel. About 5 K of that variation can be explained as a response to variations in the downward emitted sky radiometric temperature. The remainder is probably due to small variations in the snowpack properties over the two-hour measurement period. It may also be argued that the observed variation is totally due to drifts in the amplifier gain of the radiometer receiver. In either case, the variation is small in comparison to the change (about 80 K) observed during the diurnal cycles (section 4.2) which appears to be in response to variations in snow wetness.

Variability of the radar data is shown in Figure 43 for 17.0 GHz and 35.6 GHz at nadir and 50°. Table 8 provides a list of the measured values of the received power and the mean value and the variance of the received power. Also provided in Table 8 are the number of independent samples calculated on the basis of the measured data (Eq. 36 and on the basis of Rayleigh fading and frequency averaging (Eqs. 37 and 38). Two values of the predicted number of independent samples are given in Table 8 , the smaller value corresponds to the assumption that the backscatter is only from the snowpack surface while the larger value corresponds to the assumption that the entire snowpack depth contributes to the backscatter. Comparison of the calculated and predicted values of N clearly demonstrates that Rayleigh fading is a good descriptor of the fading statistics of snowpacks.

The variations shown in Figure 43 are in agreement with the predictions of section 3.3 and Table 5. At 5° angle of incidence the variations are much larger than the variation at 50° for both frequencies. This is precisely the reason for acquiring more spatially independent samples at nadir than at the higher angles.

TABLE 8. Scatterometer measurement variation with spatial position.

| Date: 2/18/77 Time: 0300	Angle of Incidence (degrees): 5		Date: 3/3/77 Time: 2045	Angle of Incidence (degrees): 50	
Measurement Number	Measured Received Power (dB)		Measurement Number	Measured Received Power (dB)	
	17.0 GHz	35.6 GHz		17.0 GHz	35.6 GHz
1	-38.9	- 8.3	1	-40.1	- 5.6
2	-40.3	- 2.7	2	-43.2	- 6.5
3	-36.1	- 6.9	3	-42.8	- 5.7
4	-41.6	- 7.3	4	-44.1	- 7.7
5	-39.2	- 3.5	5	-44.3	- 7.3
6	-44.0	- 4.6	6	-42.8	- 6.2
7	-44.0	- 2.4	7	-43.0	- 7.8
8	-42.7	- 2.9	8	-39.4	- 6.5
9	-39.9	- 9.0	9	-43.1	- 6.8
10	-42.4	- 7.4	10	-42.5	- 6.6
11	-37.4	- 6.8	11	-41.8	- 8.0
12	-37.2	- 5.8	12	-42.7	- 6.6
13	-48.9	- 9.2	13	-42.8	- 8.7
14	-47.8	-10.8	14	-45.1	- 6.0
15	-38.2	- 7.1	15	-43.3	- 5.8
16	-42.1	- 9.8			
17	-43.5	- 3.5			
18	-45.3	-10.9			
19	-45.2	- 7.9			
20	-38.7	- 3.3			
$\mu \frac{}{W}$	9.02×10^{-5}	.270	$\mu \frac{}{W}$	5.64×10^{-5}	.214
$\sigma \frac{2}{W}$	4.02×10^{-9}	.0264	$\sigma \frac{2}{W}$	4.569×10^{-10}	.00173
$N_{calc} = \frac{\mu^2}{\sigma^2}$	2.0	2.8	$N_{calc} = \frac{\mu^2}{\sigma^2}$	7.0	26.5
N_{pred} (no penetration)	1	1	N_{pred} (no penetration)	7	13
N_{pred} (complete penetration 35 cm)	1.9	1.9	N_{pred} (complete penetration 35 cm)	10.8	16.5
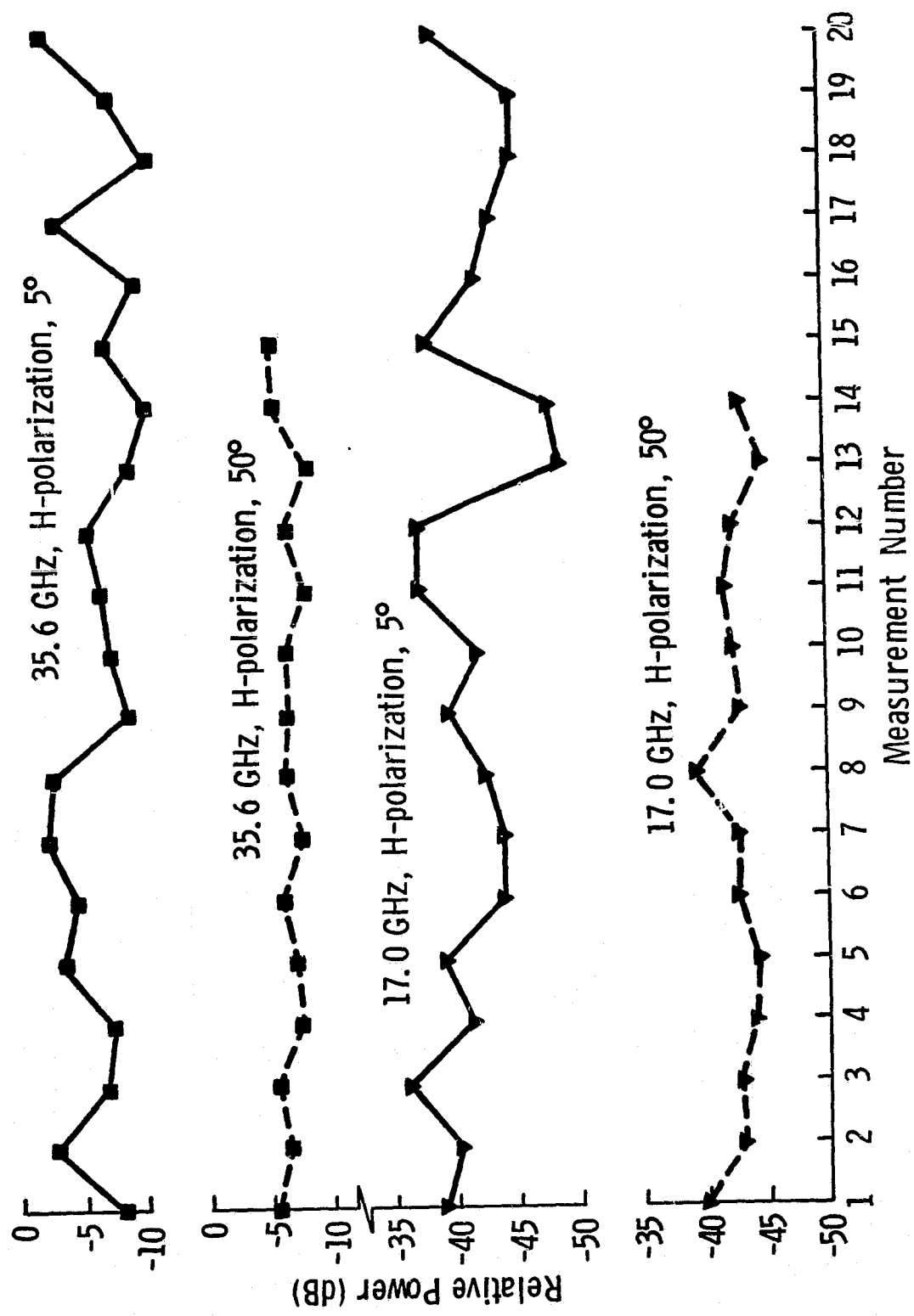
Figure 43. Spatial variability of received backscatter power at two frequencies and angles.

63

4.2 Diurnal Experiment

To investigate the effects of diurnal changes in snowpack conditions, data were acquired over four diurnal periods. During the first diurnal experiment on February 17-18, 28 MAS 8-18/35 and radiometer data sets were taken at 55° angle of incidence and 14 MAS 8-18/35 and radiometer data sets were taken at 5° and 25°. Ground truth was obtained approximately once per hour. The calorimeter measured 13 surface samples over the 28 hour period. Seven surface samples were checked for wetness with the capacitor method. Also samples were measured for wetness at deeper layers. On February 17 the sky was generally a light overcast and the winds were calm.

The temperature of the snow was measured as a function of depth in the snow, and also at the ground level. Figure 44 shows the variation in temperature of the air, snow at 26 cm above the ground and the ground level. During the diurnal period the snow depth was approximately 30 cm, so the 26 cm measurement was the closest to the snow surface. As expected, the air temperature exhibited the greatest variation over the 28 hour period. The peak temperature at 1030 hours corresponded to a light cloud cover. The clouds were variable during the day resulting in the non-uniformity in the temperature curve. The snow temperature rose to 0°C by 1030 hours and remained around 0°C until about 2200 by which time the air temperature had dropped sufficiently to cause cooling of the snow. During the period at 0°C, varying amounts of free water were present in the snow and were measured by the calorimeter and capacitance methods. The ground temperature was observed to vary less than the snow temperature because it was insulated by 30 cm of snow. The ground was in a frozen state during the 28 hour period.

Figure 45 presents the free water content of the surface layer and one underlying layer as measured by the calorimeter. The reason for the dip in free water around 1100 hours is not known since it appears to lead the corresponding temperature drop. The peak value of the free water content, 8.3%, occurred in late afternoon just preceding the temperature drop to below 0°C. The free water of the 15-20 cm layer above ground level indicates a similar trend to the snow surface measurements
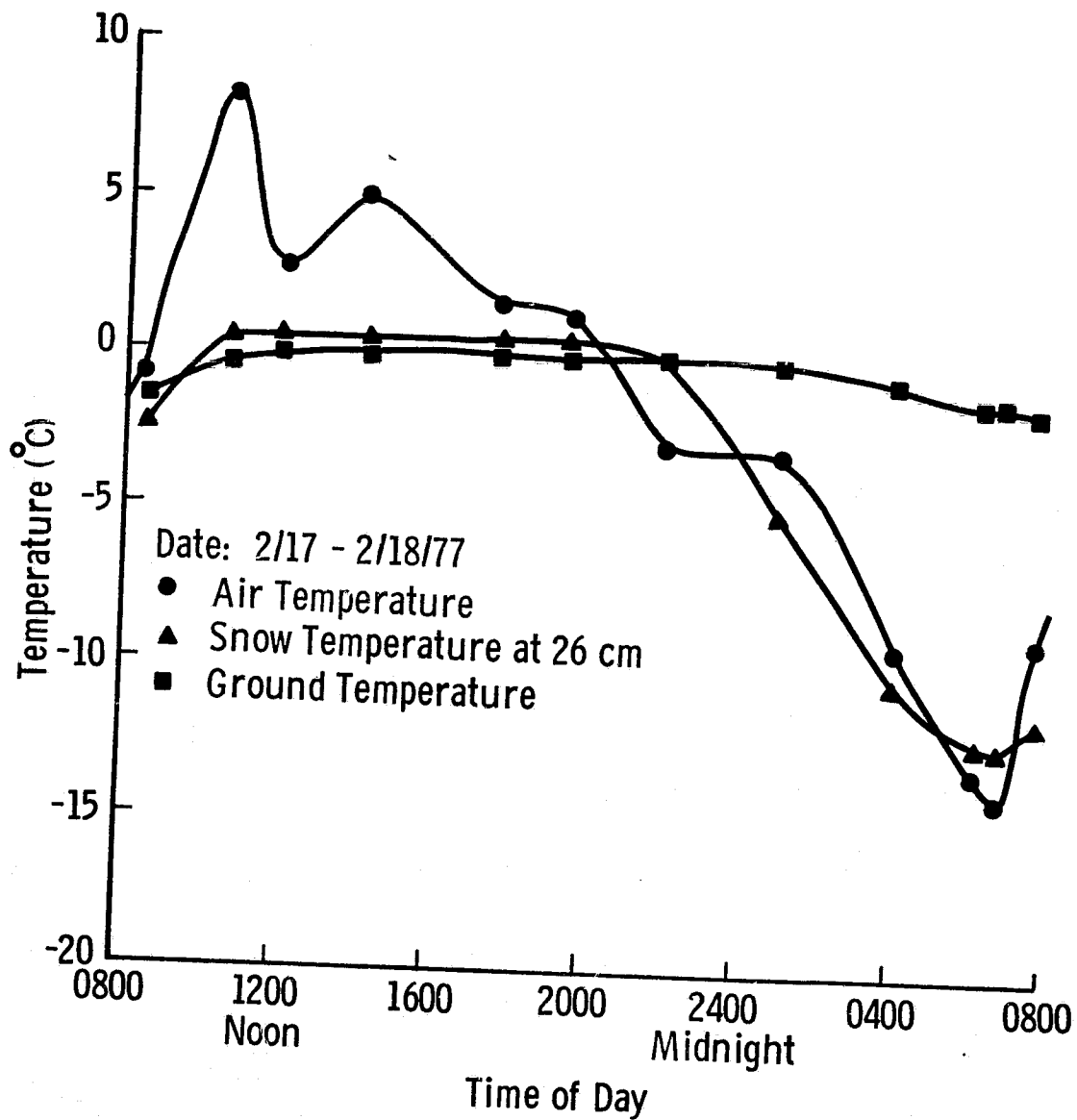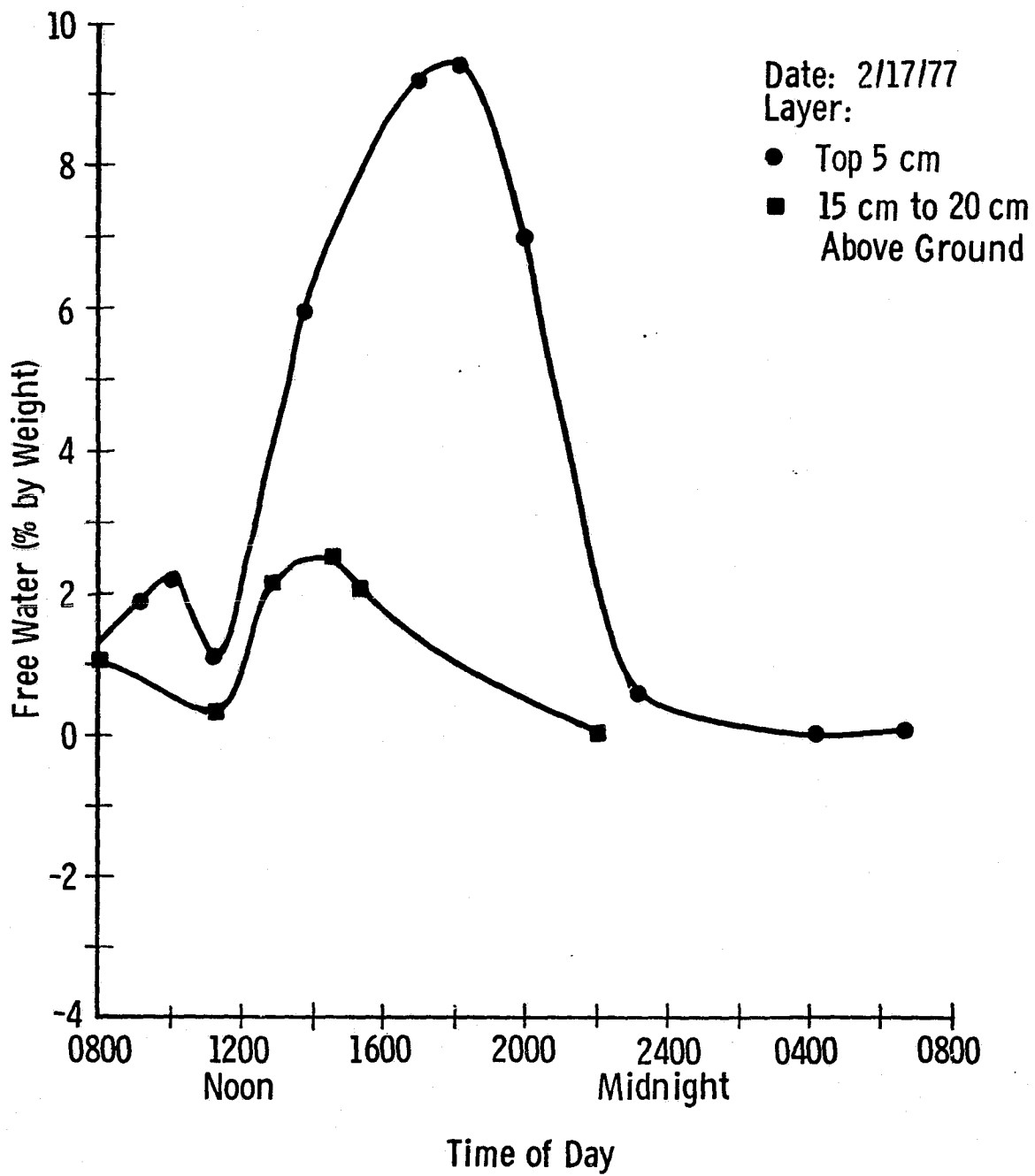
64

Figure 44. Diurnal temperature variation.

Figure 45. Diurnal variation of free water content as measured with the freezing calorimeter.

with a smaller magnitude. The snow was dry between 2300 hours, 17 February and 0800 hours, 18 February.

Capacitance measurements were obtained at three depth layers throughout the diurnal period. Figures 46 to 48 show the change in capacitance at several frequencies. The lower frequencies are much more sensitive to wetness; however, when the snow is very wet they tend to have Q's lower than can be measured by the Q-meter. Some measurements are missing due to operator errors. Examination of the curves, for the ranges of wetness observed during the diurnal, indicates that 500 KHz provides the best compromise between sensitivity and Q. Data from the daily experiments indicate that the frequency choice should be around 1 MHz for higher values of wetness. Figure 49 shows the variation in Q over the diurnal period. The minimum measurable Q was 5. Therefore, 500 KHz or 1 MHz would be the best choice for frequency. The changes in capacitance are very similar to the changes in free water as measured with the calorimeter. The deeper layers show progressively smaller values of wetness.

The diurnal radar data at 8.6, 17.0 and 35.6 GHz are plotted in Figures 50 through 52. The 5° data show no obvious response to a single ground truth parameter whereas the 25° and 55° data indicate an inverse response to free water content (Figures 45 and 46). Over the period when the ground data was relatively constant, 0200 to around 0800 hours, there is less than 2 dB variation in power return. The response to free water content appears to be stronger the higher the frequency. At 25°, the dynamic range at 8.6 GHz is about 6 dB while it is 8.5 dB at 17.0 GHz and almost 12 dB at 35.6 GHz. Figure 45 indicates that the greatest rate of change in the amount of free water was from 1100 hours to about 1400 hours which matches well with the decrease in backscatter power. The 55° backscatter power data show a slight increase in dynamic range over the 25° data: 7 dB at 8.6 GHz, 9 dB at 17.0 GHz and 14 dB at 35.6 GHz. Figure 53 gives the angular responses for a wet and a dry data set. The slopes of the responses are all greater for the wet case than for the dry case. Also the change in slope between the wet and dry cases increases with frequency.
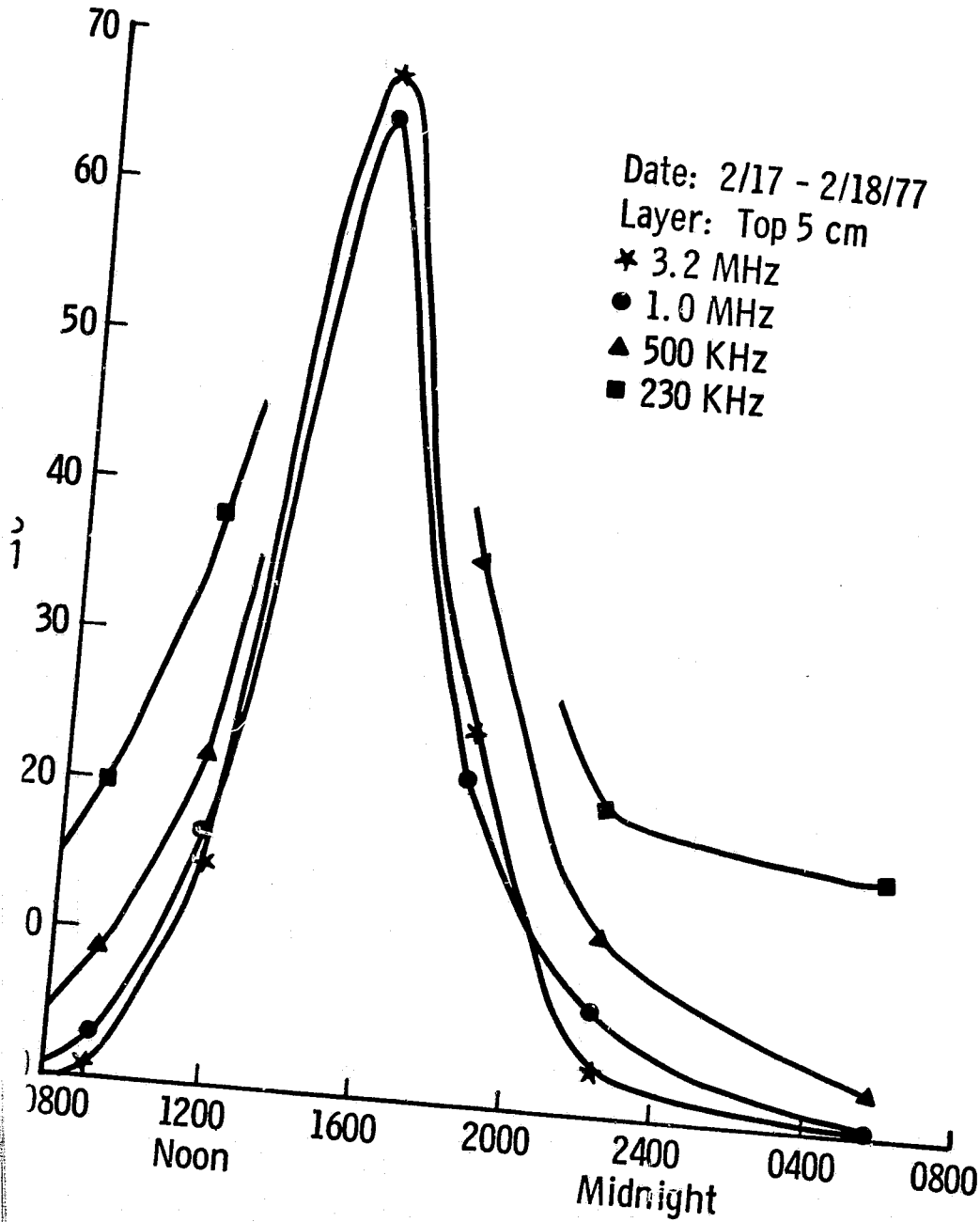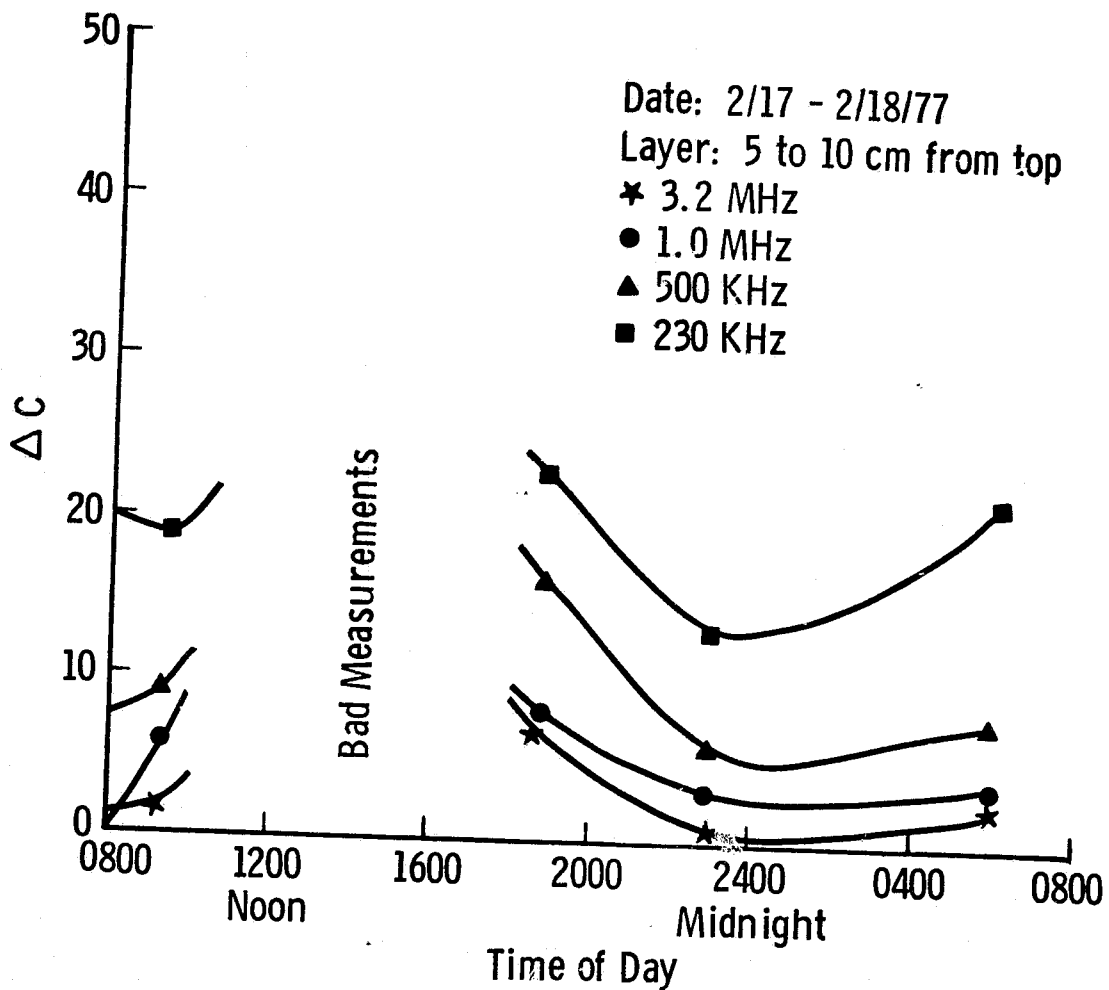
Figure 46. Diurnal variation of ΔC of the top 5 cm layer as measured with the Q-meter.

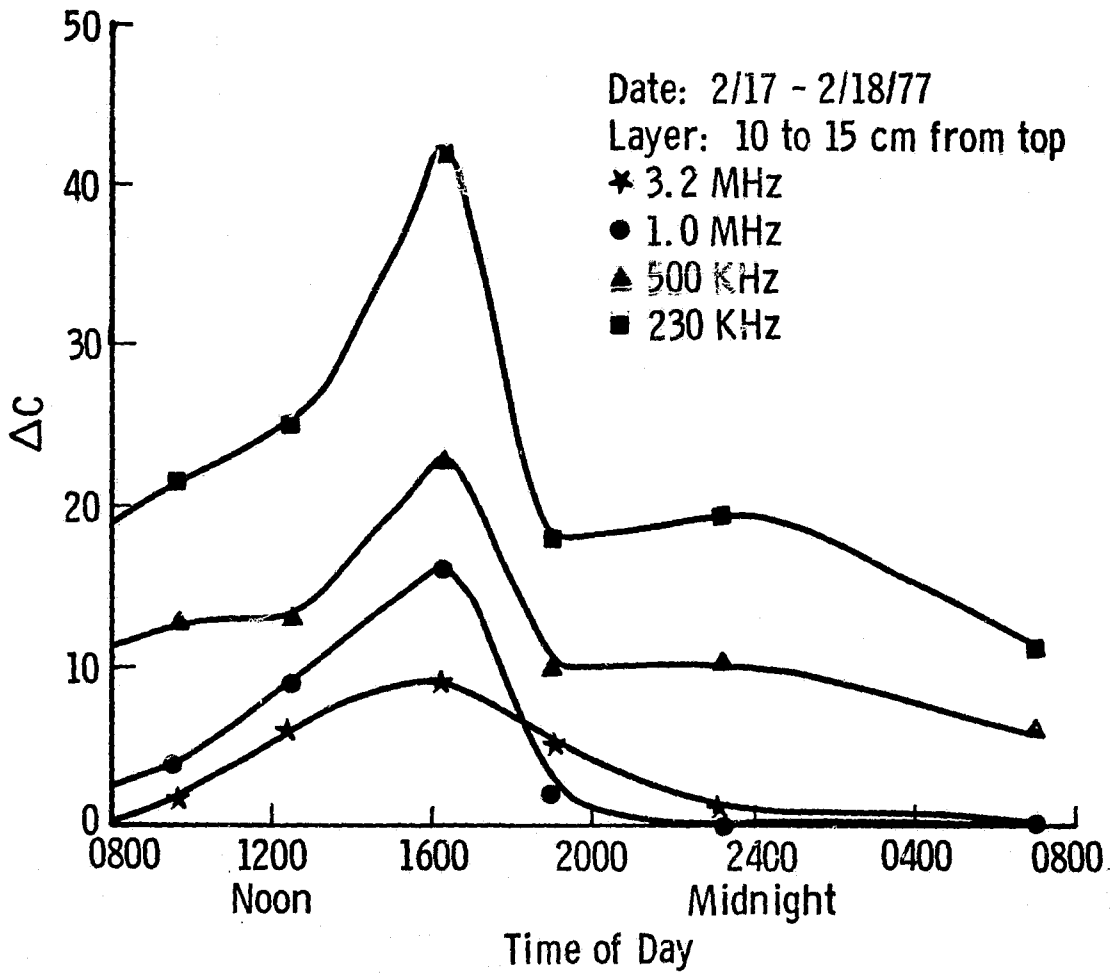Figure 47. Diurnal variation of ΔC of the 5 to 10 cm layer from the top as measured with the Q-meter.

Figure 48. Diurnal variation of ΔC of the 10 to 15 cm layer from the
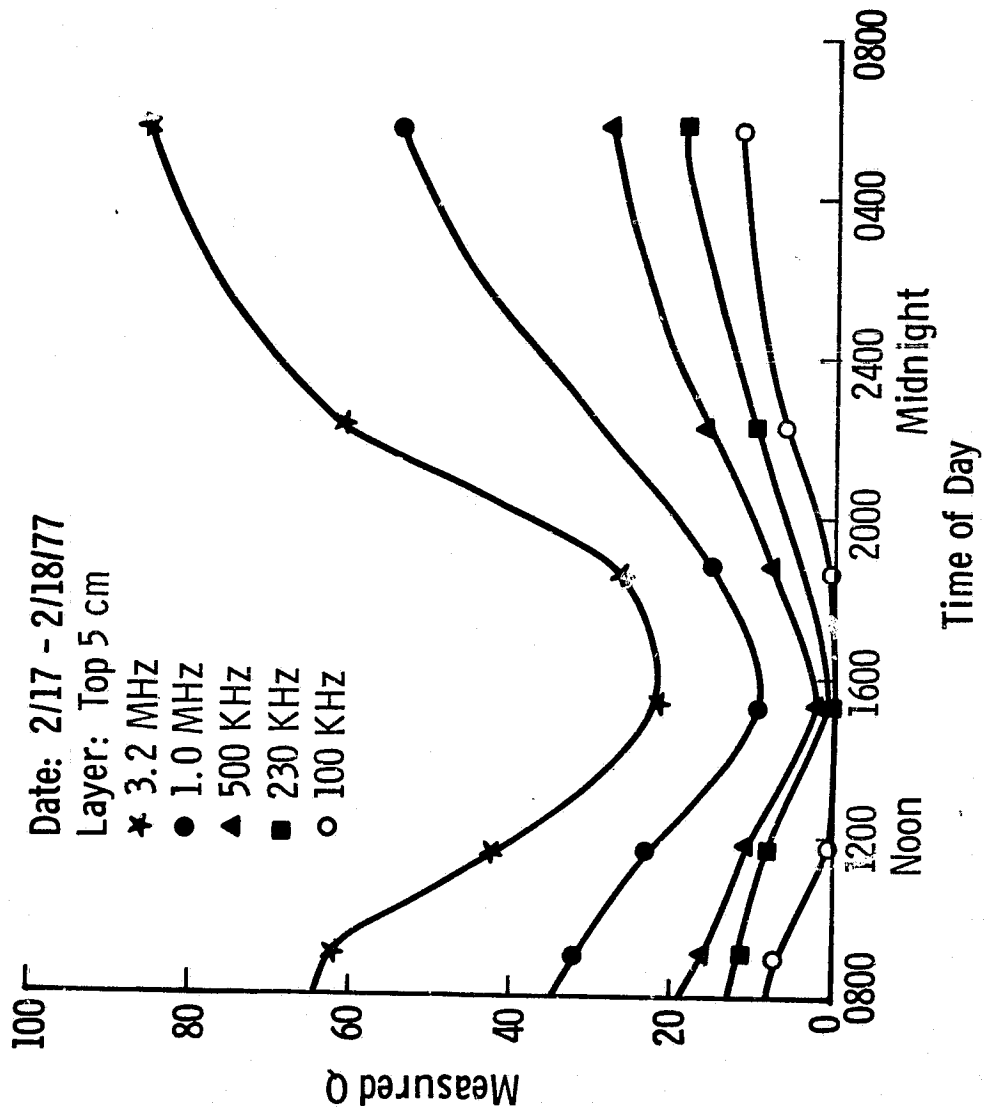top as measured with the Q-meter.

Figure 49. Diurnal variation of Q of the top 5 cm layer as measured with the Q-meter.

Date: 2/17 - 2/18/77
Layer: Top 5 cm
★ 3.2 MHz
● 1.0 MHz
▲ 500 KHz
■ 230 KHz
○ 100 KHz
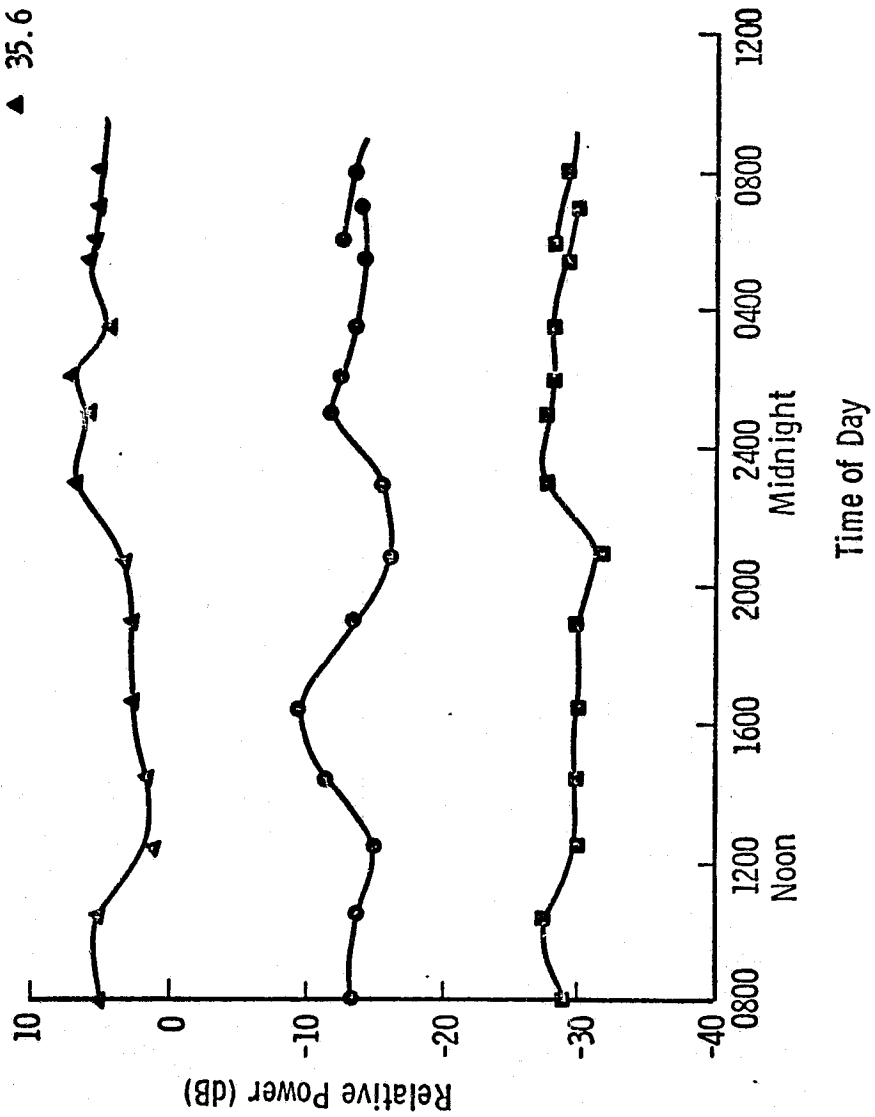
Figure 50. Diurnal variation of the received power measured by the radar at 5° angle of incidence.

72
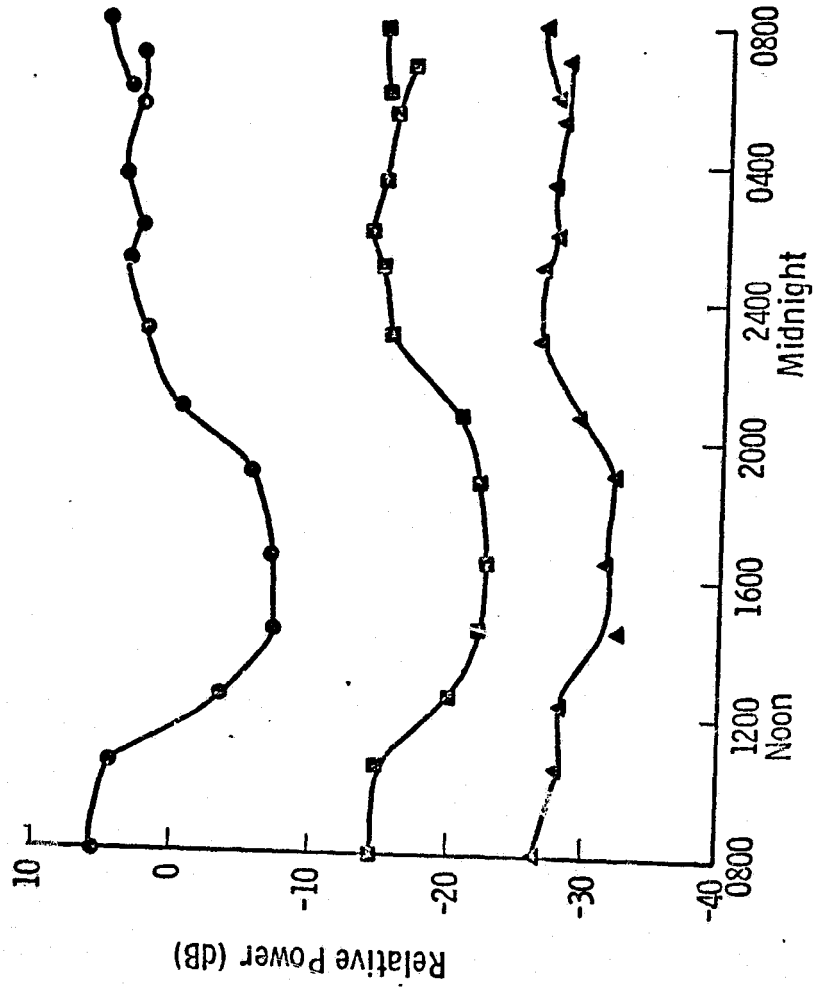
Figure 51. Diurnal variation of the received power measured by the radar at 25° angle of incidence.
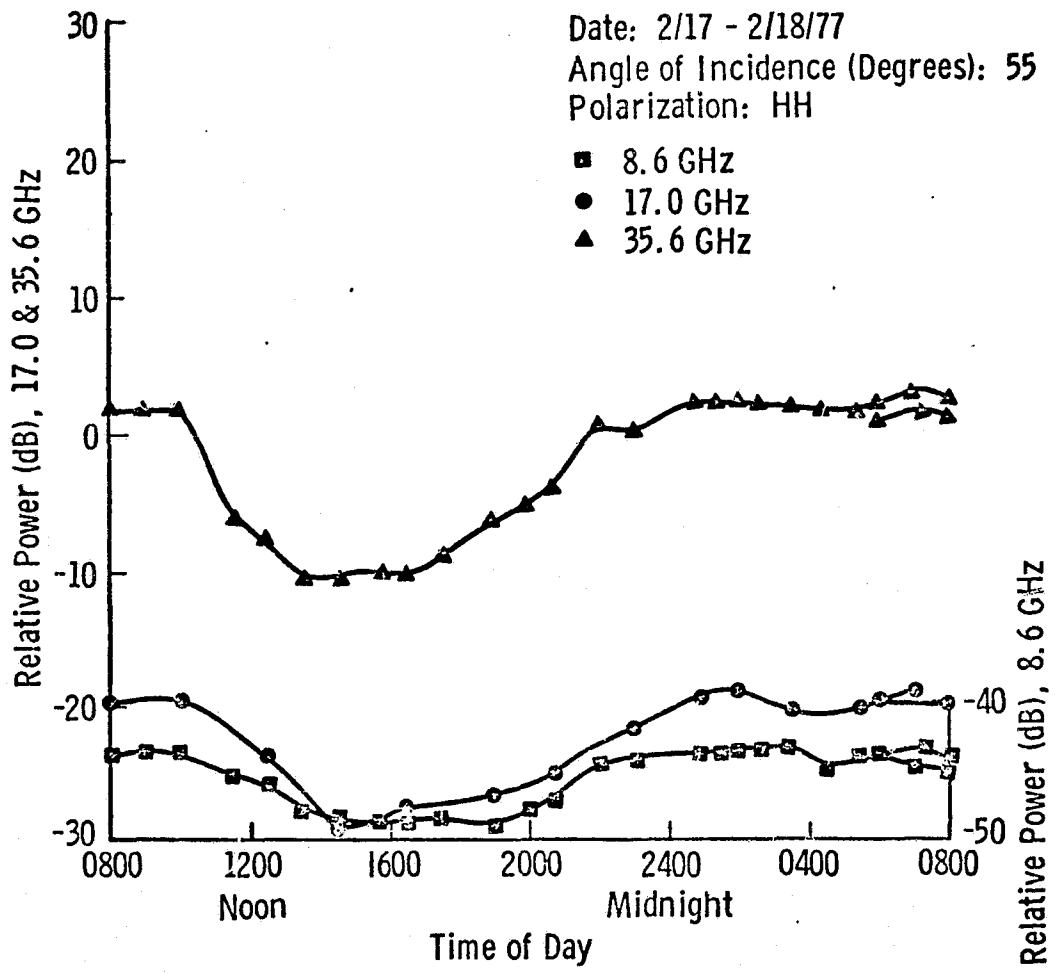
Figure 52., Diurnal variation of the received power measured by the radar at 55° angle of incidence.
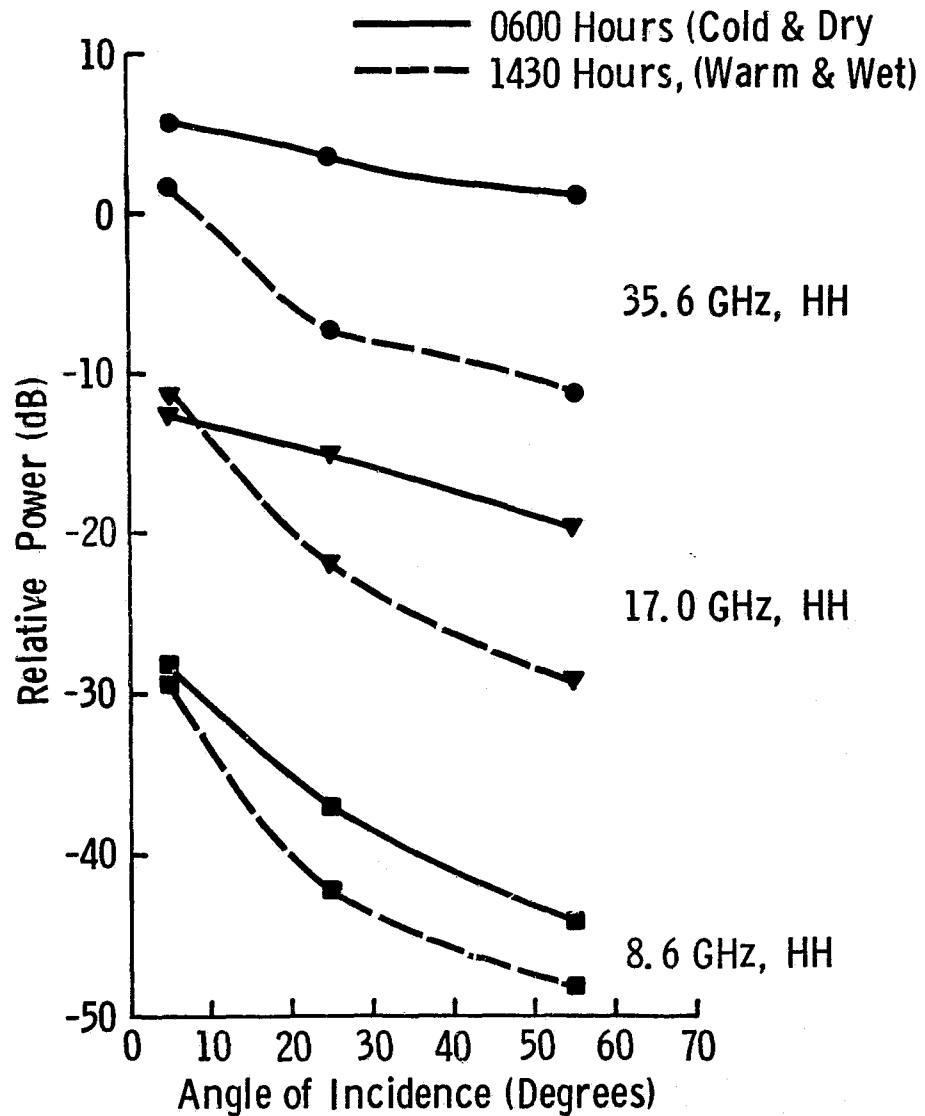
Figure 53. Angular response of the radar backscatter power
for a wet and a dry case.

Radiometric data were acquired at 10.69 GHz and 37 GHz in addition to the radar data. Figure 54 shows the diurnal response at 10.69 GHz. The mid-day notch is surprising since there were no obvious ground truth changes; this effect may be due to penetration and therefore caused by layering effects. The 37 GHz responses at 5° and 55° from nadir are shown in Figures 55 and 56 . Note the 80 K rise in temperature with the appearance of the free water. Edgerton et al. [5] observed the same effect at 13 and 37 GHz but not at 1.5 and 5 GHz for a 40 cm water equivalent snowpack. Figure 57 shows the radiometric angular response for a wet and a dry snow case. When the snow is wet, the drop in temperature with angle is less.

During the second diurnal experiment on March 3 and 4, sixteen MAS 1-8, twelve MAS 8-18/35 and twelve 10.68 GHz and 37 GHz radiometer data sets were obtained over a 26 hour period. Ground truth data were also recorded. These data included eight calorimeter surface samples and seven capacitor measurements. The sky was very lightly overcast and light snow was falling. The temperatures are shown in Figure 58 . The snow temperature was near 0°C for only a short time during the day. The calorimetric and capacitance measurements again agree qualitatively (Figures 59 and 60) and show the peak value of the free water to be between 1400 and about 1700 hours. Figures 61 through 63 present the relative radar response at nadir, 20° and 50°. Similarly to the first diurnal experiment, no simple response is apparent for the 0° data. At 20° and 50° angles of incidence, the response to free water is quite strong, especially at the higher frequencies: 35.6 GHz and 17.0 GHz. Figure 64 shows the variation of the 10.69 GHz radiometric temperature over the diurnal period. The radiometric temperature response is approximately a mirror image of the cross section curve exhibited by the radar. Figure 65 presents the 37 GHz vertical channel data at 50°. The response in this case also agrees with the 10.69 GHz and radar data although the change between 1100 hours and 1600 hours is much more pronounced than that of the 10.69 GHz.

In conclusion, the following preliminary observations are deduced from the first two diurnal experiments:

Date: 2/17 - 2/18/77
Angle of Incidence (Degrees):
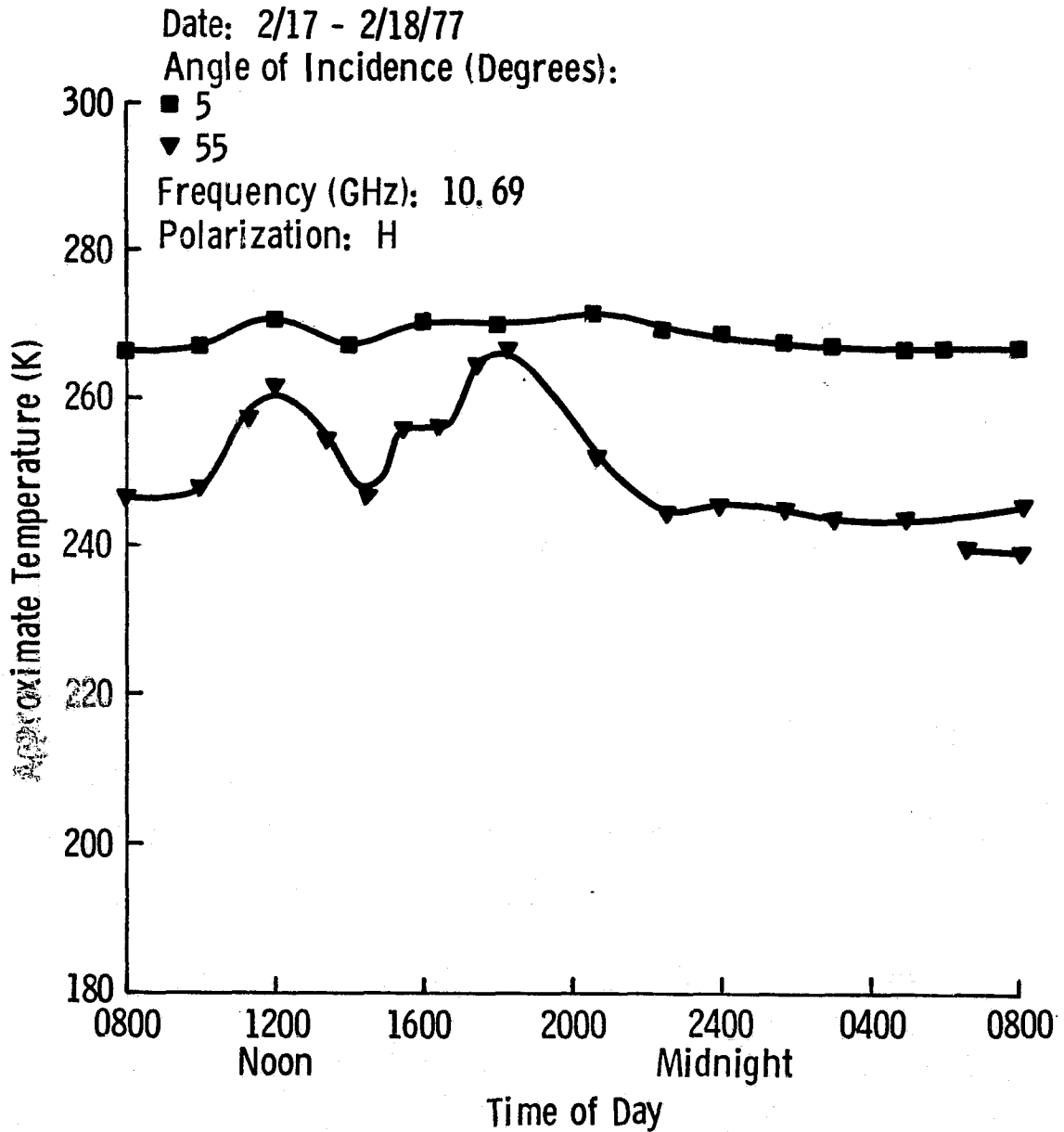■ 5
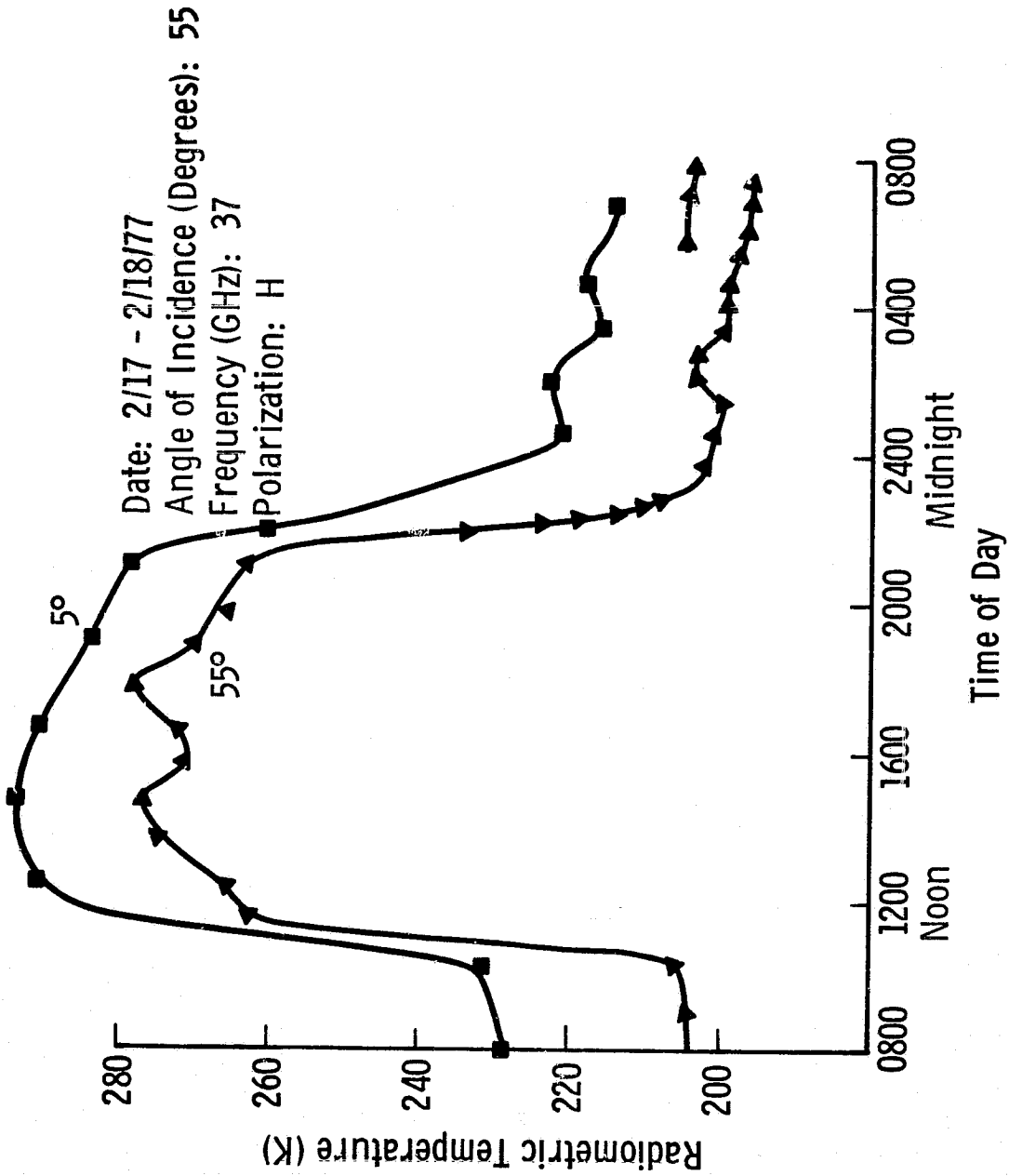▼ 55
Frequency (GHz): 10.69
Polarization: H

Figure 54. Diurnal variation of the radiometric temperature at 10.69 GHz, horizontal polarization.

77

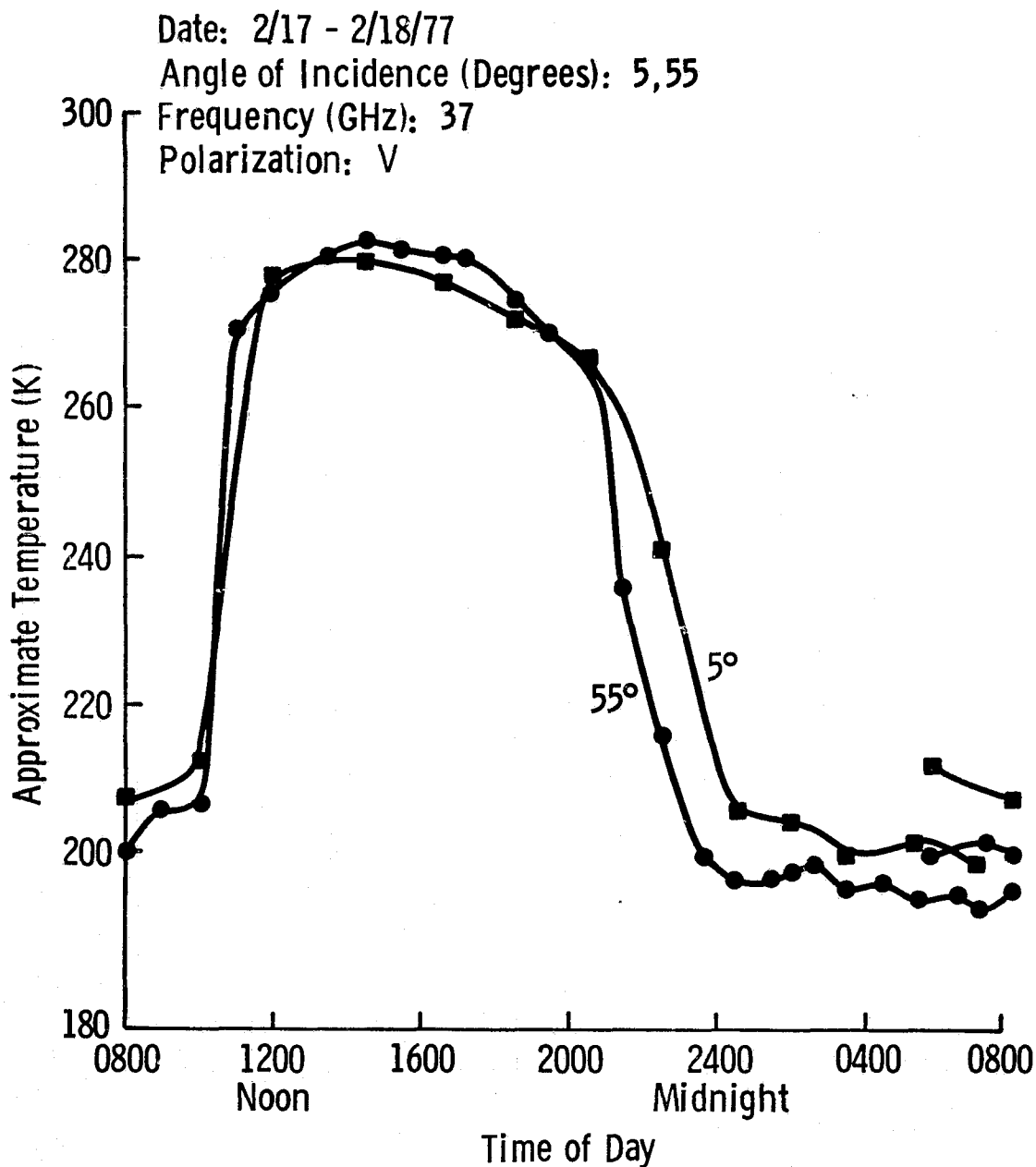Figure 55. Diurnal variation of the radiometric temperature at 37 GHz, horizontal polarization.

Date: 2/17 – 2/18/77
Angle of Incidence (Degrees): 55
Frequency (GHz): 37
Polarization: H

Figure 56. Diurnal variation of the radiometric temperature at 37 GHz, vertical polarization.

Date: 2/17 - 2/18/77
Time:

——————— 0600 Hours (Cold & Dry)
— — — 1430 Hours (Warm & Wet)
● 37 GHz, H-polarization
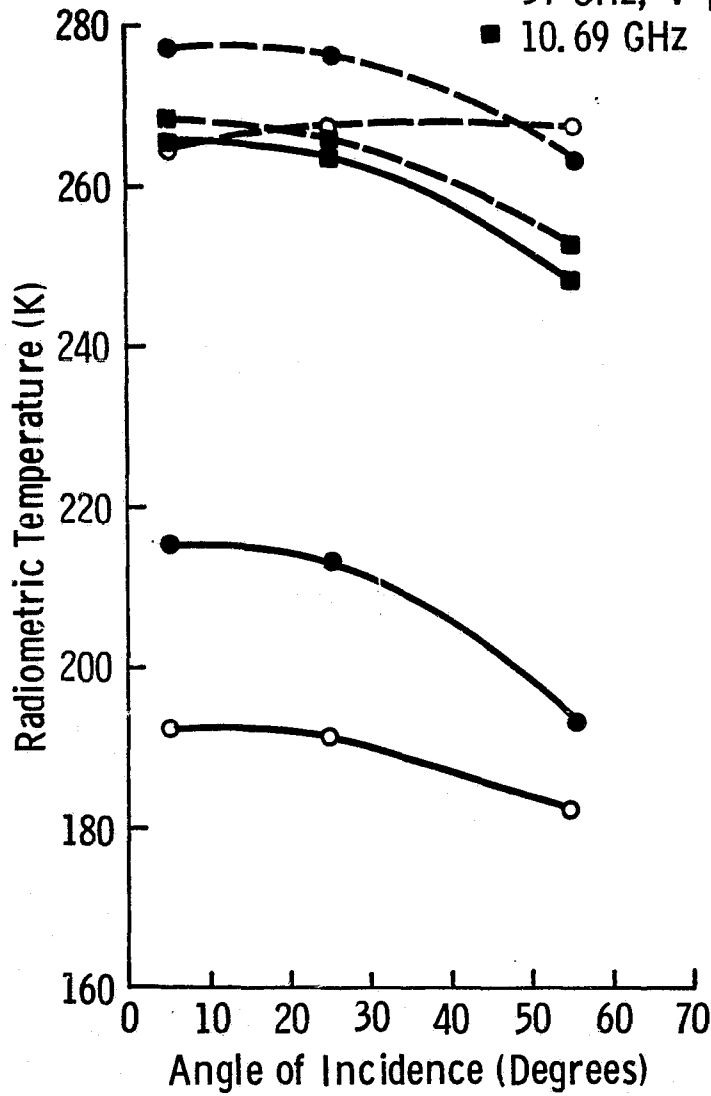○ 37 GHz, V-polarization
■ 10. 69 GHz

Figure 57. Angular response of radiometric temperatures at 10.69 GHz and 37 GHz for a dry and a wet case.

80
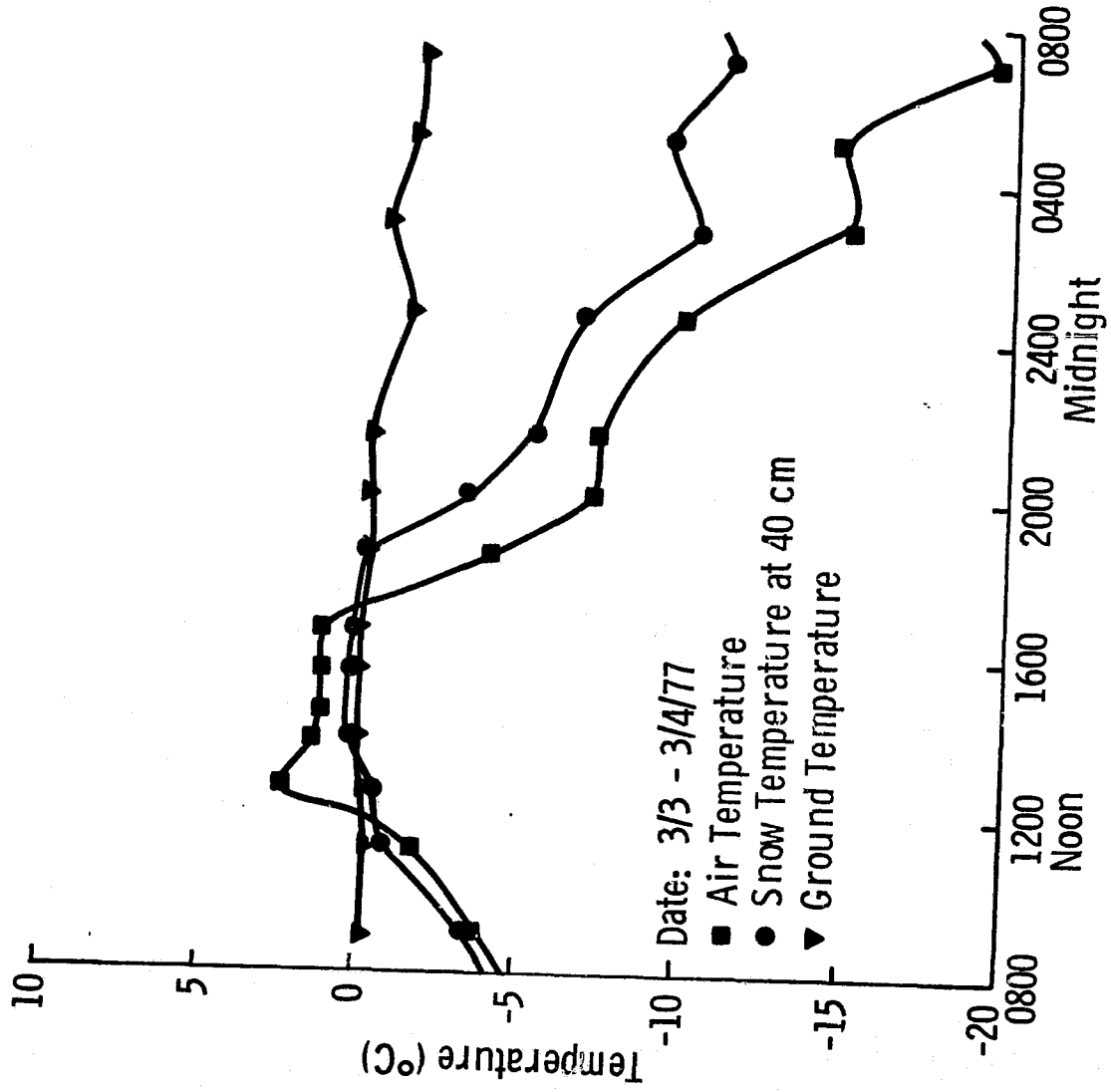
Figure 58. Diurnal temperature variation.
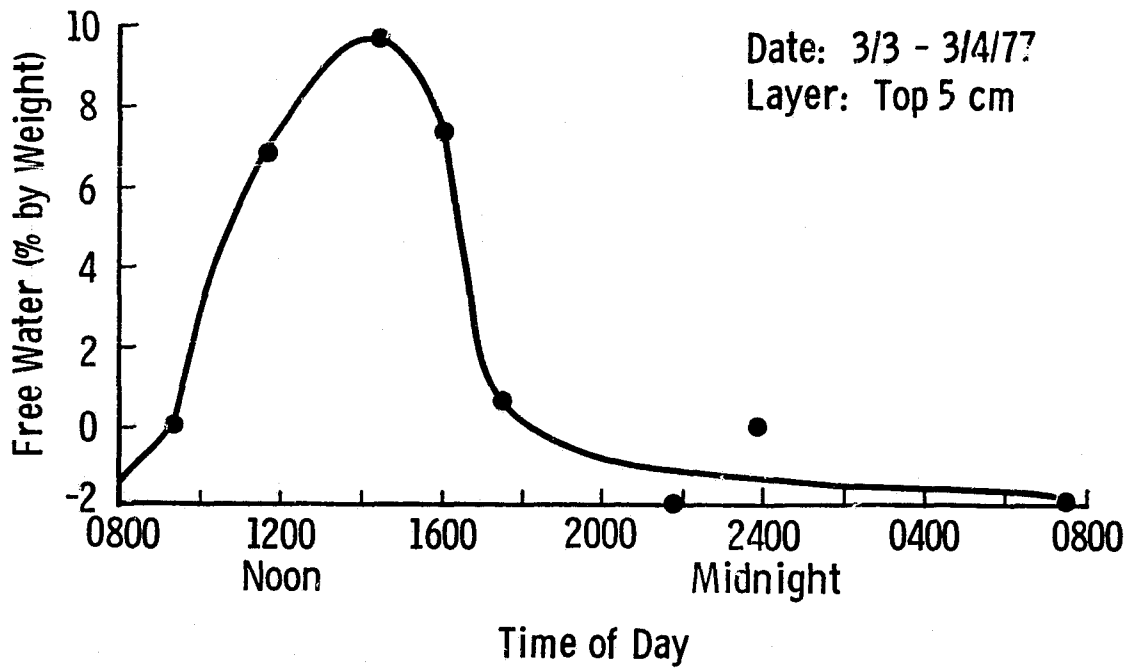
Figure 59. Diurnal variation of free water content as measured with the freezing calorimeter.
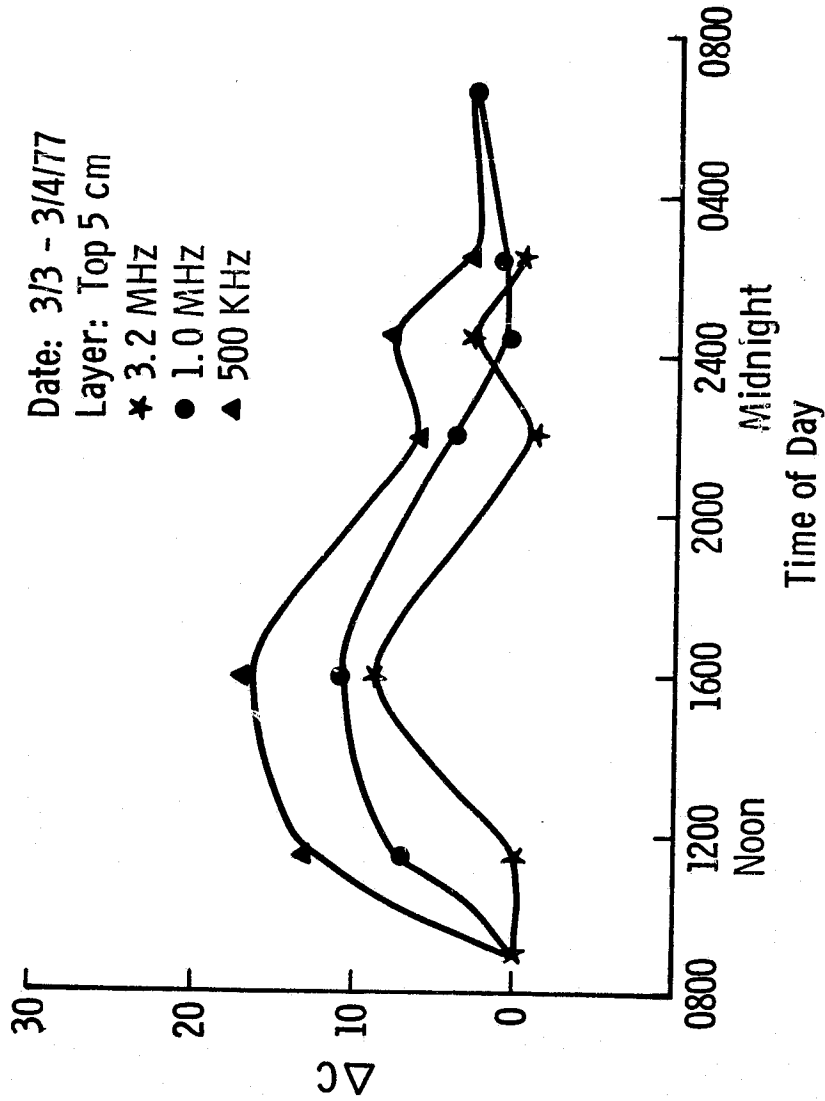
Figure 60. Diurnal variation of ΔC of the top 5 cm layer as measured with the Q-meter.

83
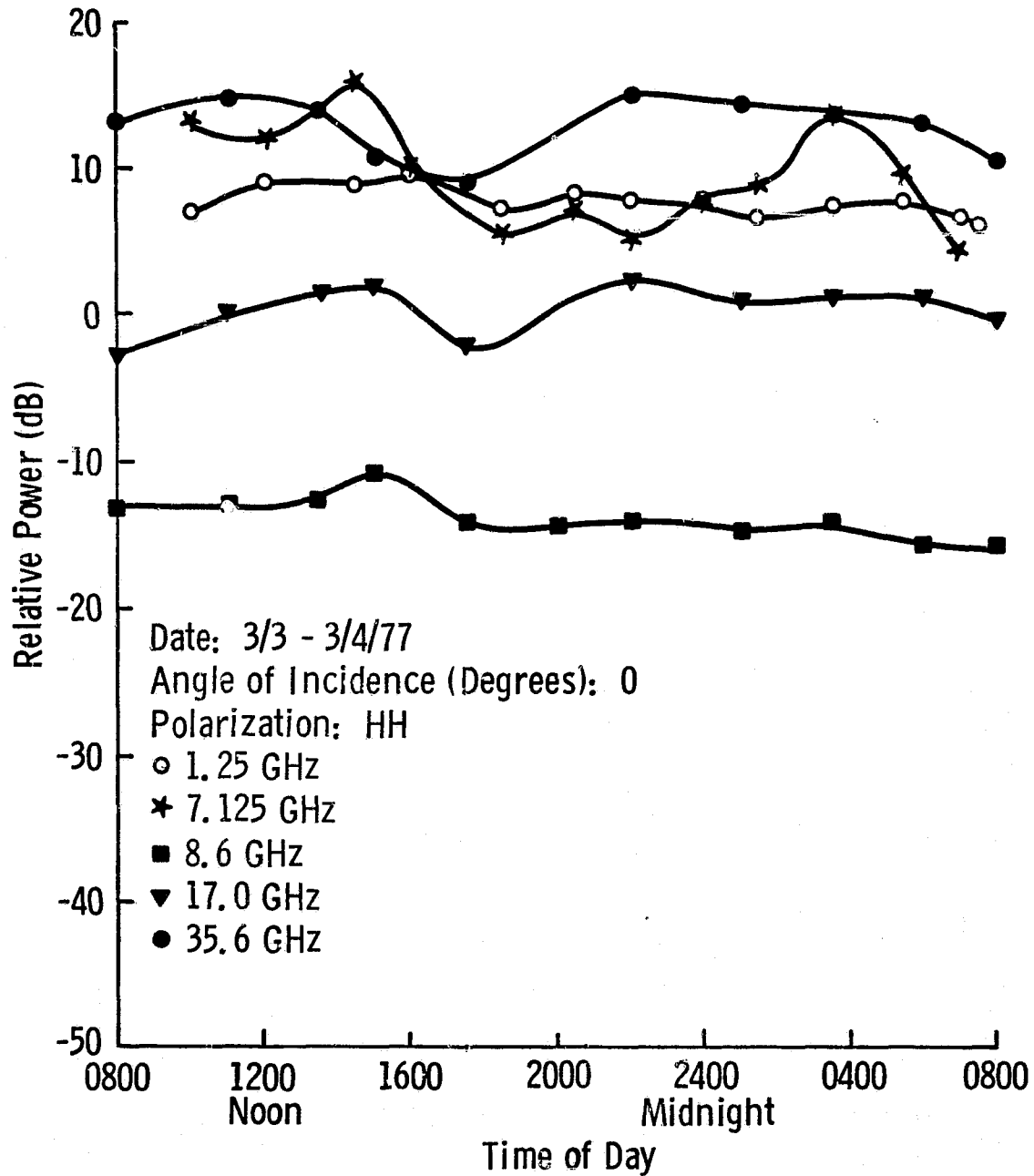
Figure 61. Diurnal variation of the received power measured by the radar at $0°$ angle of incidence.

84

Date: 3/3 - 3/4/77
Angle of Incidence (Degrees): 20
Polarization: HH
○ 1.25 GHz
✶ 7.625 GHz
■ 8.6 GHz
▼ 17.0 GHz
● 35.6 GHz
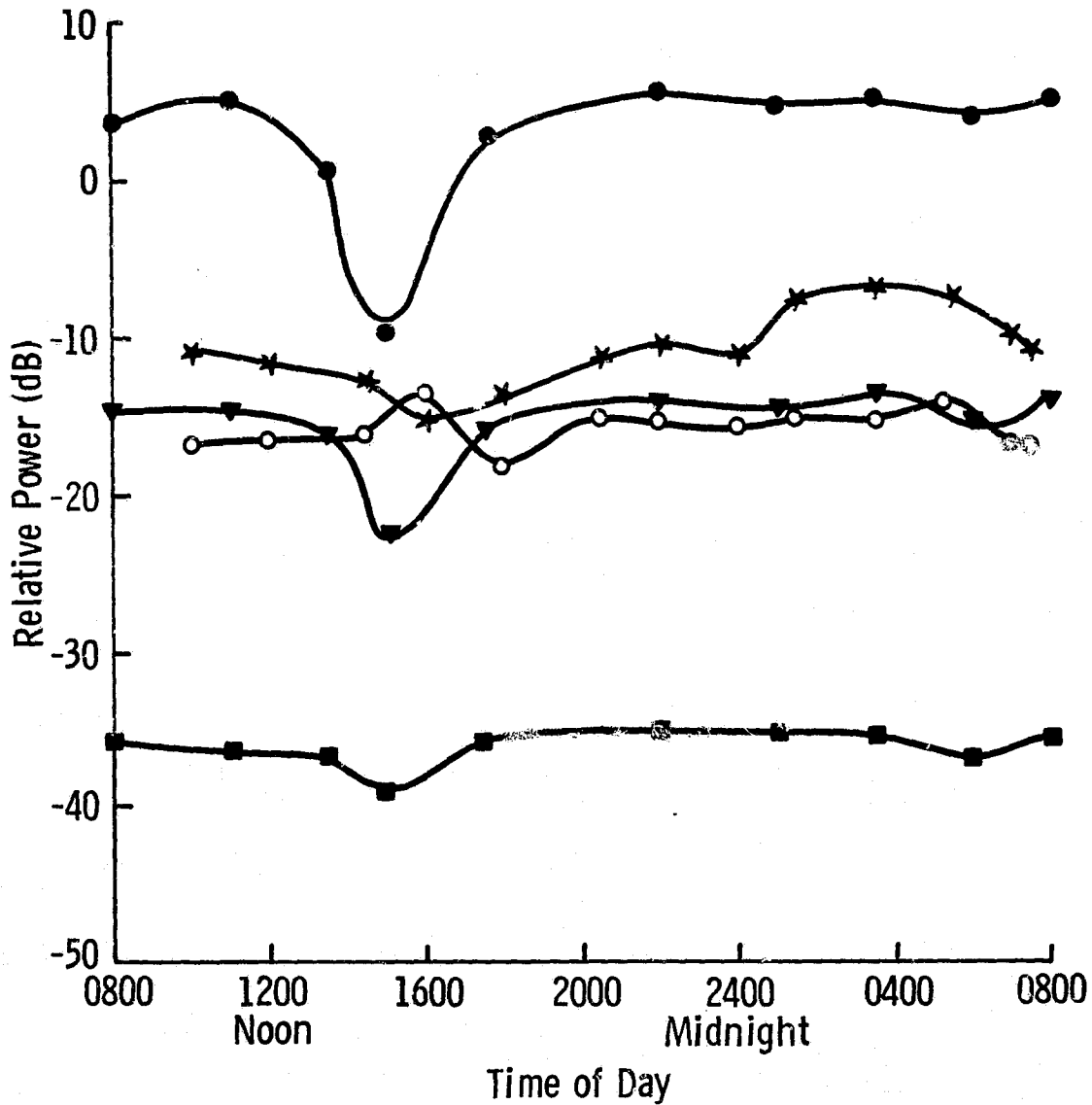
Figure 62. Diurnal variation of the received power measured by the radar at 20° angle of incidence.

Date: 3/3 - 3/4/77
Angle of Incidence (Degrees): 50
Polarization: HH

■ 1.25 GHz
✶ 7.625 GHz
● 8.6 GHz
▼ 17.0 GHz
⬤ 35.6 GHz

Figure 63. Diurnal variation of the received power measured by the radar at 50° angle of incidence.

C - 2

Figure 64. Diurnal variation of the radiometric temperature at 10.69 GHz, horizontal polarization.
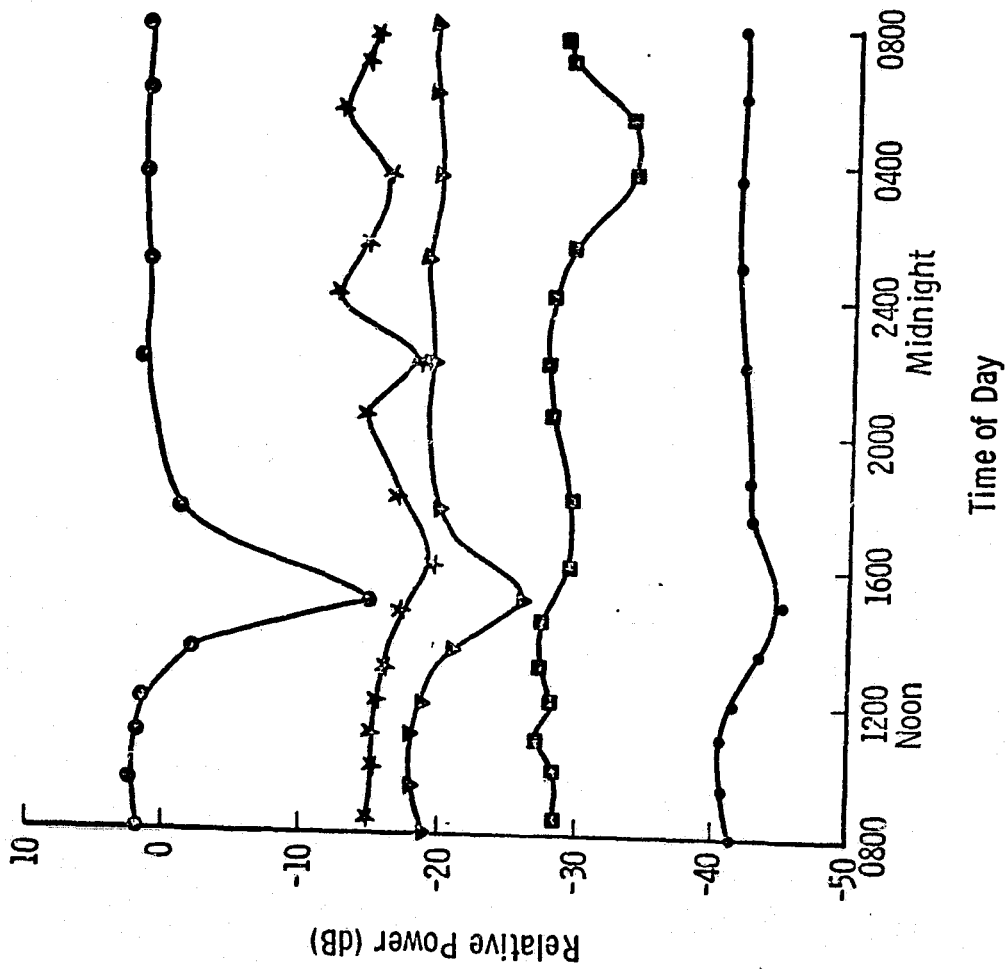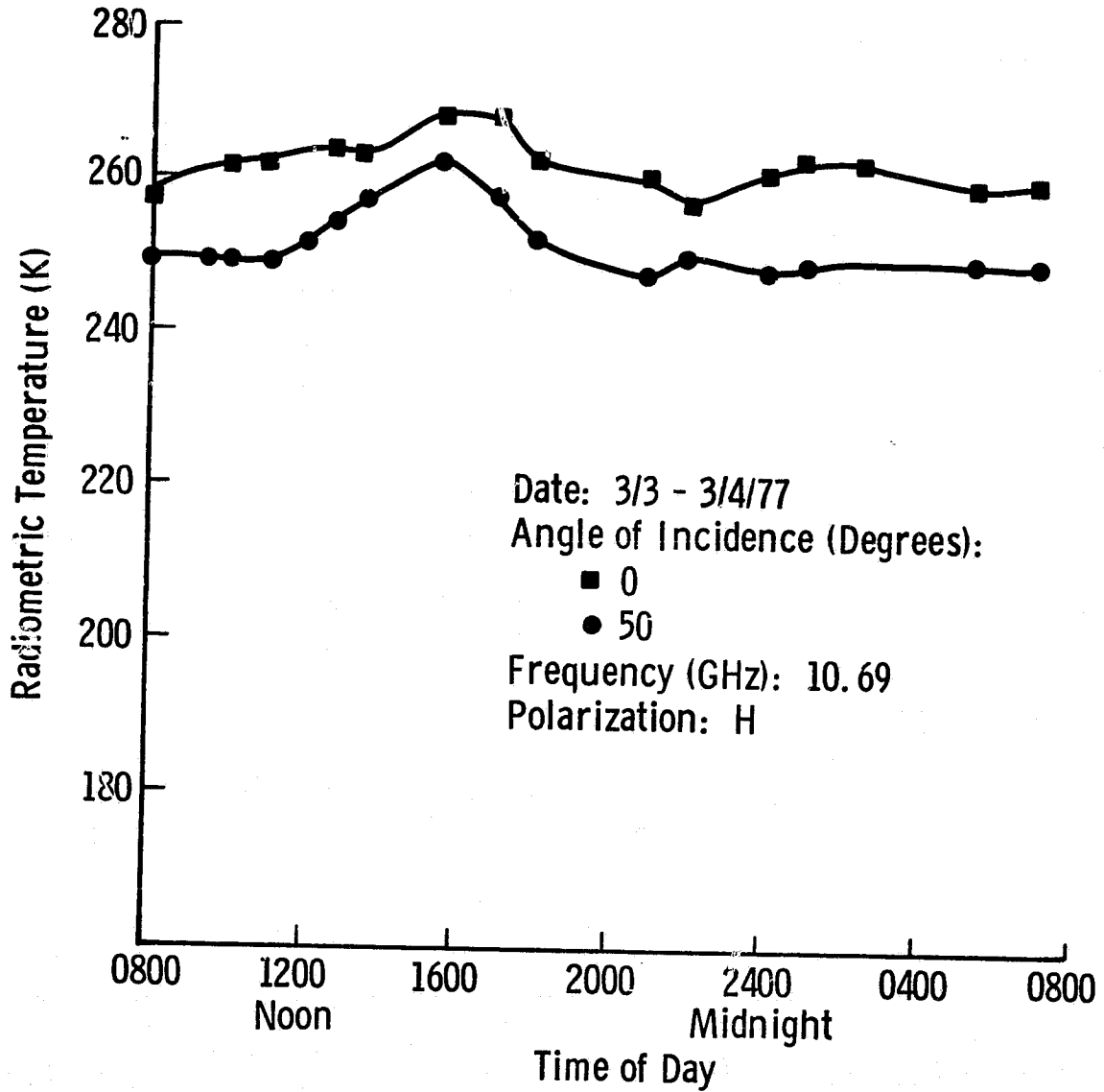
Date: 3/3 - 3/4/77
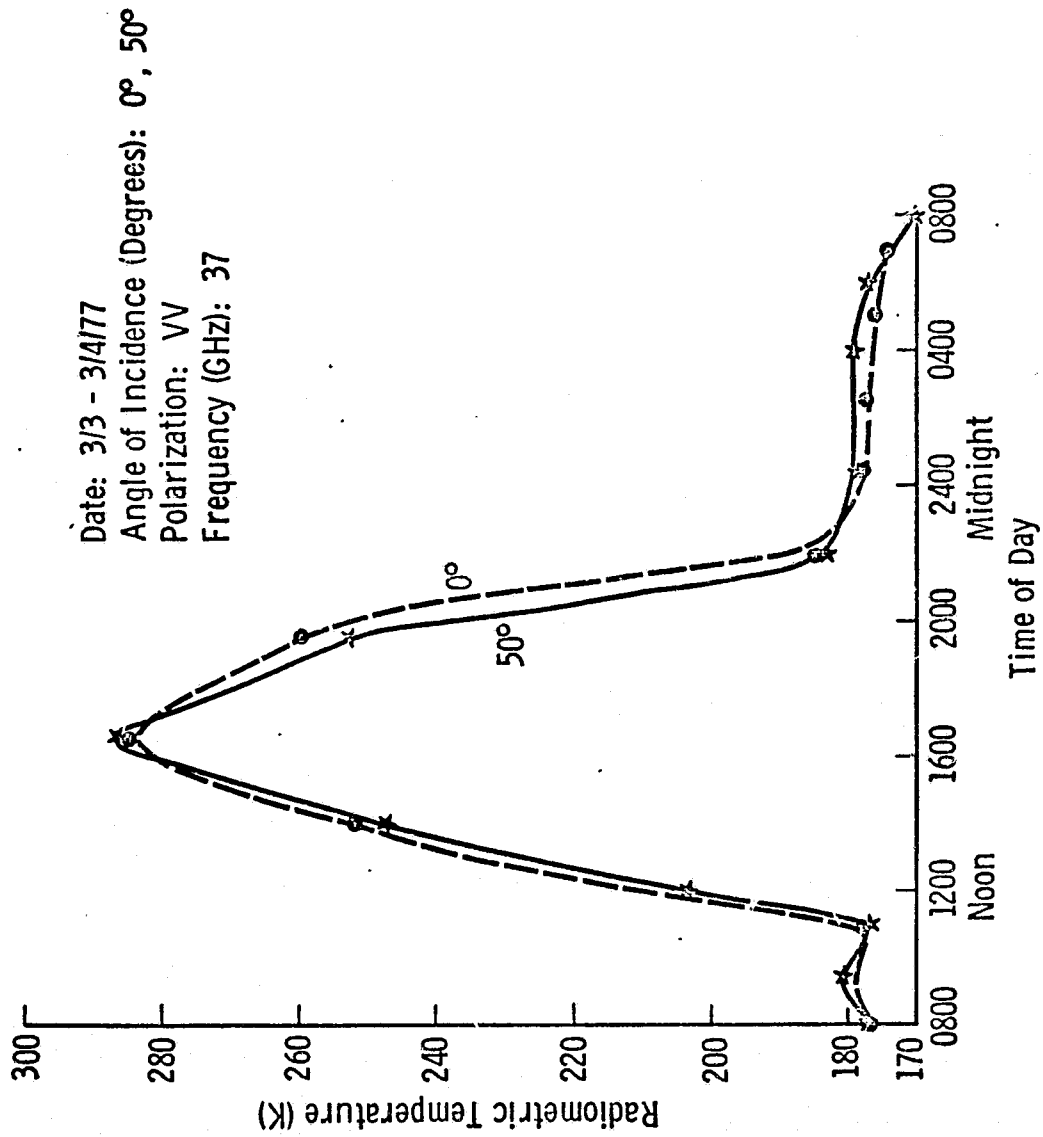Angle of Incidence (Degrees): 0°, 50°
Polarization: VV
Frequency (GHz): 37

Figure 65. Diurnal variation of 37 GHz radiometric temperature at 0° and 50°.

88

1. Passive Microwave

a) Wetness of the snow surface layer strongly affects the microwave emission at all angles of incidence (between 0° and 55°) and both frequencies employed in these two diurnal experiments (10.69 GHz and 37 GHz).

b) The response to wetness is much more pronounced at 37 GHz than at 10.69 GHz.

2. Active Microwave

a) Wetness of the snow surface layer strongly affects the microwave backscatter at angles of incidence away from nadir (20° or higher).

b) The response to wetness increases with frequency.

Further analysis of the data in conjunction with the results of the third and fourth diurnal experiments and the daily experiments should provide a more detailed picture of the passive and active microwave response to snow parameters.

4.3 Single Cell Diurnal Fluctuation Experiment

In this experiment all the data were acquired at 50° and 70° from nadir. The azimuth position remained unchanged for the entire 11 hour duration of the experiment. Sky conditions were clear in the morning and became partly cloudy to cloudy late in the day. Figure 66 shows the variations of the air temperature, snow surface layer temperature, snow temperature at 10 cm above the ground and the snow-ground interface temperature. Note that the temperature at 10 cm above the ground was cooler than either the snow surface temperature or the ground temperature. Figures 67 and 68 show the calorimeter and capacitance data for the surface layer. The dip in the capacitance readings at 1540 hours is due to the snow being so wet that the capacitor could not be filled properly. Figures 69 and 70 show the radar backscatter fluctuations over the measurement period. The trends at 50° and 70° are very similar. The 8.6 GHz data were stopped at 1500 hours due to equipment malfunction. When the snow was dry, in the early morning,
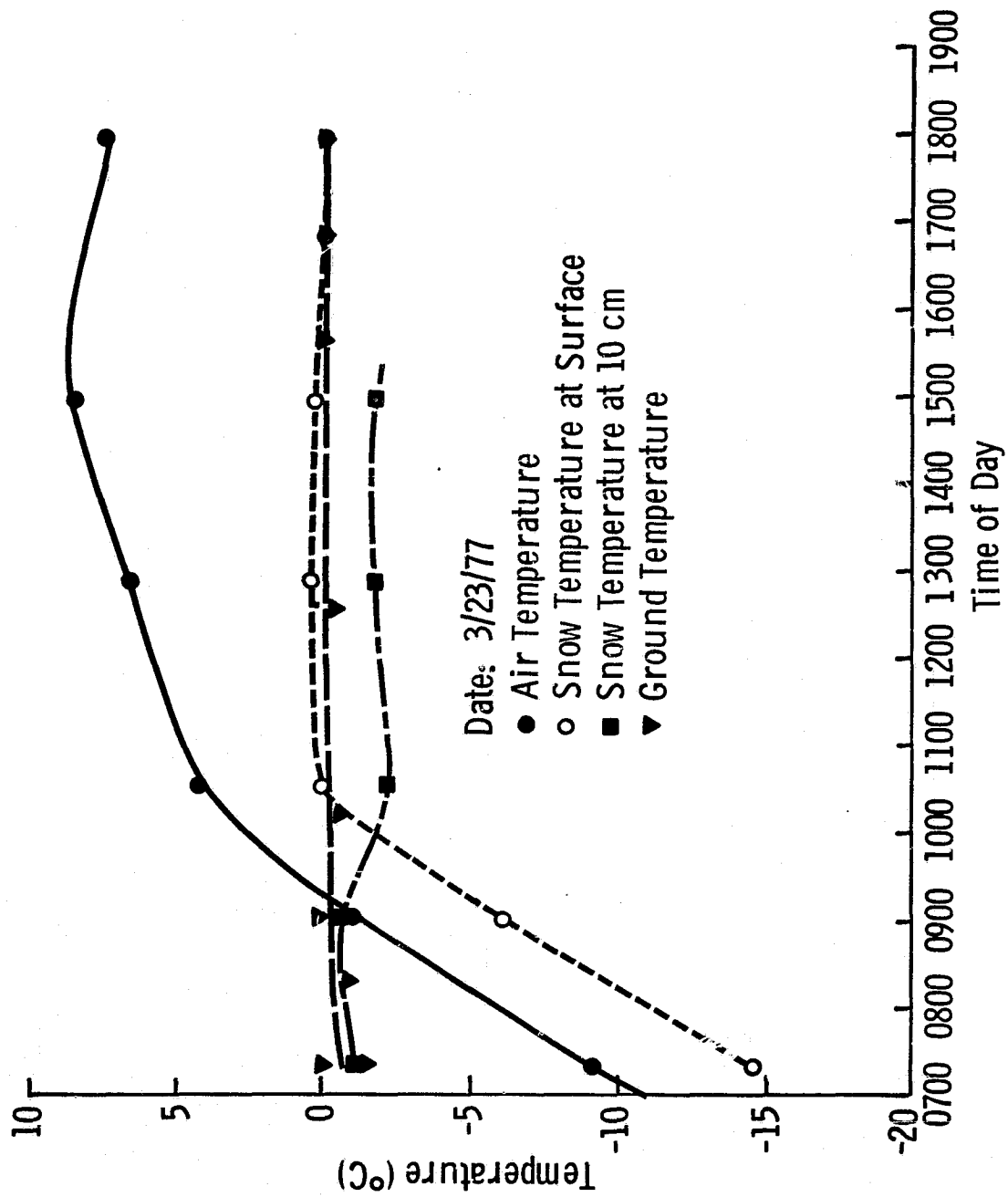
Figure 66. Temperature variation over the measurement period of the single cell experiment.

90
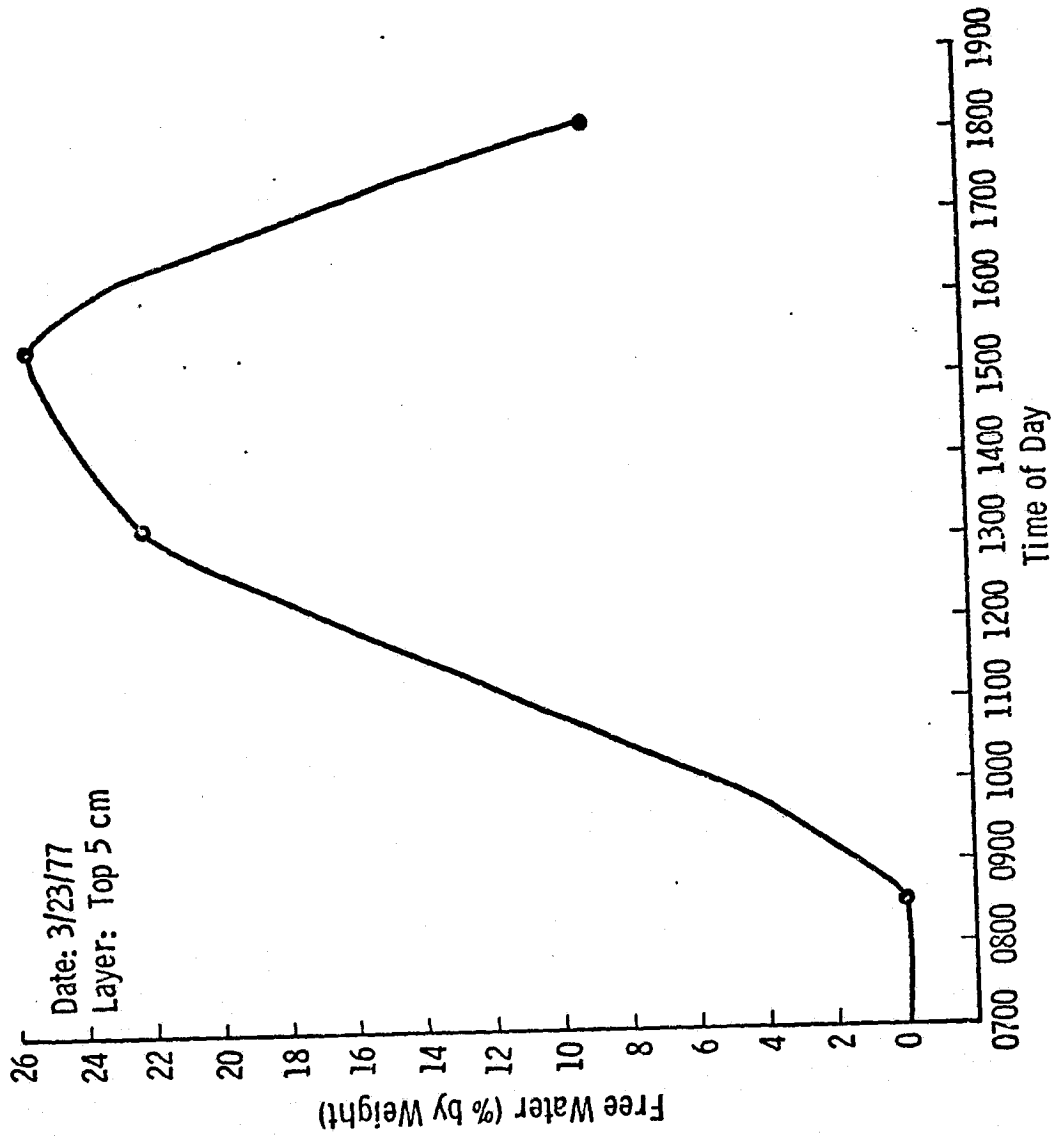
Figure 67. Snow free water content variation of the surface layer as measured by the freezing calorimeter.

91
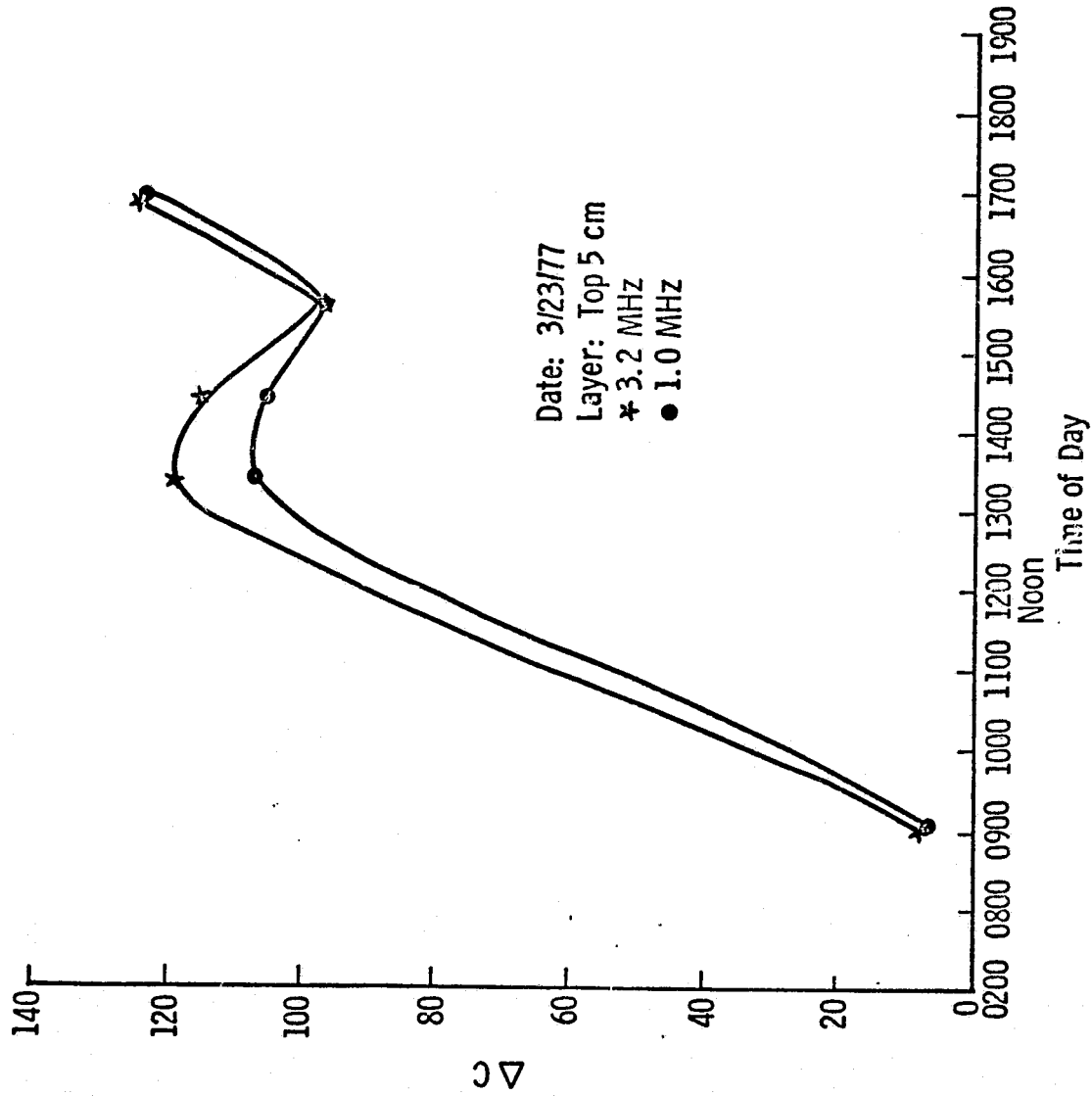
Figure 68. Variation in ΔC of the surface layer as measured by the Q-meter.
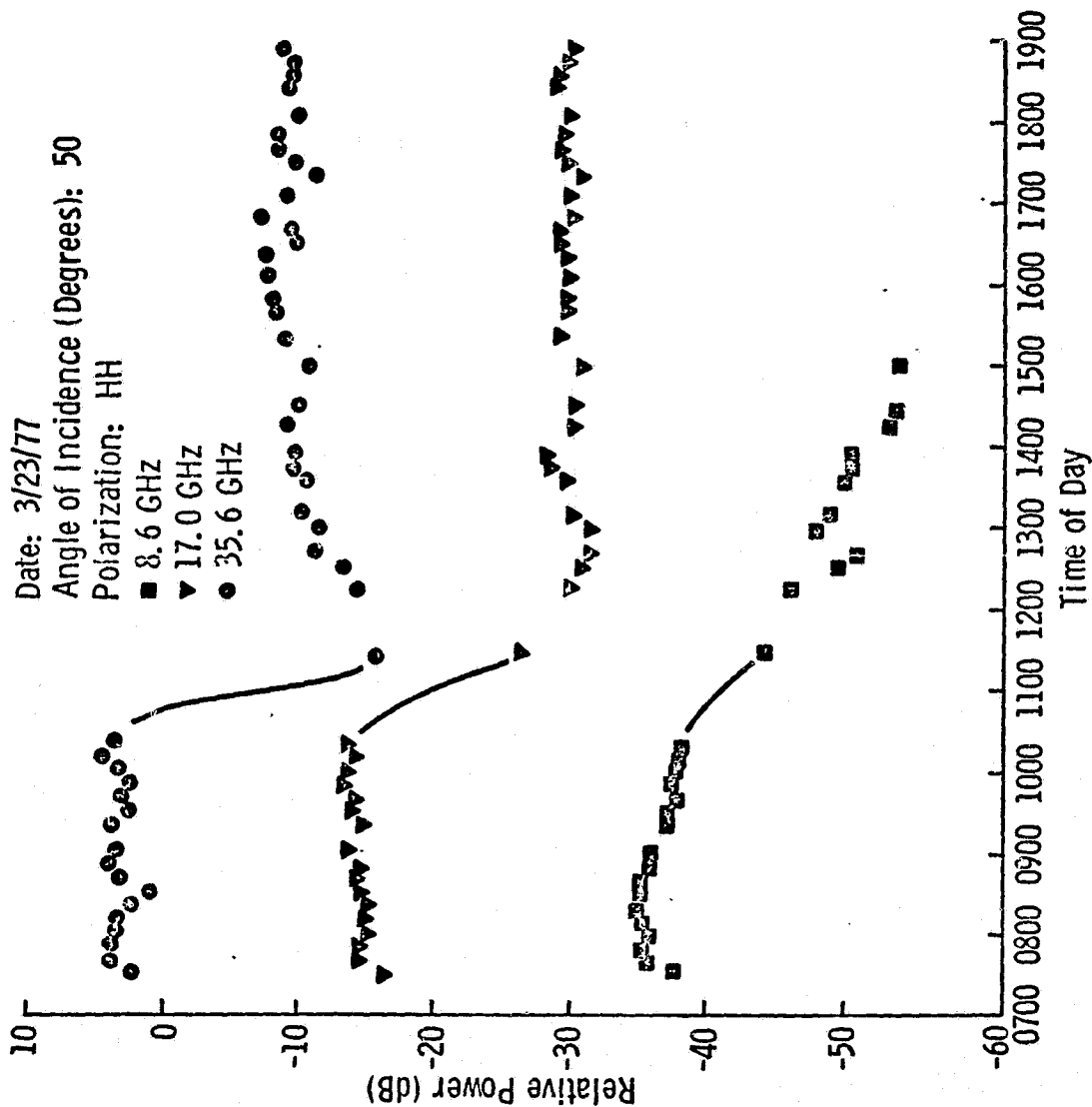
Figure 69. Time variation of 50° backscatter power at three frequencies.

93
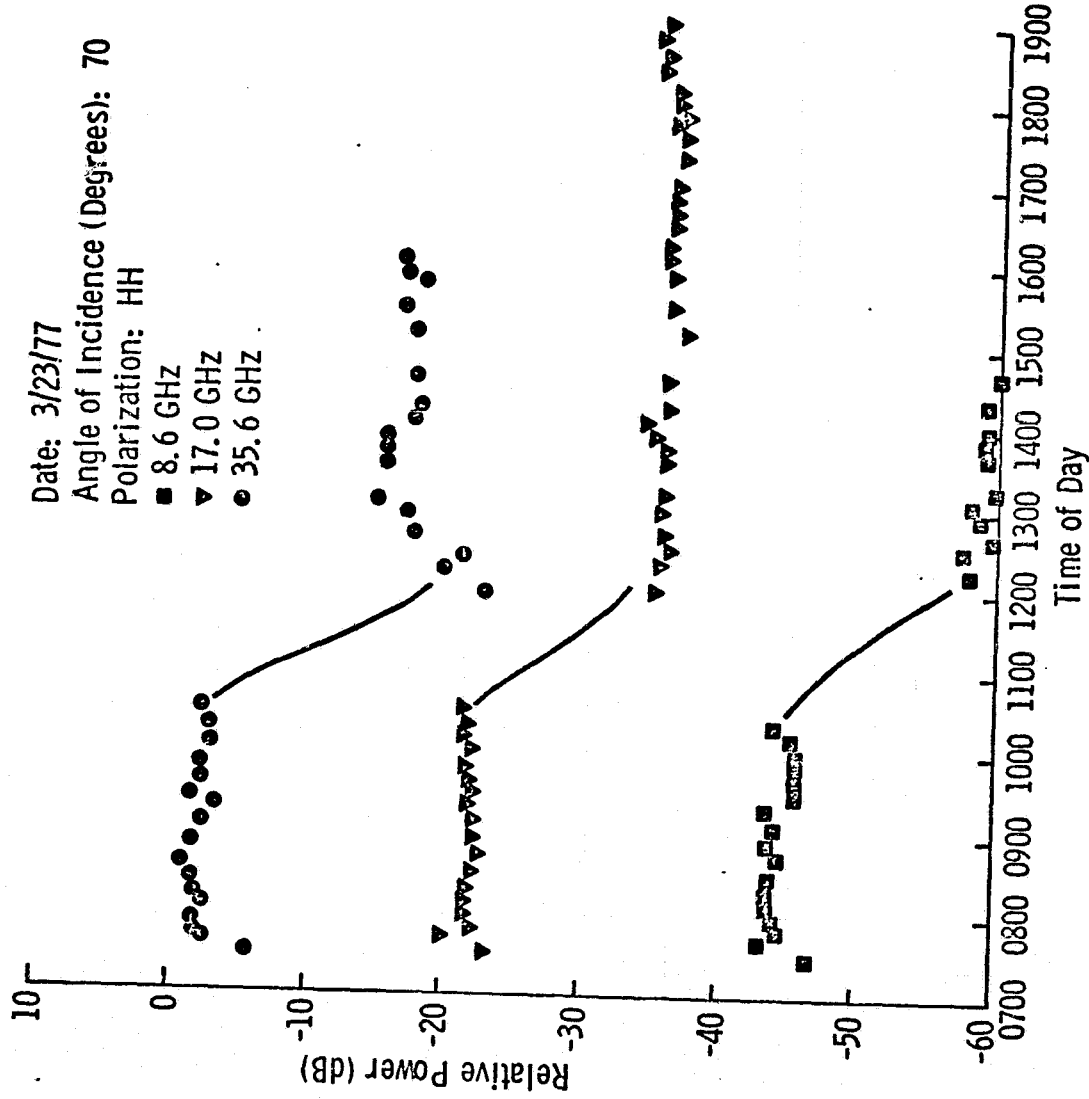
Figure 70. Time variation of $70°$ backscatter power at three frequencies.

94

the fluctuation in the measurements was on the order of 3 dB. Then
the surface layer underwent a rapid melting phase from about 1030 to
1200 hours. During this period, the cross section dropped by 12 dB,
16 dB and about 18 dB at 8.6 GHz, 17.0 GHz and 35.6 GHz, respectively.
The 8.6 GHz data appeared to be continually decreasing until the
equipment malfunctioned, this trend contrasts with the higher frequencies
which seemed to exhibit a saturation effect after about 1300 hours.
Figures 71 and 72 present the temperatures measured with the radiometers
at 50° and 70°. The 94 GHz radiometer overheated and had to be shut off
at 1500 hours. All three radiometers appear to saturate after about
1200 hours. The dynamic range from the wetest to dryest case was 40 K
for the 10.69 GHz radiometer increasing to about 120 K for the 37 GHz
channels and about 80 K for the 94 GHz radiometer. The 94 GHz data show
a decrease after 1200 hours at 70°, this may have been the result of gain
changes since a similar change is observed for the sky temperature at
94 GHz but not at 10.69 GHz or 37 GHz. Between 0745 hours and 1500 hours
the 94 GHz sky temperature decreased from 45 K to -25 K! This obvious drift
in the radiometer gain will be investigated as a means of correcting the
snow response.

4.4 Snowpile Experiments

Two snowpile experiments were conducted. In the first experiment,
the snow was piled to a depth of 144 cm in five steps. The air temperature
was below -2°C for the duration of the experiment. The snow temperature
varied from a maximum of -1.6°C at 134 cm above ground to -2.4°C at
74 cm. Calorimetric measurements were not obtained; however, these
temperatures indicate dry snow conditions. Figure 73 shows the variation
of radiometric temperature with depth. Bare ground was observed, then
fresh snow was added in increments of about 40 cm. Table 9 is a
summary of the ground truth data. In Figure 74 the radiometric data are
plotted versus water equivalent. The temperature decrease is seen to be
approximately linear above 3 cm of water for both 37 GHz channels and
at 10.69 GHz.
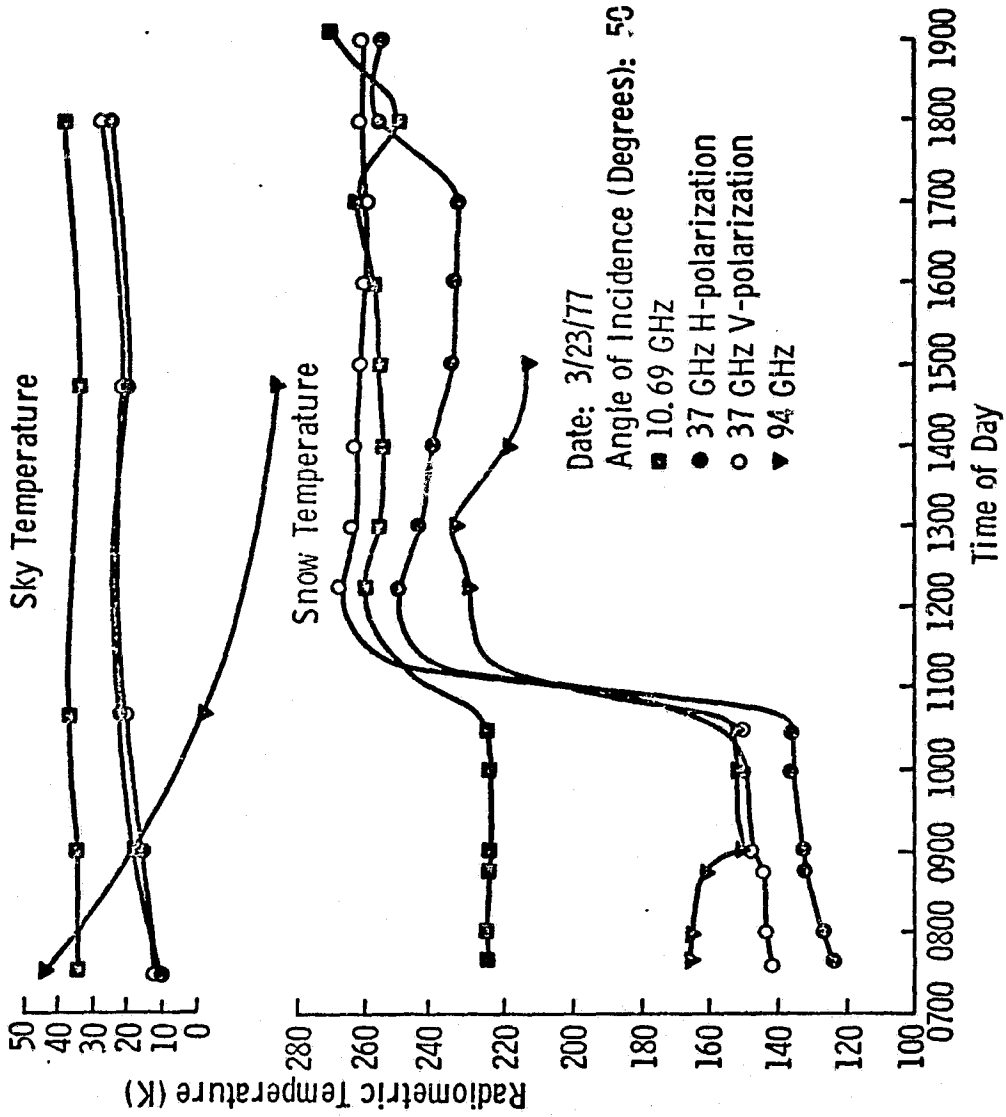
Figure 71. Time variation of the 50° radiometric temperature at three frequencies.

96
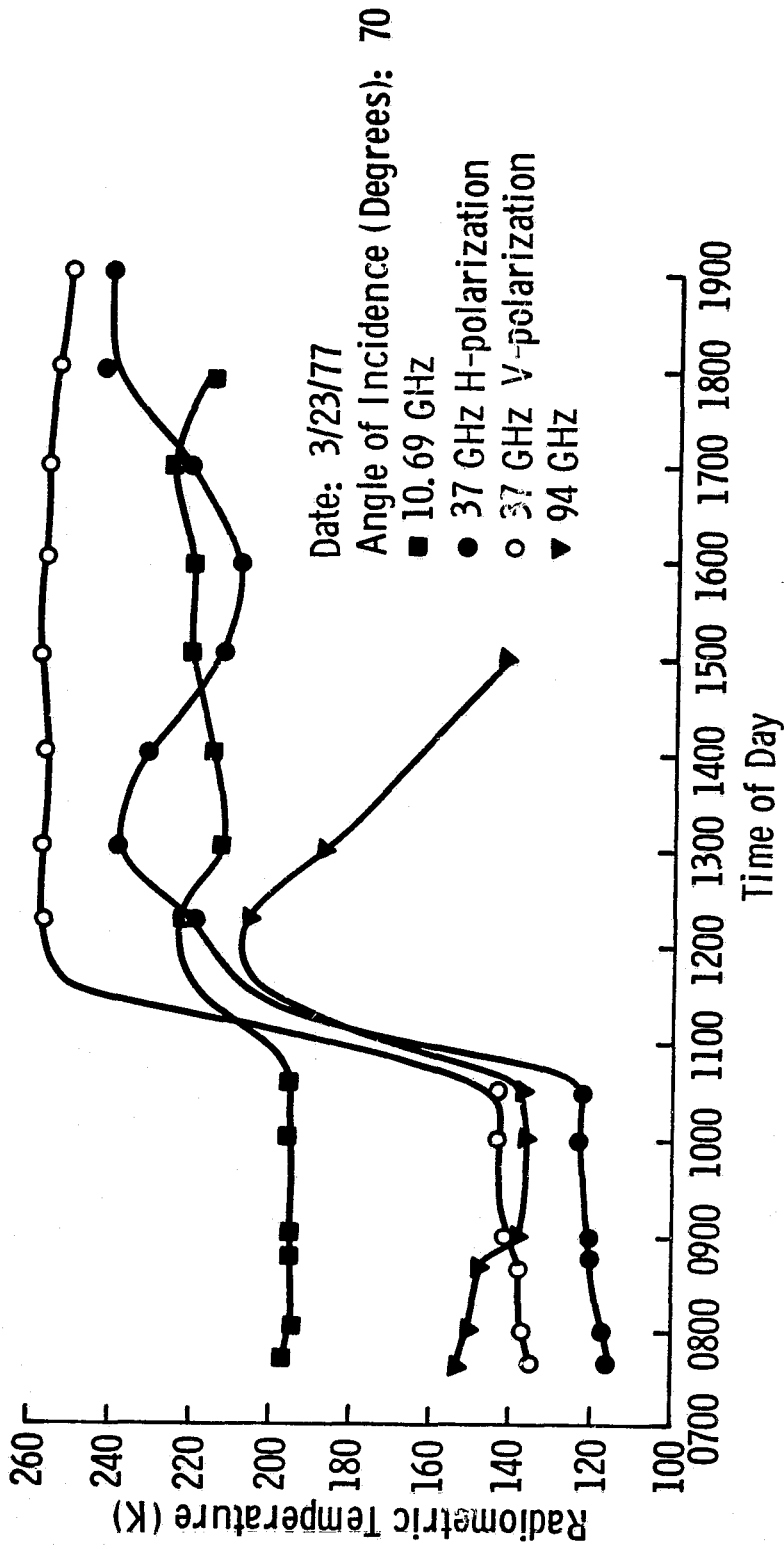
Figure 72. Time variation of the 70° radiometric temperature at three frequencies.

Figure 73. Radiometric temperature variation with snow depth.

TABLE 9.   Ground Truth for Snowpile Experiments

Date	Snow Layer (cm)	Density	Temperature
Feb. 24	144-113	.196	-1.8°C
	113-80	.176	-2.2°C
	80-40	.22	-2.4°C
	40-12	.226	-3°C
	12-0	.10	-4°C
March 21	170-120	.456	-1.7°C
	120-71	.425	- .8°C
	71-51	.413	-1.2°C
	51-32	.510	- .7°C
	32-13	.512	-1.0°C
	13-0	.340	- .5°C
March 22	170-140	.447	< 0°C
	140-120	.385	< 0°C
	120-105	.381	< 0°C
	105-85	.382	< 0°C
	85-70	.411	< 0°C
	70-52	.420	< 0°C
	52-37	.420	< 0°C
	37-14	.462	< 0°C
	14-0	.462	< 0°C

Date: 2/24/77
Angle of Incidence (Degrees): 27
■ 10.69 GHz
✻ 37 GHz, H-polarization
● 37 GHz, V-polarization

Figure 74. Radiometric temperature variation with water equivalent.

The second experiment included the 94 GHz radiometer. In this experiment snow was piled to a depth of 170 cm in seven layers. Figures 75 and 76 show the radiometric te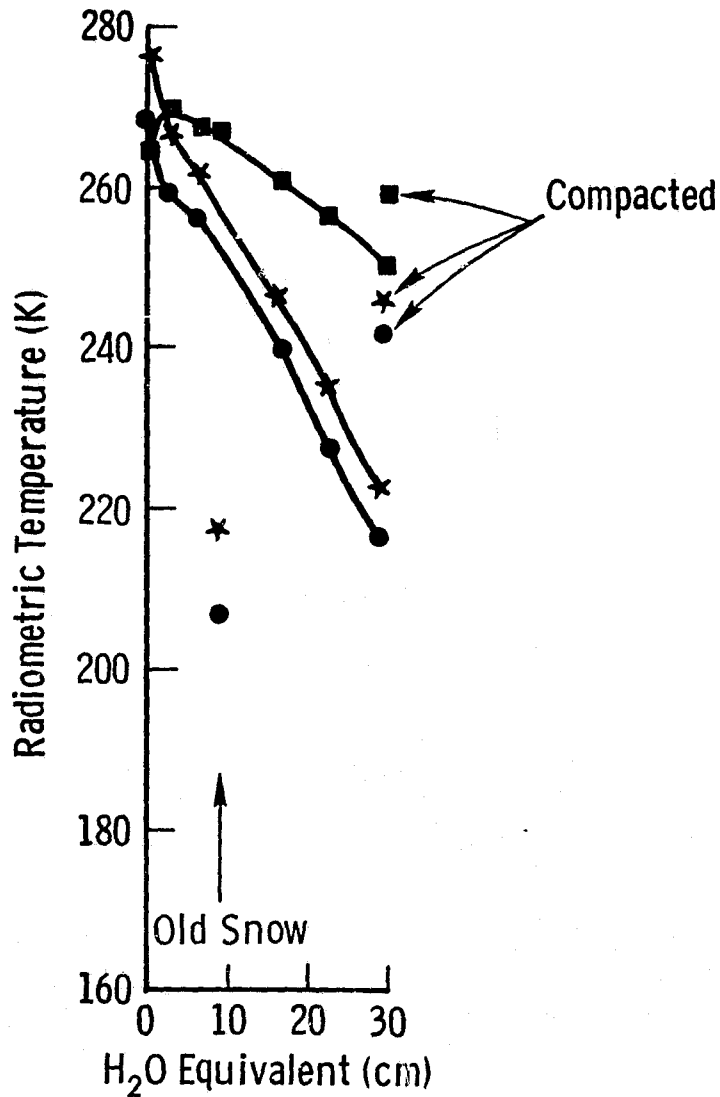mperatures plotted against depth and water equivalent. Calorimeter measurements were obtained for each layer and indicated that no free water was present. Note that there appears to be a saturation effect at about 30 cm water equivalent at 37 GHz. The 94 GHz response saturates at about 15 cm water equivalent.

The following day, the snowpile was uncovered by layers and the experiment repeated. Figures 77 and 78 show the results. The fluctuation in the 94 GHz response for depths greater than 70 cm was the result of temperature fluctuations of its ambient temperature (and hence its gain). The saturation effect is also apparent for this experiment. The 94 GHz radiometer response levels off after about 20 cm water equivalent and the 37 GHz response saturates at 23 cm water equivalent while the 10.69 GHz response continues to drop up to the maximum value of water equivalent although the rate of change decreases above 40 cm water equivalent. This observation indicates that the effective depth of penetration of the snow varies inversely with frequency which points to the potential use of multi-frequency microwave sensors to reconstruct the profile of snow parameters of interest.

4.5 35 GHz Attenuation Experiment

This experiment was performed on March 23 and March 25. Section 2.4.3 describes the method used. The total path loss through several thicknesses of snow was measured for three different layers of the snowpack. Table 10 gives the results of this experiment. Case 1 was the third layer from the top of the pack. No calorimeter measurements were obtained, but the snow was fairly wet. Case 2 was the second layer from the bottom. The wetness as measured by the calorimeter was 1.6%. Case 3 was the third layer from the top late in the day on March 25. Calorimeter measurements were not made, but the snowpack was near saturation in wetness. For this case only one reading was possible at 6 cm thickness before the layer collapsed. Figure 79 is a plot of the measured loss as a function of snow layer thickness for each of the three cases.

Date: 3/21/77
Angle of Incidence (Degrees): 57
■ 37 GHz, H-polarization
● 37 GHz, V-polarization
▲ 94 GHz
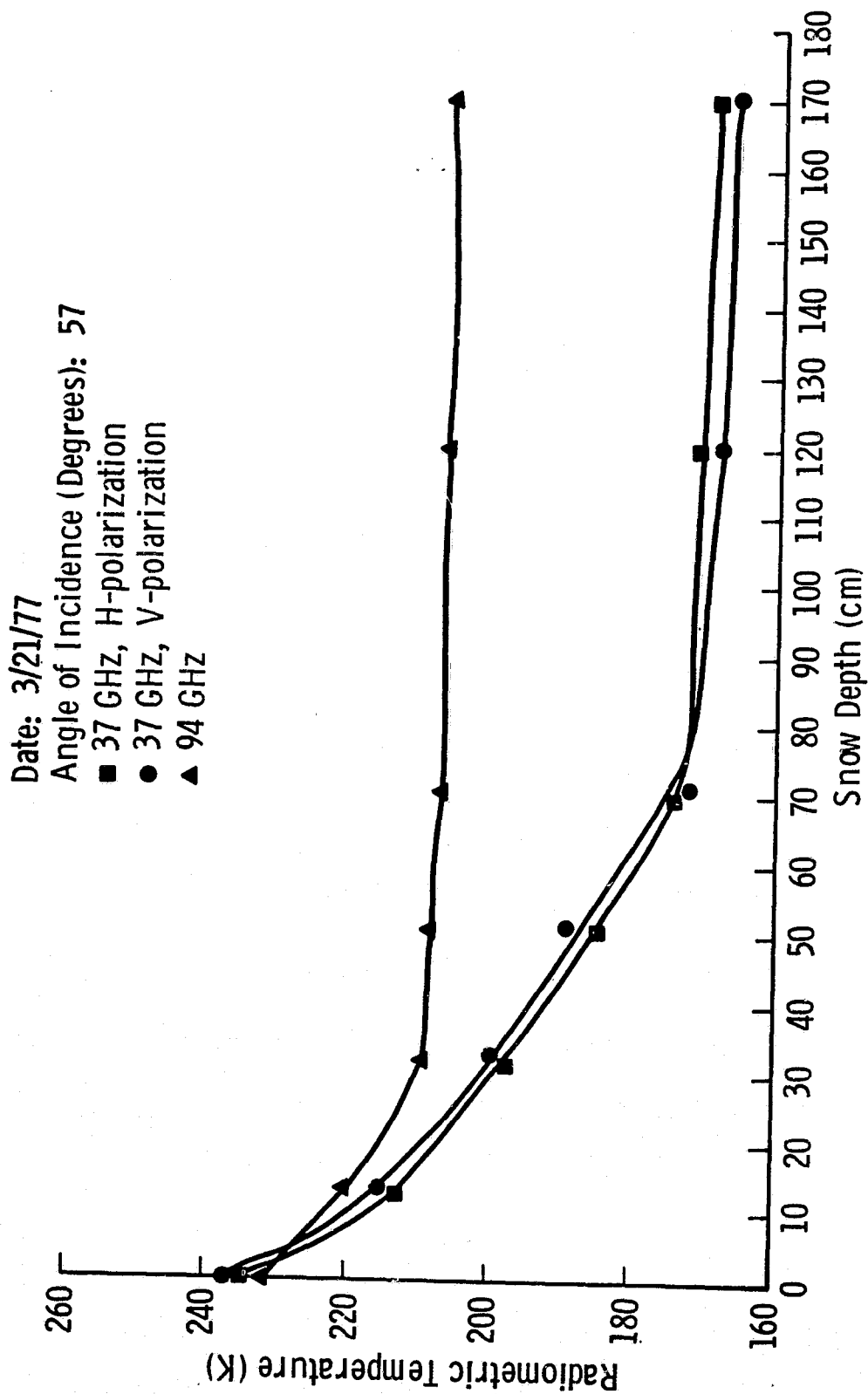
Figure 75. Radiometric temperature variation with snow depth.

Date: 3/21/77
Angle of Incidence (Degrees): 57
★ 37 GHz, H-polarization
■ 37 GHz, V-polarization
• 94 GHz

Figure 76. Radiometric temperature variation with water equivalent.
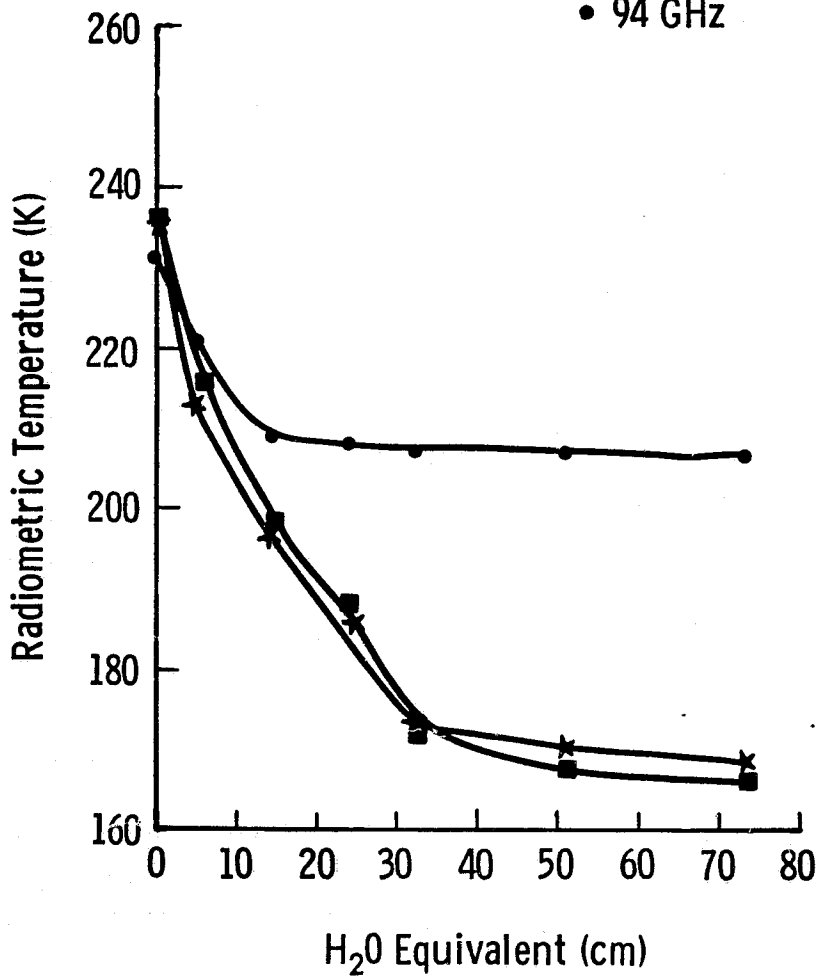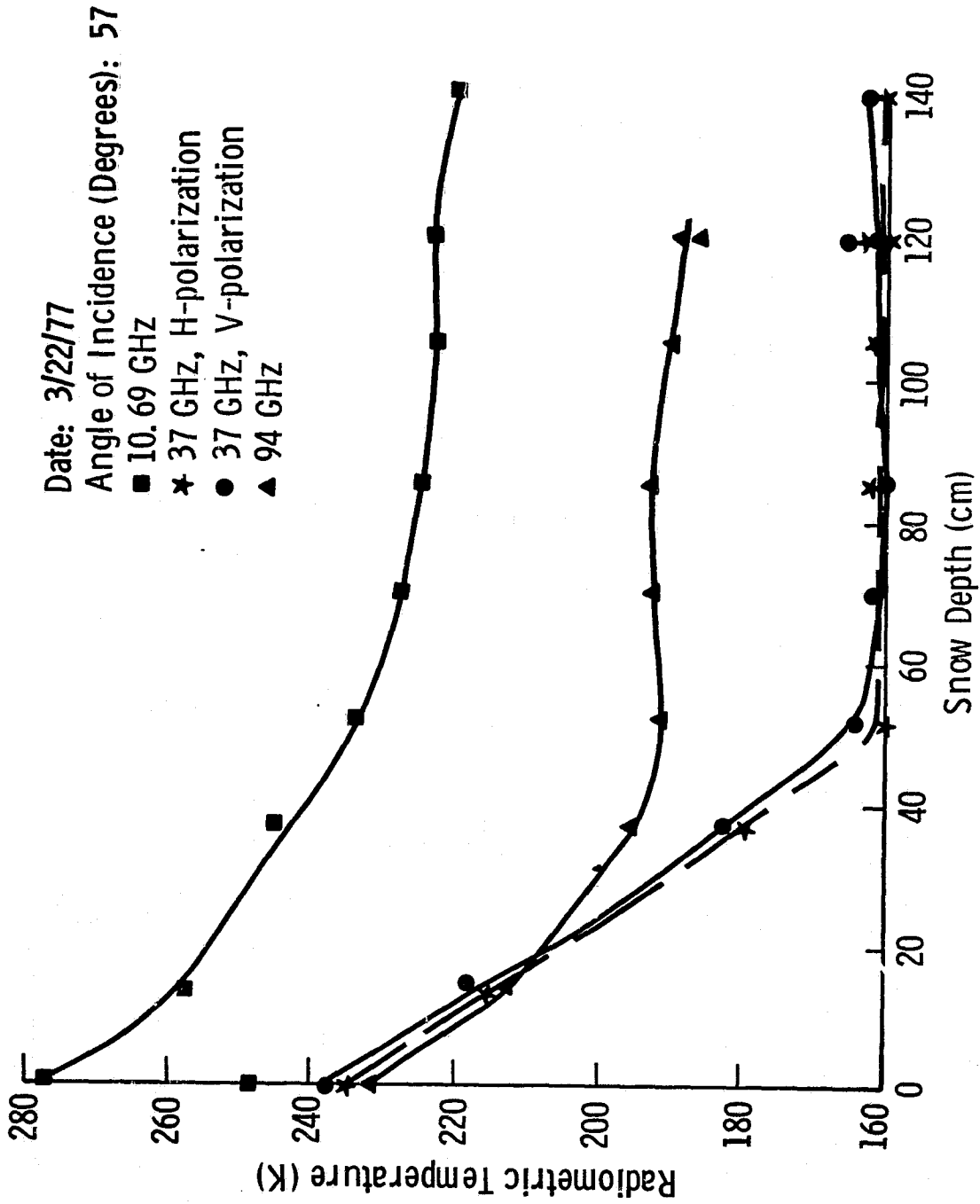
Figure 77. Radiometric temperature variation with snow depth.

Date: 3/22/77
Angle of Incidence (Degrees): 57
▼ 10.69 GHz
★ 37 GHz, H-polarization
■ 37 GHz, V-polarization
● 94 GHz
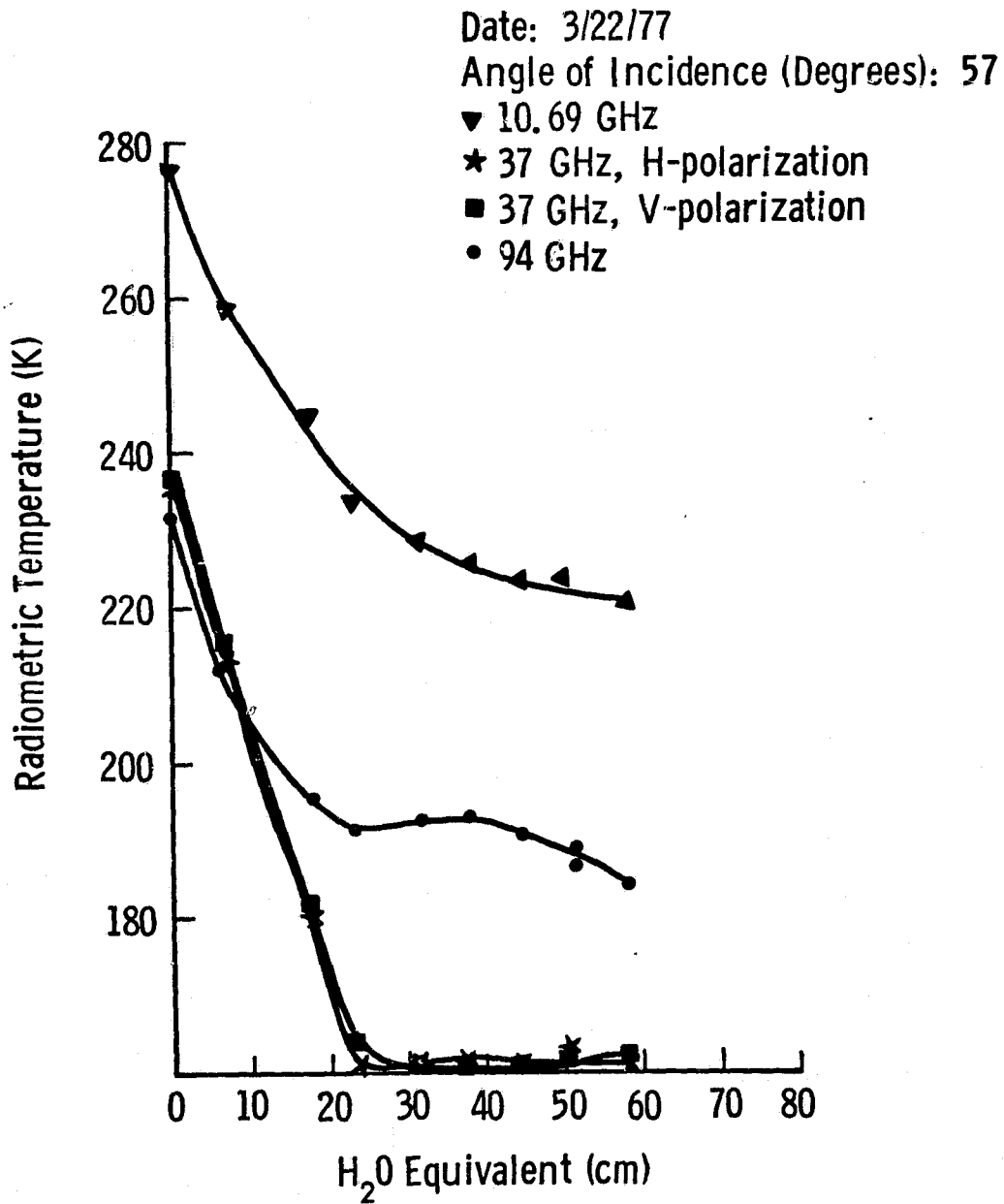
Figure 78. Radiometric temperature variation with water equivalent.

TABLE 10.   35 GHz Attenuation Experiment Data

Case	Snow Thickness (cm)	Received Power- Air Path	Received Power- Snow Path	Range (cm)
1 (wet snow)	20	-31.5 dBm	-62 (noise) dBm	30
	14	-30.5	-50.6	30
	10	-31	-41.5	30
	7	-31.2	-42	30
	5	-31.5	-43	30
2 (dry snow 1.6% free water)	57	-42.5	-54	67
	47	-38.5	-50.5	57
	39	-40	-52.5	57
	28	-39	-49	57
	17	-40	-46.5	57
	15	-40	-46	57
	7	-40	-41	57
3 (very wet snow)	8	-34	noise	40
	6	-33.6	-53.8	40

Figure 79. Measured path loss as a function of snow thickness for three snow conditions.

107

The difference between the power received through the air path and the power received through the snow path is the loss in dB. This loss is composed of two parts, misma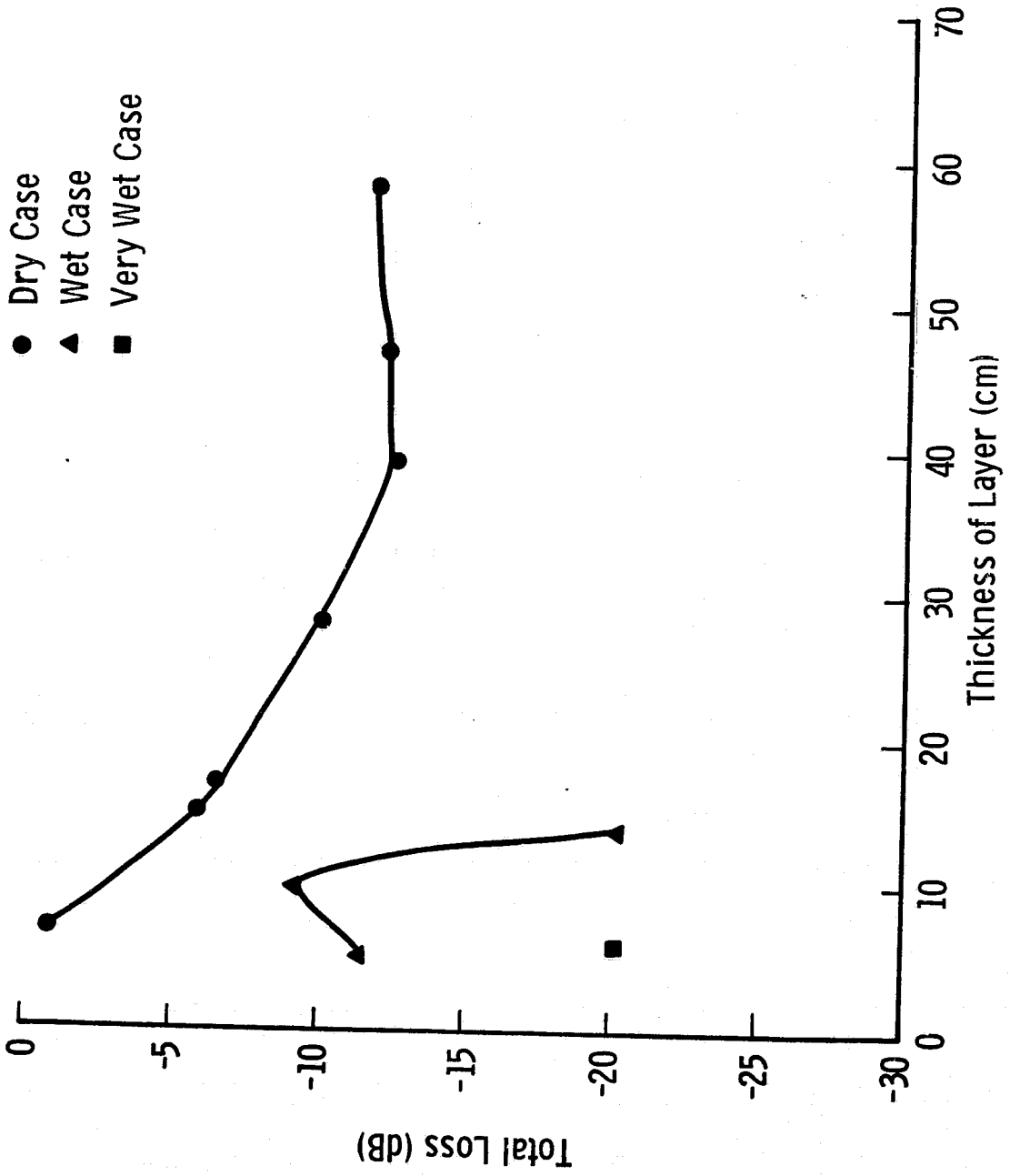tch loss and attenuation loss. Moreover, since the measurement is performed with coherent transmission, the two types of losses cannot be easily decoupled (even with multiple thickness measurements) because of the interference effects caused by multiple reflections, unless the measurements cover a wide range of thickness at intervals smaller than the effective wavelength in the snow. These conditions were not realized respectively because of the sensitivity limitation of the power meter and the difficulty involved in physically reducing the snow thickness while maintaining a flat interface.

REFERENCES

[1] Leaf, C. F., "Aerial Photographs for Operational Streamflow Forecasting in The Colorado Rockies," 37th Western Snow Conf. Proc., Salt Lake City, Utah, 1969.

[2] Barnes, J. C. and C. V. Bowley, "Snow Cover Distribution as Mapped from Satellite Photography," Water Resources Research, v. 4, n. 2, pp. 257-272, 1968.

[3] Cosgriff, R. L., W. H. Peake and R. C. Taylor, "Terrain Scattering Properties for Sensor System Design (Terrain Handbook II)," Ohio State University Experiment Station, 1960.

[4] Stiles, W. H., F. T. Ulaby, B. C. Hanson and L. F. Dellwig, "Snow Backscatter in the 1-8 GHz Region," RSL Technical Report 177-61, University of Kansas Center for Research, Inc., Lawrence, Kansas, 1976.

[5] Edgerton, A. T., A. Stogryn and G. Poe, "Microwave Radiometric Investigations of Snowpacks," Final Report for USGS, Aerojet General Corp., El Monte, California, 1971.

[6] Kunzi, K. F., A. D. Fisher, D. H. Staelin and J. W. Waters, "Snow and Ice Surfaces Measured by the Nimbus-5 Microwave Spectrometer," Journal of Geophysical Research, v. 81, pp. 4965-4980, 1976.

[7] Aerojet General Corporation, "Operations and Maintenance Manual for X-band Microwave Radiometer," prepared for NASA Langley Research Center.

[8] Sperry Microwave Electronics, Clearwater, Fla., "Technical Manual-- 94 GHz Radiometer," prepared for Air Force Avionics Laboratory, Air Force Systems Command U.S.A.F., Wright Patterson AFB.

[9] Linlor, W. I., F. D. Clapp, M. F. Meier and J. L. Smith, "Snow Wetness Measurements for Melt Forecasting," NASA Special Publication SP391, in Operational Application of Satellite Snowcover Observations, A. Rango, Ed., Proc. Workshop, Waystation, South Lake Tahoe, Ca., August 18-20, 1975.

[10] Leaf, C. F., "Free Water Content of Snowpack in Subalpine Areas," Western Snow Conf. Proc., 1966.

[11] Marshall, J. S. and W. Hitchfeld, "Interpretation of the Fluctuating Echo from Randomly Distributed Scatterers, Part 1," Canadian Journal of Physics, v. 31, n. 6, pp. 962-994, September, 1953.

[12] Swerling, P., "Probability of Detection of Fluctuating Targets," IRE Transactions, v. IT-6, pp. 269-308, April, 1960.

[13] Rice, S. O., "Mathematical Analysis of Random Noise," Bell System
      Technical Journal, v. 22, pp. 282-332, 1944; v. 23, pp. 46-156,
      1946.

[14] de Loor, G. P., "Radar Ground Returns Part III: Further Measurements
      on the Radar Backscatter of Vegetation and Soils," Physics Laboratory
      TNO, Rept. No. PHL-974-05, The Hague, The Netherlands, March, 1974.

[15] Bush, T. F. and F. T. Ulaby, "Fading Characteristics of Panchromatic Radar
      Backscatter from Selected Agricultural Targets," IEEE Transactions
      on Geoscience Electronics, v. GE-13, n. 4, pp. 149-157, October, 1975.

[16] Moore, R. K., W. P. Waite and J. W. Rouse, Jr., "Panchromatic and
      Polypanchromatic Radar," Proc. IEEE, v. 57, pp. 590-593, 1969.

[17] Waite, W. P., "Broad-Spectrum Electromagnetic Backscatter," CRES
      Technical Report 133-17, University of Kansas Center for Research, Inc.,
      Lawrence, Kansas, 1970.